ISBN 978-82-326-0394-7 (printed version)
ISBN 978-82-326-0395-4 (electronic version)
ISSN 1503-8181

NTNU – Trondheim
Norwegian University of
Science and Technology

Doctoral Thesis

Astrid Marie Flattum Muggerud

Doctoral theses at NTNU, 2014:239

Astrid Marie Flattum Muggerud

Transmission electron microscopy studies of dispersoids and constituent phases in Al-Mn-Fe-Si alloys

NTNU
Norwegian University of
Science and Technology
Faculty of Natural
Sciences and Technology
Department of Physics

NTNU – Trondheim
Norwegian University of
Science and Technology

Doctoral theses at NTNU, 2014:239

NTNU

Astrid Marie Flattum Muggerud

Transmission electron microscopy studies of dispersoids and constituent phases in Al-Mn-Fe-Si alloys

Thesis for the degree of Philosophiae Doctor

Trondheim, July 2014

Norwegian University of Science and Technology
Faculty of Natural Sciences and Technology
Department of Physics

NTNU – Trondheim
Norwegian University of
Science and Technology

NTNU
Norwegian University of Science and Technology

Thesis for the degree of Philosophiae Doctor

Faculty of Natural Sciences and Technology
Department of Physics

ISBN 978-82-326-0394-7 (printed version)
ISBN 978-82-326-0395-4 (electronic version)
ISSN 1503-8181

Doctoral theses at NTNU, 2014:239

Printed by Skipnes Kommunikasjon as

Abstract

3xxx aluminium alloys are used among others in packaging, architectural applications and heat exchangers. Both dispersoids and constituent phases are very important in this alloy system. The size and distribution of the dispersoids have a strong influence on the deformation, the recovery and recrystallisation behaviour and final mechanical properties of the 3xxx Al alloys. Also the constituent phases influence recrystallisation, grain size, texture and mechanical properties. In this thesis dispersoids and constituent phases in 3xxx Al alloys were studied, using transmission electron microscope (TEM) techniques as the main tools for the investigations. The alloys studied here were direct chill-cast 3xxx aluminium alloys with varying material composition. They were studied after various low temperature homogenisations.

Constituent phases extracted from the Al matrix were studied with respect to type, lattice parameters, chemical composition and morphology in alloys with various composition. Al_6(Fe,Mn) was found to be the most prominent constituent phase in the alloy with a low Si content. Orientation relationships (ORs) of constituent particles with relation to Al matrix were investigated for Al_6(Fe,Mn) and α-Al(Fe,Mn)Si constituents. The OR between the Al matrix and the Al_6(Fe,Mn) constituent was determined to be $[\bar{1}\bar{1}\bar{2}]_C$ // $[\bar{1}1\bar{1}]_{Al}$, $(33\bar{3})_C$ // $(0\bar{2}\bar{2})_{Al}$. This OR is consistent with the OR of Al_6(Fe,Mn) dispersoids. α-Al(Fe,Mn)Si constituent particles in the Si rich alloy were found to have various possible orientations.

The main focus of this thesis is the study of α-Al(Fe,Mn)Si dispersoids. How the precipitation of α-Al(Fe,Mn)Si dispersoids influences the hardness and tensile strength in alloys were systematically investigated. The evolution of density, size and volume fraction of the α-Al(Fe,Mn)Si dispersoids when varying the annealing time, the temperature and the alloy composition was quantitatively studied by conventional TEM and electrical conductivity

measurements. A hardening effect from the dispersoids was revealed. The hardening effect increases with increasing Mn and Si contents in the alloys. A high number density of relatively small dispersoids are beneficial for the hardness. For some applications of the 3xxx alloys this hardening during low temperature annealing is of significant importance for the further process.

The α-Al(Fe,Mn)Si dispersoid phase is a cubic icosahedral quasi crystal approximation phase. Investigations of quasi crystal approximant phases are important for better understanding of quasi crystals. Diffraction studies verified that the most commonly observed OR for the α-Al(Fe,Mn)Si dispersoids is $[1\bar{1}1]_\alpha$ // $[1\bar{1}1]_{\mathrm{Al}}, (5\bar{2}\bar{7})_\alpha$ // $(011)_{\mathrm{Al}}$. This orientation may be explained by the assumption that the Mackay icosahedron internal in the α-phase has a fixed orientation in relation to Al, similar to that of the icosahedral quasi crystals existing in this alloy system.

High angle annular dark field scanning transmission electron microscopy (HAADF STEM) tomography and diffraction studies were combined to study the α-Al(Fe,Mn)Si dispersoids in the 3xxx Al alloys. Most dispersoids were found to have a plate shaped morphology after low temperature homogenisation at 450 °C for 24 hours. The largest proportion of the dispersoids follows the commonly observed OR with the Al matrix. A methodology was established, which connects information about the morphology, the OR and the habit plane of crystalline particles, not restricted only to the dispersoid phase studied in this thesis.

Preface

This thesis is submitted to the Norwegian University of Science and Technology (NTNU) as a partial fulfilment of the requirements for the degree of philosophiae doctor (PhD). The work has been carried out at the Department of Physics, NTNU from August 2010 to July 2014, including 25% teaching duties at the Department of Physics, NTNU. This PhD project was a part of the KMB MoReAl project (Modelling towards Value-added Recycling Friendly Aluminium Alloys) with NTNU, SINTEF, Hydro Aluminium and Sapa Technology as partners.

The thesis is a paper collection divided in two parts. Part I contains an introduction to the papers in Part II. In Part I, Chapter 1 presents the motivation and introduction to the work. In Chapter 2 aluminium with focus on wrought 3xxx Al alloys are presented. Details about the dispersoid and constituent phases studied in the thesis are given. Transmission electron microscopy is presented in Chapter 3. This chapter presents a selection of the theory for electron interaction with matter forming the basis for the work with the transmission electron microscope. It is not intended as a full theoretical description of the topic, but as an overview of the theory relevant for the studies in this thesis. Further in this chapter, the transmission electron microscope is presented together with the relevant TEM techniques for this work. How to index and define orientation relationships are also outlined. Chapter 4 presents other experimental techniques relevant for the papers in the thesis. Chapter 5 concludes, summarises the work and presents an outlook for further work within the topic. Part II contains four scientific papers representing the scientific contribution of the work.

Papers included in the thesis

Paper I

Astrid Marie F. Muggerud, Eva A. Mørtsell, Yanjun Li and Randi Holmestad
Dispersoid strengthening in AA3xxx alloys with varying Mn and Si content during annealing at low temperatures
Materials Science and Engineering A 567 (2013) 21 – 28.

Paper II

Astrid Marie F. Muggerud, Yanjun Li and Randi Holmestad
Composition and orientation relationships of constituent particles in 3xxx aluminum alloys
Philosophical Magazine, Vol. 94, No. 6 (2014) 556 – 568.

Paper III

Astrid Marie F. Muggerud, Yanjun Li, Randi Holmestad and Sigmund Andersen
Mackay icosahedron explaining orientation relationship of dispersoids in Al alloys
Accepted for publication in Acta Crystallographica Section B.

Paper IV

Astrid Marie F. Muggerud, John C. Walmsley, Randi Holmestad and Yanun Li *Combining HAADF STEM tomography and electron diffraction for studies of α-Al(Fe,Mn)Si dispersoids in 3xxx aluminium alloys*
Submitted to Philosophical Magazine.

Statement of author contributions

Paper I

The manuscript was written by me. The experimental work and data analysis was done by myself, except the hardness and conductivity measurements of two alloys measured by Eva Mørtsell. Jesper Friis made a Phyton script for precipitation free zone analysis which was applied in this paper. Randi Holmestad and Yanjun Li supervised the work, helped interpreting the results and commented on the manuscript.

Paper II

The manuscript was written by me. The experimental work was carried

out by myself, except butanol particle extraction and X-ray powder diffraction (XRD) carried out by Christian Simensen (SINTEF). Randi Holmestad and Yanjun Li supervised the work, helped interpreting the results and commented on the manuscript.

Paper III
The manuscript was written by me. The experimental work was carried out by myself, except the micrographs of Figure 5 which were taken by Yanjun Li. Sigmund Andersen contributed significantly to interpret the results and to revise the manuscript. Randi Holmestad and Yanjun Li supervised the work and commented on the manuscript.

Paper IV
The manuscript was written by me. The experimental work and data processing was carried out by myself. John C. Walmsley assisted with discussion while developing the methodology. John C. Walmsley and Yanjun Li helped interpreting the results and commented on the manuscript. Randi Holmestad supervised the work and commented on the manuscript

Other scientific contributions

Publications

- Yanjun Li, Astrid Marie F. Muggerud, Arne Olsen and Trond Furu
  Precipitation of partially coherent α-Al(Mn,Fe)Si dispersoids and their strengthening effect in AA 3003 alloy
  Acta Materiala 60 (2012) 1004 – 1014.
- Astrid Marie F. Muggerud, Yanjun Li and Randi Holmestad
  Orientation relationship of dispersoids precipitated in an AA3XXX alloy during annealing at low temperatures
  Proceedings, 13th International Conference on Aluminum Alloys (ICAA13) TMS (The Minerals, Metals & Materials Society) (2012) 1161 – 1166.
- Eva A. Mørtsell, Astrid Marie F. Muggerud, Yanjun Li and Randi Holmestad
  Dispersion hardening effect of dispersoids in 3xxx Al alloys with varying manganese and silicon contents
  Proceedings, 13th International Conference on Aluminum Alloys (ICAA13) TMS (The Minerals, Metals & Materials Society) (2012) 1527 – 1532.

- Astrid Marie F. Muggerud, Eva A. Mørtsell, Yanjun Li and Randi Holmestad
  Strengthening mechanisms in 3xxx Aluminium alloys during annealing at low temperatures.
  Proceedings, 7th International Conference on the Physical Properties and Application of Advanced MATerials (ICPMAT) (2012) 97 – 98.

- Astrid Marie F. Muggerud, Yanjun Li, and Randi Holmestad
  Orientation studies of α-Al(Fe,Mn)Si dispersoids in 3xxx Al alloys
  Materials Science Forum Vols. 794-796 (2014) 39 – 44.

Oral presentations

- Astrid Marie F. Muggerud, Yanjun Li, Eva A. Mørtsell, and Randi Holmestad
  Precipitation behaviour of dispersoids in 3xxx alloys during annealing at low temperatures
  ECAA, the Conference on Aluminium Science and Technology,
  05 – 07 October 2011, Bremen, Germany.

- Astrid Marie F. Muggerud, Yanjun Li and Randi Holmestad
  Orientation relationship of dispersoids precipitated in an AA3XXX alloy during annealing at low temperatures
  13th International Conference on Aluminum Alloys (ICAA13)
  03 – 07 June 2012, Pittsburgh, USA.

- Astrid Marie F. Muggerud, Yanjun Li, and Randi Holmestad
  Orientation studies of α-Al(Fe,Mn)Si dispersoids in 3xxx Al alloys
  14th International Conference on Aluminum Alloys (ICAA14)
  15 – 19 June 2014, Trondheim, Norway.

Posters

- Eva A. Mørtsell, Astrid Marie F. Muggerud, Yanjun Li and Randi Holmestad
  Dispersion hardening effect of dispersoids in 3xxx Al alloys with varying manganese and silicon Contents
  13th International Conference on Aluminum Alloys (ICAA13)
  03 – 07 June 2012, Pittsburgh, USA.

- Astrid Marie F. Muggerud, Eva A. Mørtsell, Yanjun Li and Randi Holmestad
  Dispersoid strengthening in AA3xxx Al-Fe-Mn-Si alloys with varying Mn and Si content
  7th International Conference on the Physical Properties and Application of Advanced MATerials (ICPMAT), 17 – 20 June 2012, Trondheim, Norway.
- Astrid Marie F. Muggerud, Yanjun Li and Randi Holmestad
  Study of dispersoids in 3xxx aluminum alloys after low temperature annealing
  International conference on processing and manufacturing of advanced materials (THERMEC), 02 – 06 December 2013, Las Vegas, USA.

Trondheim July 2014

Astrid Marie Flattum Muggerud

Acknowledgements

Professor Randi Holmestad at Department of Physics has been the main supervisor of my PhD. I thank her for her support and encouragement, always positive, compassionate and trying to find solutions. Thank you for including me in the TEM group. Professor Yanjun Li at Department of Materials Science and Engineering was the leader of the MoReAL project under which I was hired. He has been a large source to knowledge about the alloys I have studied. He is acknowledged for his time spent helping me, and for providing me the opportunity to work within the project. Further, the research council of Norway, Hydro Aluminium and Sapa Technology are acknowledged for the financial support of the project.

Dr. Sigmund J. Andersen at SINTEF Materials and Chemistry was a large source of knowledge for the crystallography of the dispersoid phase studied. His time and effort put into Paper III is greatly acknowledged. Dr. John C. Walmsley at SINTEF Materials and Chemistry has been essential when it comes to the tomography part of my thesis in Paper IV. Thank you for always showing interest in my work, being friendly, encouraging and providing good advices. Associate professor Ton Van Helvoort at NTNU, Dr. Jesper Friis and Dr. Per Erik Wullum at SINTEF Materials and Chemistry, thank you all for the willingness to help solving practical or theoretical obstacles in relation to my work. Bjørn Soleim, the TEM group engineer is greatly acknowledged for only being a phone call away when I was facing practical problems at the microscopes. Dr. Christian J. Simensen, SINTEF, is acknowledged for help with particle extraction and organisation of the XRD measurements in Paper II.

I spent 6 weeks in Beijing, China, visiting Professor Wenzheng Zhang at Department of Materials Science at Tshinghua University. Professor Zhang is greatly acknowledged for providing me the opportunity to visit her group.

I have been privileged with many nice past and present colleagues in the

TEM group and at the rest of the Department of Physics. As a bonus, friendships not restricted to the work environment have been developed, a side effect I am highly grateful for. Eva Mørtsell, master student in the MoReAl project the two first years and now a PhD colleague, thank you for a nice and well functioning collaboration, which also resulted in a friendship. Dr. Flemming Ehlers, thank you for your insight, compassion and all the interesting discussions of more or less philosophical character.

And to my friends and family, in Norwegian:

Tusen takk til venner og familie for støtte, oppmuntring og avkobling fra arbeidet med doktorgraden. Anne Jone, takk for at du alltid viser stor interesse i både arbeidet mitt og livet generelt. Takk for alle besøk i Trondheim, du er en sann venn. Lene, det har vært så fint at du også har vært i Trondheim alle disse årene. Takk for at du er en venn og støtte i tykt og tynt.

André, Elin og Øyvind, Paul Fredrik, Ottar og Mimmi, takk for at dere alltid har vist interesse i det jeg holder på med og oppmuntret meg.

Lars-Kristian, du er min lille sol og stolthet, ingen kan lyse opp tilværelsen som deg. Sigurd, jeg er allerede veldig glad i deg. Birgit, takk for at du er min søster og sjelevenn. Din støtte, veiledning og tiltro betyr uendelig mye for meg.

Mamma og Pappa, dere har alltid latt meg ta mine egne valg, støttet og oppmuntret meg uansett. Takk for den ubetingede kjærlighet, tiltro og støtte dere alltid har gitt meg.

Lars Martin, takk for all hjelp av mer eller mindre teknisk karakter de siste 10 årene. Og enda viktigere, takk for at du alltid er der for meg og har tro på meg.

Det er den draumen

Det er den draumen
Det er den draumen me ber på
at noko vidunderlig skal skje,
at det må skje -
at tidi skal opna seg,
at hjarta skal opna seg,
at dører skal opna seg,
at kjeldor skal springa -
at draumen skal opna seg,
at me ei morgonstund skal glida inn
på ein våg me ikkje har visst um.

∼Olav H. Hauge∼

Abbreviations

2D	Two dimensional
3D	Three dimensional
ART	Algebraic reconstruction technique
bcc	Body centred cubic
BF	Bright field
BSE	Backscattered electrons
CBED	Convergent beam electron diffraction
CT	Computerised tomography
DF	Dark field
DP	Diffraction pattern
EDX	Energy dispersive X-ray spectroscopy
EELS	Electron energy loss spectroscopy
fcc	Face centred cubic
HAADF	High angle annular dark field
HR	High resolution
HV	Vickers hardness

IQC	Icosahedral quasi crystalline
MI	Mackay icosahedron
MoReAl	Modelling towards Value-added Recycling Friendly Aluminium Alloys
NTNU	Norwegian University of Science and Technology
OR	Orientation relationship
PhD	Philosophiae doctor
SA	Selected area
SADP	Selected area diffraction pattern
sc	Simple cubic
SE	Secondary electrons
SEM	Scanning electron microscope
SIRT	Simultaneous iterative reconstruction technique
STEM	Scanning transmission electron microscopy
TDS	Thermal diffuse scattering
TEM	Transmission electron microscope
WBP	Weighted back projection
XRD	X-ray diffraction

Contents

Part I

Introduction

Chapter 1

Motivation and introduction

Aluminium production is Norway's third largest industry, after oil and fish. As the two larger industries, the Al production in Norway is closely related to water. The production of Al is an energy demanding process, the large capacity of hydro power makes aluminium production in Norway both sustainable and beneficial.

By the addition of alloying elements, Al is a metal with highly tuneable material properties. The possibility to tune the properties of aluminium makes it favourable for a wide range of applications. Beneficial characteristics of aluminium are the high strength, the good thermal and electrical conductivity and the high formability. Also, a beneficial fundamental property of aluminium is its low weight. From an environmental perspective this is an important advantage. By replacing steel with aluminium the fuel consumption in transportation vehicles such as aircrafts, cars and trains is substantially reduced.

Another advantageous property of aluminium in an environmental perspective is its recyclability. The energy demand to recycle Al is as low as 5% of the energy demand in primary Al production [1]. Packaging products, like for instance beverage cans, have a short life cycle from a produced can to an empty scrap can and is therefore desirable to recycle. The changes in the chemical composition introduced in the recycling process alter the microstructural development. Therefore effort must be made to understand these alterations and predict the changes in material characteristics induced by the recycling.

The work in this thesis has been a part of the MoReAl project, which is short

for *Modelling towards Value-added Recycling Friendly Aluminium Alloys*. The alloys studied in this project were wrought non-heat treatable direct chill-cast 3xxx aluminium alloys, used in products such as heat exchangers, packaging (i.e. beverage can bodies) and architectural applications. The principal objective of the project was to establish the next generation of physically based micro structure models. Such models aim to predict the behaviour and mechanical properties of aluminium alloys during complex thermo mechanical processing. In order to make such a model physically trustful, experimental input for each processing step is essential.

The first processing step after casting of the Al alloys is the homogenisation. Homogenisation is carried out to reduce solid solution levels of alloying elements and to obtain the optimum type, size and density of both the larger constituent particles and the smaller dispersoids before mechanical processing. Constituent phases and dispersoids are very important in these Al alloys as they influence the recrystallisation, the grain size, the texture and the mechanical properties [2–7]. In this thesis the constituent particles and the dispersoids are studied after homogenisation treatment.

During solidification of wrought non-heat treatable 3xxx Al alloys, the constituent Al_6(Fe,Mn) and α-Al(Fe,Mn)Si phases form [8]. The constituents were extracted and studied with regards to phase type, lattice parameters, morphology and composition in order to obtain an in-depth understanding of the nucleation mechanisms and growth behaviour. The constituents were also studied as embedded in the Al matrix with respect to the orientation relationship with the Al grain boundaries.

Two main phases of dispersoids, orthorhombic Al_6(Fe,Mn) and cubic α-Al(Fe,Mn)Si, precipitate during homogenisation in non heat treatable commercial 3xxx Al alloys [4, 9–11]. Composition and heat treatment govern which types of dispersoids that precipitate. The α-Al(Fe,Mn)Si dispersoids were the main focus of this thesis. They were studied with respect to size, number density, hardness and tensile strength for varying alloy compositions, and homogenisation temperatures and times.

The α-Al(Fe,Mn)Si phase is a so-called quasi crystalline approximant [12, 13]. The phase is rather complex, consisting of two almost identical layered Mackay icosahedra(MIs) [14]. The structure of the α-Al(Fe,Mn)Si phase was used to provide an explanatory model for the commonly observed orientation relationship (OR) to the matrix for the dispersoids in these alloys. Investigations of such approximant phases are important in order to obtain a better understanding of quasi crystals. The quasi crystals are the initially

formed phase nucleating the dispersoids, and are directly coupled to the mechanical properties of the alloys.

The transmission electron microscope (TEM) is a very powerful tool for investigating material characteristics and have been the main tool for the investigations in this thesis. Conventional TEM techniques only provide two dimensional (2D) projections of a three dimensional (3D) structure. High angle annular dark field (HAADF) scanning transmission electron microscopy (STEM) tomography were used to reveal the 3D morphology of the α-Al(Fe,Mn)Si dispersoids. A methodology to connect information about morphology, OR and habit plane of the dispersoid phases were developed by combining electron diffraction studies and HAADF STEM tomography.

Part I of this thesis contains an introduction to Al and the phases studied in the papers in Part II of this thesis. Further, an introduction to transmission electron microscopy, with the relevant theory and techniques for the work in this thesis, is presented. Also, other experimental techniques used in this thesis are described. Summary and outlook of further work concludes Part I.

Chapter 2

Aluminium alloys, dispersoids and constituent phases

Aluminium is one of the most abundant metal in the earth's crust [15]. Al has atomic number 13 and belongs to the boron group in the periodic table. The crystal structure of Al is face centred cubic (fcc), with lattice parameter $a = 4.049$ Å, and mass density 2.698 g/cm^3, approximately 1/3 of the density of steel [16]. In addition to the low mass density, Al has high strength, good thermal and electrical conductivity, high formability and recyclability [1].

Bauxite is the main source of Al. It is refined to alumina (Al_2O_3), before electrolysis to Al in the Hall-Héroult process, which is the basis of all aluminium production [15]. Independently of each other, the American and French scientists Charles Hall and Paul Héroult developed the principle of how to produce aluminium in 1886. In this process, alumina (Al_2O_3) is reduced in molten cryolite (Na_3AlF_6). An electric current is applied to ionize the dissolved alumina. Oxygen from the alumina reacts with a carbon anode and produces CO_2, while liquid aluminium metal is deposited at the cathode. The production process needs a lot of electrical power. Due to Norway's large hydro power resources production of aluminium is reasonable here, where it started in Høyanger as far back as in 1916.

2.1 Aluminium alloys

There are two main categories of aluminium: cast alloys and wrought alloys. Cast alloys are directly casted into the shape of the product, while wrought aluminium alloys are deformed after initial casting [15]. Wrought alloys are manufactured into standardised products, such as sheets, plates, foils, rods and bars, or engineered products for special applications, e.g. extruded shapes or forgings. The cast and wrought alloys are further categorized into non-heat-treatable and heat-treatable alloys. The wrought alloys are placed in an alloy identification system based on their main alloying elements. Table 2.1 presents the main alloying elements, heat-treatability and main application fields for the wrought Al alloys.

Table 2.1: Wrought Al alloy classification after main alloying elements, fields of applications and heat treatability [15].

Alloy	Alloying elements	Application	Heat treatability
1xxx	None	Electrical conductors, chemical plant and architectural panels	Non-heat treatable
2xxx	Cu and Mg	Aircraft structures	Heat treatable
3xxx	Mn	Heat exchangers, packaging, architectural applications	Non-heat treatable
4xxx	Si	Architectural applications	Mostly non-heat treatable
5xxx	Mg	Car trim	Non-heat treatable
6xxx	Mg and Si	Wide field of applications, e.g. extrusions	Heat treatable
7xxx	Zn and Mg	Aircraft structures and hydraulic equipment	Heat treatable

2.1.1 Recycling

Due to the large energy demand and environmental impact related to primary Al production, recycling is both cost and environmental highly beneficial. In fact, as little as 5% of the energy demand in primary aluminium production is used in recycling of the material [1]. The Al can be remelted and recycled to new products numerous times without much material loss, in this respect Al can be looked upon as an energy bank. A consequence

of the high benefits of recycling, as much as 75% of all Al ever produced in the world is still in use in various products [1, 15].

However, as presented in Table 2.1, the various Al alloys contain different alloying elements. The properties of the alloys may be changed by the alloy composition. Trace elements are present in scrap Al, and these elements may influence the alloy characteristics. Even though many Al alloys are created with a good tolerance of impurity elements, the so-called recycling friendly alloys, other alloys are not. It is therefore important to control the trace elements in the recycled materials to control the material properties when Al is reused [1]. The Al scrap should be as pure as possible before remelting. After the initial collection and sorting of the scrap metal, various physical separation methods of the scrap Al are performed for purification purposes. These methods are for instance magnetic separation, air separation, spectrographic methods and eddy current separation. After the physical separation the metal is remelted and refining technologies, such as fluxing, are applied to remove impurities and further purify the material before processing to Al alloys for further use [17].

2.2 Strengthening mechanisms

The mechanical strength is a very important material property for the aluminium alloys. Strength may be measured in various ways, as will be described in Chapter 4.2. Commonly the tensile stress (force per area) is measured in relation to the strain (relative elongation) of a material rod when stretching it. The yield strength is defined as the stress point where the deformation goes from elastic to plastic. In the elastic regime the deformation is reversible, the atoms relax to their original positions after the stress is released. While in the plastic regime the force on the atoms is so large that a permanent displacement occurs. This permanent displacement is actually caused by the motion of dislocations, caused by the induced strain on the atoms of the material. Dislocations are lattice defects from the periodic atomic lattice, such as for instance an edge dislocation which is an extra half plane of atoms in the matrix. For fcc structures such as Al, $\{111\}$ plane dislocations are most common, with movement along a $\langle 110 \rangle$ direction. (The $\{111\}$ plane is the most closed packed plane, with largest planar spacing, and the $\langle 110 \rangle$ directions are the most closely packed directions.) The movement of such a dislocation plane in closed packed directions is called a slip system [18], as illustrated in Figure 2.1.

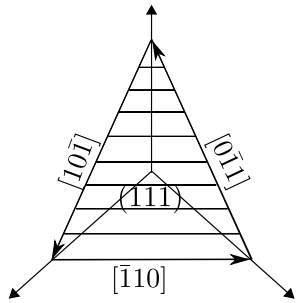

Figure 2.1: Slip systems of an fcc crystal, e.g. Al. Slip plane (111), and slip directions $[\bar{1}10]$, $[0\bar{1}1]$ and $[10\bar{1}]$. Figure adapted from [18].

Pure aluminium has a low strength compared to e.g. Fe [18]. Fortunately addition of alloying elements and thermal and/or mechanical treatments provide the possibility to design alloys with much higher strength. The strength of the aluminium alloys is to a large extent controlled by the number and mobility of the dislocations present to oppose plastic deformation of the material. In order to decrease the mobility of dislocations, internal stress must be introduced in the aluminium lattice to prevent their motion [18].

Four main hardening mechanisms are present for aluminium alloys [15]. *Work hardening*, or strain hardening, is a hardening mechanism introduced when the material is exposed to deformation. *Microstructure hardening* results from the blockage of dislocation movement by the grain boundaries or constituent particles. *Solid solution hardening* occurs when foreign atoms are dissolved in a lattice, acting as obstacles to the dislocation movement. The fourth hardening mechanism is *precipitation hardening*.

The heat-treatable, or age hardening, alloys are hardened after heating and cooling cycles by precipitation hardening. Alloying elements are dissolved into solid solution in the alloys at elevated temperatures where the solubility is high. Afterwards the alloy is rapidly quenched to a temperature well below the solvus line, resulting in a supersaturated solid solution and vacancies. A medium temperature or room temperature aging is applied in order to precipitate coherent metastable precipitates which result in high strength. The strength is induced by the need of a large strain for dislocation passage through the coherent phases. A small misfit between the coherent precipitates and matrix introduces more strain to hinder the dislocations and is therefore beneficial. At higher temperatures the equilibrium precipitates are formed. These are non-coherent and do not contribute to the precipitation hardening, such that an over aged condition is reached.

Non-heat treatable alloys gain strength through the three other hardening mechanisms, namely work hardening, microstructure hardening or solid solution hardening. During work hardening, or strain hardening, deformation of the material introduces a large amount of dislocations. Dislocations are associated with a long range stress field which is lowered by dislocation coupling. As the dislocations tangles up, they oppose further movement of dislocations. The strength of the metal increases with the square root of the dislocation density [18].

Microstructure hardening occurs when second phases act as dislocation blockage and effectively feeds the dislocations into the grain boundaries. The constituent phases are often related to grain boundaries. There is an inverse proportionality between grain size and yield strength, as given by the Hall-Petch equation. A fine grained structure will act as a larger obstacle to dislocation movement [18]. Also, finely distributed dispersoids precipitated during homogenisation from metastable solid solution will act as obstacles for recrystallisation [2, 3].

A foreign atom in the host lattice introduces chemical or elastic interaction with dislocations. As the chemical bonding is different between the host lattice and the foreign atom a dislocation-atom force is introduced. If the foreign atom is of an other size than the host lattice atoms a strain field is produced. The foreign atoms produce a restraining force upon the dislocation and will therefore act as atomic obstacles to dislocation movement. In general a square root relation between solute atom concentration and solid solution hardening is found [18].

2.3 Wrought 3xxx Al alloy system

The wrought non-heat treatable 3xxx alloys have been the topic of this thesis. These alloys have moderate strength and good workability. As briefly introduced in Table 2.1, the 3xxx alloys have various applications, e.g. beverage cans, heat exchangers, storage tanks, cooking equipment and architectural applications such as awnings, roofing and furniture. The main alloying element in the 3xxx alloys is Mn, together with Si and Fe. In addition Cu, Mg and Zn are also used in the alloy series [15].

The first processing step after the initial casting of the wrought alloys is the homogenisation. Before further mechanical processing a homogenisation is essential to eliminate micro segregation, reduce solid solution level of

Mn and get the right size and density of constituent particles and small dispersoids. The constituent particles and dispersoid distribution are very important as they will influence the further processing of the material [2–7, 19–22].

The constituent particles are formed during casting of the Al. Further growth and phase transformations may occur during homogenisation. The dispersoids precipitate during homogenisation. In the following, the emphasis will be on the stable dispersoid and constituent phases observed and studied in this thesis. However, other non-equilibrium phases are possible in the quaternary system, and also other phases are found in the binary (Al-Fe and Al-Mn) and ternary (Al-Mn-Si and Al-Fe-Si) systems [23]. These phases are not treated further as they were not studied in this thesis.

The cubic α-Al(Fe,Mn)Si phase and the orthorhombic Al_6(Fe,Mn) are formed in the commercial 3xxx alloys, possibly as both dispersoids and constituent phases. Both phases are rather complex, with 138 and 36 atoms in the unit cells respectively. Mn and Fe may freely interchange in both phases. In the following the two phases are presented in detail, and further on, how they act as constituents and dispersoids in the Al-Fe-Mn-Si alloy system studied here are explained.

α-Al(Fe,Mn)Si

The α-Al(Fe,Mn)Si phase is found both as constituent phases and dispersoids in the commercial 3xxx Al alloys. A high Si content in the Al-Fe-Si-Mn alloy favours the formation of the α-Al(Fe,Mn)Si phase [24], both as dispersoids and constituent phases. α-Al(Fe,Mn)Si dispersoids and constituent phases in commercial alloys with both Mn and Fe content have a mixture of Mn and Fe on certain atomic positions.

The Fe/Mn ratio governs the crystal structure and space group of the α-Al(Fe,Mn)Si phase. A low Fe/Mn ratio favours the simple cubic (sc) structure, characteristic for α-AlMnSi, with space group $Pm\bar{3}$ (#200) and lattice parameter 12.68 Å [25–27]. A high Fe/Mn ratio favours the body centred cubic (bcc) structure characteristic for α-AlFeSi, with space group $Im\bar{3}$ (#204) and lattice parameter 12.56 Å [28].

Figure 2.2 shows a projection of the α-AlMnSi unit cell with the sc structure ($Pm\bar{3}$) along two directions, [111] in a) and [001] in b). The Al atoms are red, the Si atoms yellow and the Mn atoms blue. The unit cell of the α-Al(Fe,Mn)Si phase consists of 138 atoms [25–27].

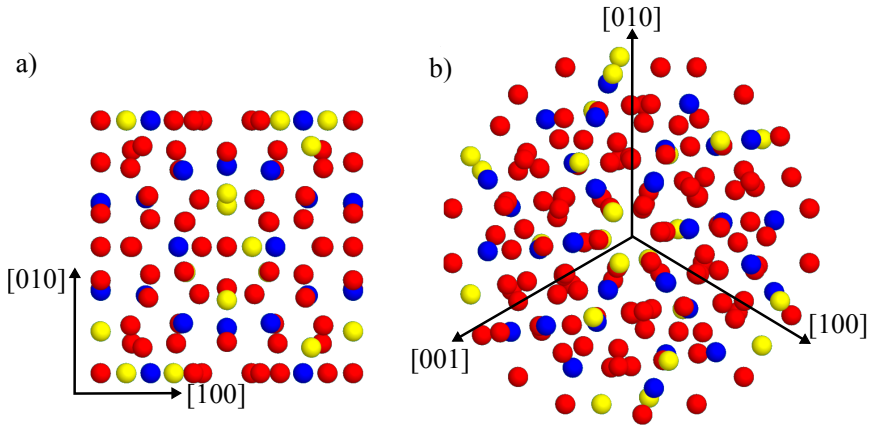

Figure 2.2: Projection of the α-AlMnSi unit cell along a) [111] α direction and b) [001] α direction. The Al atoms are red, the Si atoms yellow and the Mn atoms blue.

Two Mackay icosahedra [14] (MI) centred at (0 0 0) and ($\frac{1}{2}$ $\frac{1}{2}$ $\frac{1}{2}$) are the main structural parts of the unit cell of the α-Al(Fe,Mn)Si phase [12, 13]. The MI consists of 54 atoms, distributed in three polygon layers. The inner layer consists of an icosahedron containing a mix of Al and Si atoms. The next layer is also an icosahedron consisting of 12 Mn and/or Fe atoms. These icosahedra are surrounded by a shell of 30 Al atoms outside each of the 30 icosahedral two-fold edges, forming an icosidodecahedron [29]. The remaining 30 atoms may be considered to form outer shared shells binding the MIs together. This adds up to 138 atoms in the unit cell, and gives α-$Al_{96}(Fe,Mn)_{24}Si_{18}$. In Figure 2.3 the MI structure is shown. Figure 2.3 a) shows the inner Al/Si icosahedron, b) the next Fe/Mn icosahedron and c) the outer Al icosidodecahedron.

In the case of α-AlMnSi, the two inner part MIs consisting of Si and Al atoms, at 000 and $\frac{1}{2}\frac{1}{2}\frac{1}{2}$, are slightly structurally different [12, 25, 26]. The structure is close to a bcc structure, but one atomic Al site is not occupied at both 000 and $\frac{1}{2}\frac{1}{2}\frac{1}{2}$. Thus, the structure can not be described by a translation of $\frac{1}{2}\frac{1}{2}\frac{1}{2}$, which is characteristic for the bcc structure [28]. For the α-AlFeSi, the two inner Al/Si Mackay icosahedra are equivalent and therefore the structure is bcc, with space group $Im\bar{3}$ (#204) [28].

The α-Al(Mn,Fe)Si phase is a so-called "quasi crystalline" approximant. Investigating such approximant phases is important for better understanding the nature of quasi crystals. The transformation from icosahedral quasi

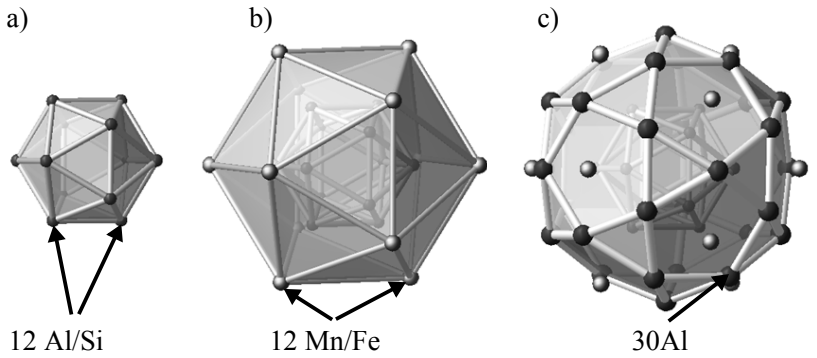

Figure 2.3: a) Inner Al/Si icosahedron. b) Middle Fe/Mn icosahedron. c) Outer Al icosidodecahedron. Figure adapted from [30].

crystalline (IQC) to crystalline α-phase for the Al-Mn-Si system has been treated in several studies [31–37]. The IQC will also be directly coupled to the mechanical properties of the alloys, as it is commonly the initially formed phase nucleating the dispersoids. In Paper III a model for the icosahedral ordering in the α-dispersoids in relation to Al is given in detail [38].

Al_6(Fe,Mn)

The Al_6(Fe,Mn) phase precipitates in the commercial 3xxx alloys when the Si content is low [4, 9–11]. It forms both constituent particles during solidification and dispersoids during homogenisation. Increasing the Si content leads to precipitation of the cubic α-Al(Fe,Mn)Si phase as the stable phase, as described in the previous section. The level of Si necessary to enhance the precipitation of α-Al(Fe,Mn)Si phase dispersoids is very low [9].

The crystal structure of the Al_6(Fe,Mn) phase is orthorhombic, with space group Ccmm (#63). Both Al_6Mn and Al_6Fe have the same space group. The Fe and Mn atoms may interchange freely in the unit cell. The unit cell of Al_6Mn has lattice parameters $a = 6.4978 \pm 0.0005$ Å, $b = 7.5518 \pm 0.0005$ Å and $c = 8.8703 \pm 0.0005$ Å [39], while the unit cell of Al_6Fe has lattice parameters $a = 6.464 \pm 0.0005$ Å, $b = 7.440 \pm 0.0005$ Å and $c = 8.779 \pm 0.0005$ Å [40]. Figure 2.4 shows projections of the orthorhombic Al_6Mn unit cell along [100] in a) and [001] in b).

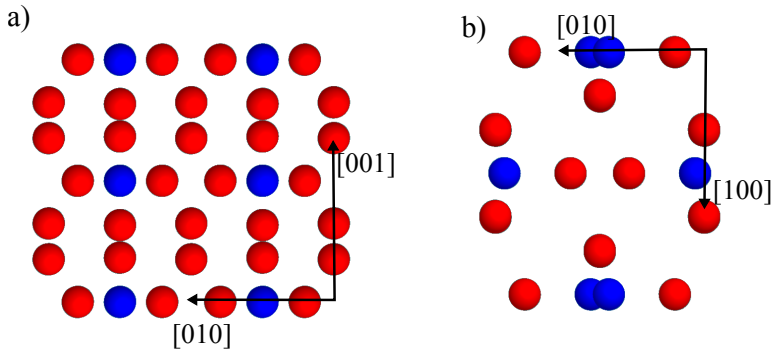

Figure 2.4: Projections of the unit cell of Al_6Mn. The projection is along [100] in a, and along [001] in b).

2.3.1 Constituent phases in the 3xxx Al-Fe-Mn-Si alloys

The constituent phases are very important as they influence recrystallisation, grain size, texture and mechanical properties of the final aluminium products [2, 3]. Constituent particles mainly form as interdendritic eutectic networks during solidification in the DC cast 3xxx Al alloys. With Mn, Fe and Si as the main alloying elements, two types of constituent particles are found in the commercial 3xxx alloys. The orthorhombic Al_6(Fe,Mn) phase and the bcc α-Al(Fe,Mn)Si phase are formed during solidification. The amount and proportion of alloying elements influence which phase will precipitate. A high Si content favours the formation of α-Al(Fe,Mn)Si, while the Al_6(Fe,Mn) phase predominates in alloys with low Si content [24].

The solid solution solubility of Fe in Al is very low. In alloys with a high Si content the constituent α-Al(Fe,Mn)Si phase will precipitate with a high content of Fe, as the solubility of Mn is higher than of Fe [15]. As described in Section 2.3, a high Fe content causes the α-Al(Fe,Mn)Si phase to have bcc crystal structure and space group $Im\bar{3}$.

Figure 2.5 shows a micrograph from a 3xxx alloy with high Si content after 24 hours homogenisation at 450 °C. The constituent α-Al(Fe,Mn)Si phases are located in the vicinity of grain boundaries, as indicated with the black arrows. The dispersoids are distributed in the surrounding matrix.

The Al_6(Fe,Mn) phase may transform to the bcc α-Al(Fe,Mn)Si phase during homogenisation heat treatment. If the Si level is sufficiently high, Si may diffuse from the matrix to the Al_6(Fe,Mn) surface and transform into the α-Al(Fe,Mn)Si and Al in solid solution through an eutectoid reaction [41–

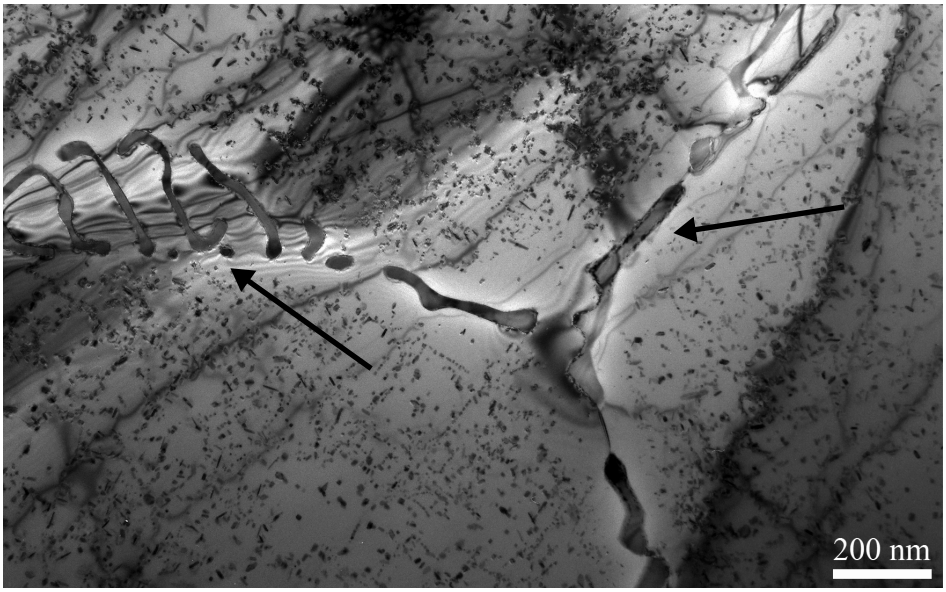

Figure 2.5: TEM micrograph showing the distribution of α-Al(Fe,Mn)Si phases, both as constituent and dispersoid phases in a 3xxx Al alloy after 24 hours homogenisation at 450 °C. The constituent phases are located at the grain boundaries (indicated with arrows) while the small dispersoids are distributed in the surrounding matrix.

47]. The fraction of transformed particles increases with homogenisation time and temperature [7, 46]. This transformation is important for further processing of the material. It will influence the formability, as the α-Al(Fe,Mn)Si phase is harder than the Al_6(Fe,Mn) phase. These two types of constituent phases are studied in Paper II [48].

2.3.2 Dispersoid phases in the 3xxx Al-Fe-Mn-Si alloys

The dispersoid phases are important due to their influence on the material properties of the 3xxx alloys. Dispersoids have been studied with respect to the material influence in numerous studies. Type, size, number density and distribution of dispersoids influence mechanical properties, recrystallisation recovery and deformation behaviour of the 3xxx Al alloys [2, 3, 6, 7, 19–22]. Also a hardening effect from the α-Al(Fe,Mn)Si dispersoids during low temperature homogenisation was found in this work (Paper I) [19, 20].

Si and Fe contents reduce the solubility of Mn in Al matrix and enhance

precipitation of dispersoids [4, 9, 47]. Two main types of dispersoids, the orthorhombic Al_6(Fe,Mn) and cubic α-Al(Fe,Mn)Si dispersoids, precipitate as stable phases in commercial 3xxx Al alloys. Composition and heat treatment govern the type of dispersoid to precipitate [4, 9–11, 47]. The two phases are the same as the constituent phases precipitated during solidification as described above. In commercial 3xxx alloys which contains Si, α-Al(Fe,Mn)Si dispersoids precipitate as the stable phase [41]. α-Al(Fe,Mn)Si dispersoids can be found in many Al alloy systems, and it is a very important dispersoid phase in Al alloys.

Figure 2.6 shows a distribution of α-Al(Fe,Mn)Si dispersoids after 450 °C homogenisation for 24 hours in an alloy with high Si and Mn content. The sizes and morphologies of the dispersoids are scattered in this orientation of the Al matrix. Due to the relatively long homogenisation time of 24 hours some dispersoids have grown to a relatively large size.

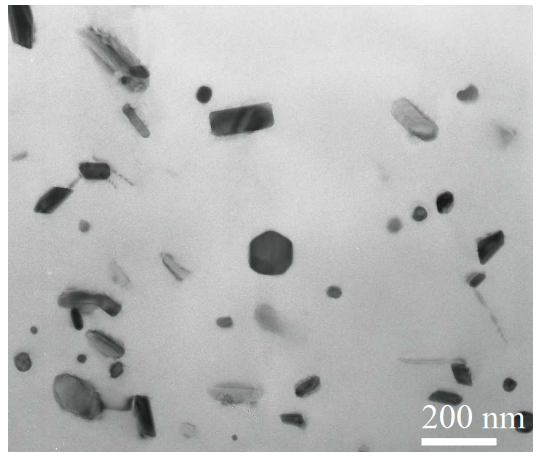

Figure 2.6: Distribution of α-Al(Fe,Mn)Si dispersoids after 450 °C homogenisation for 24 hours in an alloy with high Si and Mn contents.

In the as-cast state the majority of the Mn is in supersaturated solid solution [9]. The α-Al(Fe,Mn)Si dispersoid phase precipitate during homogenisation with a high Mn content and a sc structure, with space group Pm-3. During homogenisation Fe may diffuse into the dispersoids, however without changing the crystal structure in the alloys studied in this thesis. However, if the Fe/Mn ratio in the alloy is high, the dispersoids may have a bcc structure which is characteristic for α-AlFeSi, with space group $Im\bar{3}$ [49]. The lattice parameter of the α-Al(Fe,Mn)Si dispersoids are somewhere in between the lattice parameters determined for α-AlMnSi and α-AlFeSi, determined by

the Mn and Fe content, as shown in Paper II [48].

The Fe/Mn ratio governs the crystal structure and space group of the α-Al(Fe,Mn)Si phase. A low Fe/Mn ratio favours the sc structure, characteristic for α-AlMnSi, with space group $Pm\bar{3}$ (#200) and lattice parameter 12.68 Å [25–27]. A high Fe/Mn ratio favours the bcc structure characteristic for α-AlFeSi, with space group $Im\bar{3}$ (#204) and lattice parameter 12.56 Å [28].

Figure 2.7 a) shows an α-Al(Fe,Mn)Si dispersoid after 450 °C homogenisation for 24 hours in an alloy with high Si and Mn content. As can be seen in the diffraction pattern in the upper right corner, the dispersoid and matrix are both aligned along the [001] zone axes. As seen in the high resolution (HR) insert of Figure 2.7 b), the crystal structure of the α-Al(Fe,Mn)Si dispersoids is rather complex.

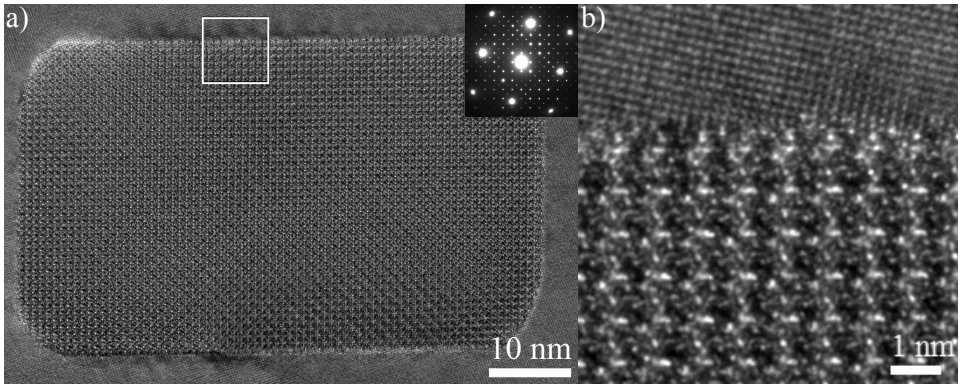

Figure 2.7: a) α-Al(Fe,Mn)Si dispersoid imaged along [001] zone axis for both Al and α-dispersoid, as seen in the diffraction pattern in the upper right corner. b) High resolution image of the area indicated by the square in a). The micrographs were taken in cooperation with Per Erik Wullum at a Jeol double corrected ColdFEG ARM200F.

In commercial 3xxx Al alloys with very low Si content, the Al_6(Fe,Mn) phase precipitates as the stable dispersoid phase [9, 11]. α-Al(Fe,Mn)Si dispersoids will also precipitate at low temperatures in the alloys with a very low Si content. At higher temperatures, due to the increased solubility of Mn in solid solution and the low Si content, the α-Al(Fe,Mn)Si phase becomes thermodynamically unstable and dissolves. As the α-Al(Fe,Mn)Si phase is the commonly observed dispersoid phase in commercial alloys, the Al_6(Fe,Mn) dispersoids will not be treated further in this thesis.

2.3.3 Alloys studied in this thesis

The alloys in this thesis were produced at Hydro Sunndalsøra and were a part of the alloy stock produced for the MoReAl project. The alloys were direct chill-casted. Table 2.2 shows the four alloys studied in this thesis, with main alloying elements. All alloys contains ∼0.5wt% Fe. A high and low Si contents (∼0.5 wt% and ∼0.15 wt%) are combined with high and low Mn content (∼1.0 wt% and ∼0.4 wt%).

Table 2.2: Alloys and main alloying elements (wt%) measured by mass spectroscopy.

Alloy	Mn (wt%)	Si (wt%)	Fe (wt%)
C1	0.39	0.15	0.53
C2	0.97	0.15	0.50
D1	0.40	0.49	0.52
D2	0.99	0.48	0.50

Samples were taken from the half radius locations of the ingots and cut into pieces. Various low temperature homogenisation treatments were performed, as presented in Figure 2.8.

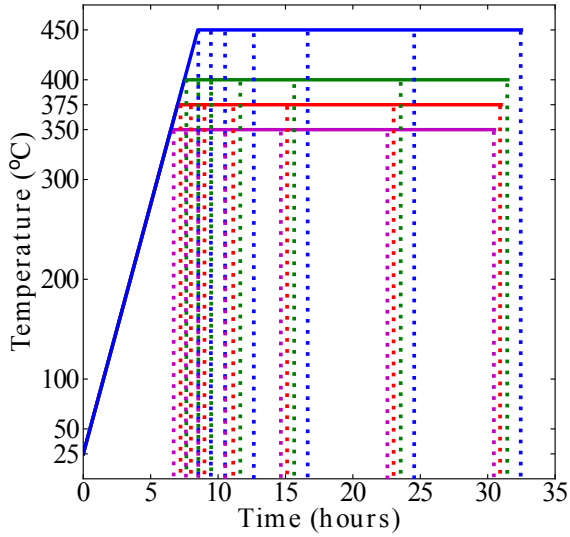

Figure 2.8: Heat treatments of alloys. The alloys were heated with a heating rate of 50 °C/hour, up to 350 °C, 375 °C, 400 °C and 450 °C, and annealed for 0, 1, 2, 4, 8, 16 and 24 hours before water quenching.

With a heating rate of 50 °C/hour, the materials were heated to 350 °C, 375 °C, 400 °C and 450 °C and annealed for 0, 1, 2, 4, 8, 16 and 24 hours, before quenched into cold water.

Chapter 3

Transmission electron microscopy

The main experimental tool for investigating the Al alloys in this thesis was the transmission electron microscope (TEM). A TEM is a powerful tool for characterisation and investigation of materials from atomic scale up to micrometre scale. Especially crystalline materials, which are not as beam sensitive as e.g. biological materials, can be studied in great detail.

The development of TEMs came due to the need of better resolution than what the regular light microscope could provide. Max Knoll and Ernst Ruska built the first electron microscope in 1932 [50]. Only four years after, the first commercial TEMs were available [51, 52]. The resolution of the first TEM was 50 nm, much better than the best optical microscopes. TEM turned out to be very useful for further development in nano- and material science.

In order to understand and exploit the TEM, a fundamental knowledge about electron interaction with matter is essential and the theory of electron diffraction is important. In the following single electron atom scattering is presented, followed by diffraction theory from a perfect crystal. Kinematic and dynamical diffraction theories are presented. These descriptions are not intended as a derivation of the theory, but are included to give a background for the diffraction work done in this thesis.

Further in this chapter, the transmission electron microscope will be presented, together with the TEM techniques relevant for the studies in this thesis. These are conventional TEM, high resolution TEM, scanning trans-

mission electron microscopy (STEM), Energy dispersive X-ray spectroscopy (EDX) and electron energy loss spectroscopy (EELS). Electron diffraction has been applied to investigate orientation relationships between the aluminium matrix and the constituent phases and the dispersoids. Therefore, this chapter presents the definitions of an orientation relationship and how it is found from a diffraction pattern (DP). STEM tomography have been an important technique in this thesis, resulting in Paper IV. The procedures of acquisition, alignment, reconstruction and visualisation of the tomography data are presented. At the end of the chapter TEM sample preparation is presented.

3.1 Electron interaction with matter

The high-energy electrons in the TEM leads to a wide range of interactions with matter. The various interactions are schematically shown in Figure 3.1. Most of these interactions can be detected in the TEM, and used in order to obtain information about the specimen under investigation [51]. Several of the signals have been used in this thesis, and will be described in the following sections.

The electrons in the TEM are typically accelerated to a kinetic energy of ∼200 keV. The speed of the electrons will then be 70% of the speed of light. The wavelength λ of the electrons is then approximately 0.0025Å, calculated from the de Broglie equation, with the relativistic effects taken into consideration

$$\lambda = \frac{h}{\sqrt{2m_0eE(1+\frac{eE}{2m_0c^2})}}. \tag{3.1}$$

Where h is Planck's constant, m_0 the rest mass of the electron, e the elementary charge, c the speed of light and E the accelerating potential of the TEM [51]. These fast accelerated electrons of the TEM open up the possibility to study materials all the way down to atomic scale and beyond.

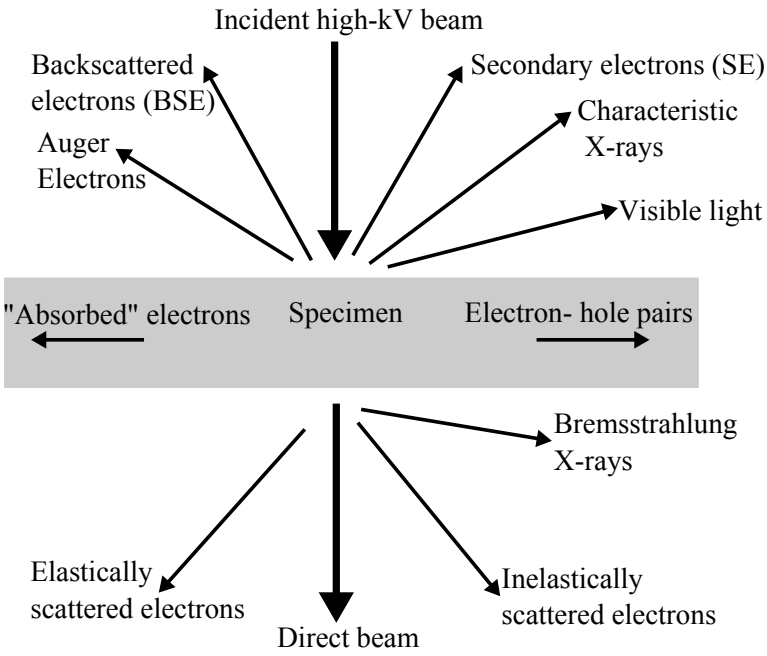

Figure 3.1: Electron beam interaction with a thin specimen of material. The directions of the different types of interactions are relative to direction of detection. The figure is adapted from [51].

3.1.1 Elastic scattering by a single atom

Initially, one may consider the scattering by a single atom. Elastic scattering by an atom does not change the energy state of the atom. If the incident electrons are fast, as they are in the TEM, the incident electrons will be scattered by the atomic potential. The Schödinger equation describes the quantum mechanical interaction of the electron, with accelerating potential E, with the atomic potential $V(\mathbf{r})$ [53].

$$\nabla^2\psi(\mathbf{r}) + \frac{8\pi^2 me}{h^2}[E + V(\mathbf{r})]\psi(\mathbf{r}) = 0. \tag{3.2}$$

The wave function of the electron, $\psi(\mathbf{r})$, is the sum of an incoming plane wave and the scattered wave at an angle 2θ from the incident plane wave

$$\psi = \exp(2\pi ikz) + f(\theta)\frac{\exp(2\pi ikr)}{r}. \tag{3.3}$$

Here $f(\theta)$ is the atomic scattering amplitude a unit distance r away from the atom, and $k = \frac{2\pi}{\lambda}$ is the wave vector of the incoming wave. The resulting

scattering intensity is given by

$$I(\theta) = |f(\theta)|^2 . \tag{3.4}$$

The scattering intensity is an actual measurable quantity in the TEM, the atomic scattering amplitude is therefore an important parameter.

If the scattering amplitude of the scattered wave is much smaller than the incoming wave amplitude ($V(\mathbf{r}) << E$) the first Born approximation may be applied to find an expression for the atomic scattering amplitude. A scattering vector $\mathbf{K'} = \mathbf{k'} - \mathbf{k}$ is defined as the difference vector between the incoming and outgoing wave vectors $\mathbf{k}$ and $\mathbf{k'}$ respectively. By assuming weak scattering and that the distance to the point of observation $\mathbf{r}$ is much larger than the atomic distances, the scattering amplitude in the direction of the scattering vector is given by

$$f^B(\mathbf{K'}) = \frac{2\pi me}{h^2} \int_{-\infty}^{\infty} V(\mathbf{r}) \exp(-2\pi \mathbf{K'} \cdot \mathbf{r}) \mathrm{d}\mathbf{r}. \tag{3.5}$$

The first Born approximation expresses the scattering amplitude as the Fourier transform of the scattering potential. It is noted that for scattering of fast electrons in crystals, the weak scattering assumption in the Born approximation is not valid. For further reading, see [53].

3.1.2 Diffraction by a perfect crystal

A natural next step is to extend the system from one atomic scattering event to the scattering from a perfect periodic crystal. A Bravais lattice is an infinite array of discrete points, defined by the lattice vector in real space

$$\mathbf{r}_i = u_i \mathbf{a}_1 + v_i \mathbf{a}_2 + w_i \mathbf{a}_3, \tag{3.6}$$

where $\mathbf{a}_1$, $\mathbf{a}_2$ and $\mathbf{a}_3$ are the primitive vectors of the Bravais lattice which span the lattice, and u, v and w are integers.

The scattered waves from each atom will interfere with each other creating diffraction maxima and minima. Conditions for diffraction maxima are stated in Bragg's law

$$2d \sin\theta = n\lambda. \tag{3.7}$$

Here θ is the scattering angle, n an integer representing the order of the diffraction and d the distance between the atomic planes. The atomic lattice plane d is defined by the Miller indices (h k l), which are integer numbers

inversely proportional to the axes intersections. For a cubic crystal, the distance between the atomic planes is given by the Miller indices and the lattice parameter a [51, 54]

$$d_{hkl} = \frac{a}{\sqrt{h^2 + k^2 + l^2}}. \tag{3.8}$$

The equivalent to Bragg's law in reciprocal space is the Laue conditions. Constructive interference will occur when the scattering vector **K'** equals the reciprocal lattice vector **g**, i.e.

$$\mathbf{K'} = \mathbf{k}' - \mathbf{k} = \mathbf{g}. \tag{3.9}$$

The lattice vector **g** in reciprocal space is given as

$$\mathbf{g} = h\mathbf{b}_1 + k\mathbf{b}_2 + l\mathbf{b}_3, \tag{3.10}$$

where $\mathbf{b}_1$, $\mathbf{b}_2$ and $\mathbf{b}_3$ are the reciprocal lattice vectors of the Bravais lattice defined as [54]

$$\mathbf{b}_1 = \frac{\mathbf{a}_2 \times \mathbf{a}_3}{\mathbf{a}_1(\mathbf{a}_2 \times \mathbf{a}_3)},\ \mathbf{b}_2 = \frac{\mathbf{a}_3 \times \mathbf{a}_1}{\mathbf{a}_1(\mathbf{a}_2 \times \mathbf{a}_3)} \text{ and } \mathbf{b}_3 = \frac{\mathbf{a}_1 \times \mathbf{a}_2}{\mathbf{a}_1(\mathbf{a}_2 \times \mathbf{a}_3)}. \tag{3.11}$$

Each lattice point in reciprocal space corresponds to a set of parallel atomic planes with indices (h k l) in real space.

In order to have a diffraction maximum, the Laue equations for diffraction must be satisfied in all three directions simultaneously

$$\begin{aligned} \mathbf{a}_1 \cdot (\mathbf{k} - \mathbf{k}') &= \mathbf{a} \cdot \mathbf{g} = n_1, \\ \mathbf{a}_2 \cdot (\mathbf{k} - \mathbf{k}') &= \mathbf{b} \cdot \mathbf{g} = n_2, \\ \mathbf{a}_3 \cdot (\mathbf{k} - \mathbf{k}') &= \mathbf{c} \cdot \mathbf{g} = n_3. \end{aligned} \tag{3.12}$$

n_1, n_2 and n_3 are integers. A useful visualisation of the Laue condition is the Ewald sphere construction. Figure 3.2 a) shows a 2D projection of an Ewald sphere at exact diffraction condition. The Ewald sphere is constructed by plotting the reciprocal lattice and drawing the incoming wave vector **k** to a lattice point. Constructive interference occurs if a circle with origin in the starting point of **k** and radius $|\mathbf{k}|$ intersects a reciprocal lattice point. The direction of the diffracted beam is determined by $\mathbf{k}'$, and the lattice vector in reciprocal space, **g**, is given in Equation 3.9, as shown in Figure 3.2 a) [51, 53, 54].

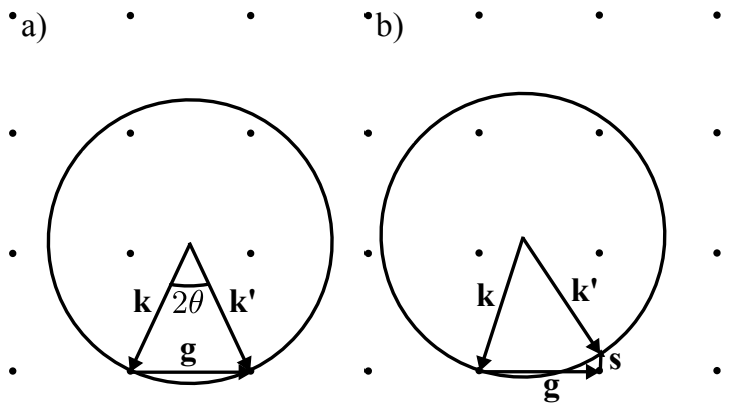

Figure 3.2: 2D projection of an Ewald sphere, in a) at Laue condition, and in b) slightly deviating from diffraction condition. The Figure is reproduced from [53].

Kinematic diffraction

In the kinematical theory of diffraction the crystal is considered a weak scattering object, and only one scattering event is considered. This assumption is reasonable for explaining the geometry of diffraction, however not for the scattered intensities.

The amplitude scattered by a unit cell in direction ($\mathbf{k}$+$\mathbf{g}$) is defined as the structure factor [53]

$$F(\mathbf{g}) = \sum_i f_i^B(\mathbf{g}) \exp(-2\pi \mathbf{g} \cdot \mathbf{r}_i). \tag{3.13}$$

Here the sum is over all atoms in the unit cell, and $\mathbf{r}_i$ is the position of atom i in the unit cell. The atomic scattering amplitude $f_i^B(\mathbf{g})$ is given by the first Born approximation in Equation 3.5. The structure factor of Al will be treated further in Section 3.2.2.

The next step is to sum over all unit cells in the crystal, but also small deviations from the Laue condition and Bragg's law must be taken into account. For fine crystals there will be diffracted intensity also in other directions than exact Bragg reflection directions.

In Figure 3.2 b) a small deviation from the Laue condition is shown, introducing the deviation vector $\mathbf{s}$

$$\mathbf{k}' - \mathbf{k} = \mathbf{g} + \mathbf{s}. \tag{3.14}$$

Here, the reciprocal deviating vector $\mathbf{s}$, with components s_1, s_2 and s_3, is given by

$$\mathbf{s} = s_1\mathbf{b}_1 + s_2\mathbf{b}_2 + s_3\mathbf{b}_3. \tag{3.15}$$

The total amplitude scattered by the crystal, $\mathrm{A}(\mathbf{s})$, in the direction of $\mathbf{k}'$, to a point $\mathbf{r}$ is then a summation over all the unit cells of the crystal

$$A(\mathbf{s}) = r^{-1}F_g \sum_j \exp(-2\pi\mathbf{r}_j \cdot (\mathbf{g} + \mathbf{s})) = r^{-1}F_g \sum_j \exp(-2\pi\mathbf{r}_j \cdot \mathbf{s}). \tag{3.16}$$

The intensity scattered in the direction of $\mathbf{k}'$ will then be given by

$$\begin{aligned} I(\mathbf{s}) &= A(\mathbf{s})A^*(\mathbf{s}) \\ &= \left(\frac{F_g}{r^2 V_{\text{cell}}}\right)^2 \left(\frac{\sin \pi A s_1}{\pi s_1}\right)^2 \left(\frac{\sin \pi B s_2}{\pi s_2}\right)^2 \left(\frac{\sin \pi C s_3}{\pi s_3}\right)^2. \end{aligned} \tag{3.17}$$

A, B and C are cell dimensions and V_{cell} is the volume of the unit cell.

Due to the short penetration of electrons through a crystal, the TEM specimen must be thin. Typically, the sample is a thin plate with thickness $C = t$. The two lateral directions A and B are much larger, and therefore Equation 3.17 can be simplified to [53]

$$I(\mathbf{s}) = \frac{ABF_g^2}{r^2 V_{\text{cell}}^2} \left(\frac{\sin \pi t s_3}{\pi s_3}\right) \delta(s_1)\delta(s_2). \tag{3.18}$$

The scattered intensity is then spread around a maximum, normal to the crystal. This finite distribution of intensity is represented by the so called rel-rods in the Ewald sphere construction, which means that each reciprocal lattice point are represented by a line of length t^{-1} normal to the specimen.

The intensities of the diffracted beams g can be found by integrating Equation 3.18 over a sphere in reciprocal space around the diffracted beam direction. The resulting absolute intensity for a crystal of thickness t is then

$$I_g(t) = \left(\frac{\pi}{\xi_g}\right)^2 \left(\frac{\sin \pi t s}{\pi s}\right)^2, \tag{3.19}$$

where ξ_g is the extinction length, defined as two times the distance providing unit amplitude of the scattered intensity

$$\xi_g = \pi k V_{\text{cell}} \cos\theta / F_g(2\theta). \tag{3.20}$$

If the crystal is at exact Bragg condition, and the intensity in the diffracted beam $I_g(t) \leq 1$, the maximum thickness for the kinematical theory to be valid, is $t_{\max} \leq \frac{\xi_g}{\pi}$. For the accelerated electrons in the TEM, the extinction length is in the range of ∼100 nm, and also a realistic intensity in the scattered beam is much less than 1. Therefore a sample thickness in the range of ∼5-10 nm is needed for kinematical theory to be valid. For typical TEM sample thicknesses of ∼100 nm, multiple scattering must be considered, and dynamical theory should be applied [51, 53].

Dynamical diffraction

As a consequence of the breakdown of kinematic theory for realistic TEM sample foil thicknesses of ∼100 nm, dynamical diffraction must be considered. One approach is to represent the wave function $\psi(\mathbf{r})$, in the Schrödinger equation (3.2), as a linear superposition of Bloch waves

$$\psi(\mathbf{r}) = \sum_g C_g \exp[2\pi i(\mathbf{k}+\mathbf{g})\cdot\mathbf{r}], \tag{3.21}$$

where C_g is the Bloch wave coefficients. A first approximation is to include two reflections. The direct beam and one reflection in direction $(\mathbf{k}+\mathbf{g})$ is included in this two beam approximation. The wave function in Equation 3.21 will then be given by

$$\psi(\mathbf{r}) = C_0 \exp[2\pi i\mathbf{k}\cdot\mathbf{r}] + C_g \exp[2\pi i(\mathbf{k}+\mathbf{g})\cdot\mathbf{r})]. \tag{3.22}$$

The periodic potential of a perfect crystal can be constructed as a Fourier series

$$V(\mathbf{r}) = \sum_{-\infty}^{\infty} V_g \exp(2\pi i\mathbf{g}\cdot\mathbf{r}). \tag{3.23}$$

Solving the Schrödinger equation (3.2) when including the periodic potential in Equation 3.23 and the wave function $(\psi(\mathbf{r}))$ in Equation 3.22 lead to the following intensities [53]

$$I_0(t) = 1 - I_g(t),\ I_g(t) = \left(\frac{\pi}{\xi_g}\right)^2 \left(\frac{\sin\pi t s'}{\pi s'}\right)^2. \tag{3.24}$$

Here, $I_0(t)$ is the incident intensity, and $I_g(t)$ is the diffracted beam intensity for a specimen of thickness t. ξ_g is the extinction length, as defined in Equation 3.20 (except k is exchanged with K, which is the mean wave vector of the fast electrons within the crystal). The extinction length is now defined as the inverse of the separation of the two wave vector solutions. Here, $s' = \sqrt{(s^2 + \xi_g^{-2})}$ is the effective deviation from Bragg condition in the dynamical two beam approximation.

Comparing Equation 3.19 and Equation 3.24 shows that s' is the only difference. Close to the Bragg condition, s will be small and s' will be significantly different from s. When varying the thickness, there is an interchange of energy between the two beams (the direct beam and the diffracted beam) which needs to be taken into account.

It is worth mentioning that also the two beam approximation is a simplification. For high voltages, as in the TEM, a many beam theory, with an algebraic extension of the two beam approximation needs to be considered. Further derivations can be found in Humphreys [53].

3.2 The transmission electron microscope

The TEM consists of an electron gun, a lens system, the specimen chamber and the detection units. In addition a high tension (HT) voltage source, a cooling system and a vacuum pumping system are essential parts of the microscope. A schematic simplified drawing of a TEM column is shown in Figure 3.3.

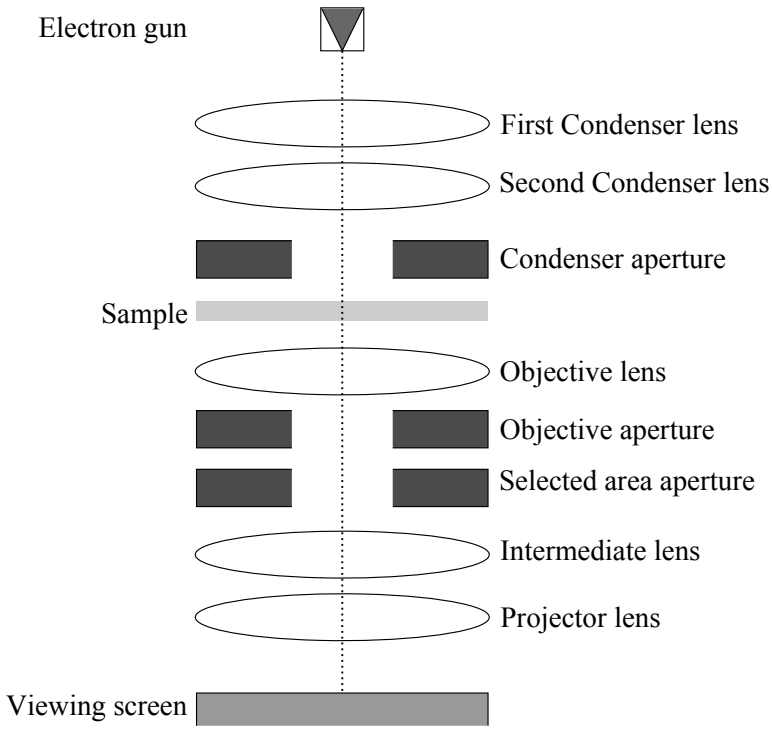

Figure 3.3: Schematic drawing of a TEM.

Two types of electron sources are used in the TEM, thermionic sources or field-emission sources. A thermionic source produces electrons when heated. In modern TEMs, LaB_6 crystals are used as thermionic electron guns. The field- emission gun source is usually a fine needle tip made of tungsten [51].

The lenses in a TEM are magnetic electron lenses. They consist of two pole pieces, where each is a cone with a core of soft magnetic material with a coil of copper surrounding it. An axially symmetric magnetic field, used to control the electron flow, is created when a current runs through the coil.

The condenser lenses are the first lenses after the electron source, as illustrated in Figure 3.3. They are used to form an electron beam with the desired properties of the electrons entering the specimen. The electron beam may either be converged to a small spot, a set of parallel rays or a divergent cone on the specimen. After the interaction with the specimen, the objective lens forms the first image, and is a very important lens in the TEM. The image formed by the objective lens is further magnified and projected to the viewing screen by the intermediate and projector lenses [51, 52].

There are three main lens imperfections which limit the resolution in the TEM. These are spherical aberration, chromatic aberration and astigmatism [51]. Spherical aberration C_s is caused by the varying strength of the electromagnetic lens in the off axis direction. The further away the electrons are from the optical axis in the lens, the stronger the electrons are deflected. As a consequence, all electrons will not be focused in the same plane. A point like object will then be imaged as a disc. The spherical aberrations can be corrected, and have improved the resolution of modern TEMs substantially. Electrons with different energy will be deflected with various strength in the objective aperture. This causes a chromatic aberration C_c which leads to a blurring of the object into a disc in a similar way as with the spherical aberration. The non-uniform magnetic field caused by imperfections in the pole pieces and the introduction of non-centred or contaminated apertures lead to astigmatism. By applying stigmators the astigmatism can be compensated for. Stigmators are small octupoles which introduce a compensating field to the deviations caused by the astigmatisms.

3.2.1 Conventional TEM

Imaging and diffraction are the two basic modes of the TEM. Figure 3.4 shows schematic drawings of the imaging a) and the diffraction b) modes. In imaging mode the image plane of the objective lens is projected down to the screen or detection unit. Then the intermediate lens is adjusted so that the image plane of the objective lens is the object plane of the projector lens. When forming an image, an objective aperture is inserted in the back focal plane of the objective aperture. If the objective aperture is centred around the direct beam of the diffraction pattern, a bright field (BF) TEM image is produced. If one of the diffracted spots is selected, a dark field (DF) image is the result.

The contrast mechanisms in BF and DF images are so called amplitude contrast mechanisms, these are diffraction contrast and mass-thickness con-

trast. Diffraction contrast is dominating for thin crystalline specimens. Diffraction contrast arises due to orientation of the sample or bending effects. Bending effects are caused by changed orientation of the lattice planes, due to for instance phase changes, grain boundaries, stacking faults or strain. Diffraction contrast can therefore be used to distinguish between different phases and provide help in orienting the specimen. Mass-thickness contrast arises due to difference in specimen thickness and atomic number Z. This contrast mechanism is most relevant for non-crystalline samples.

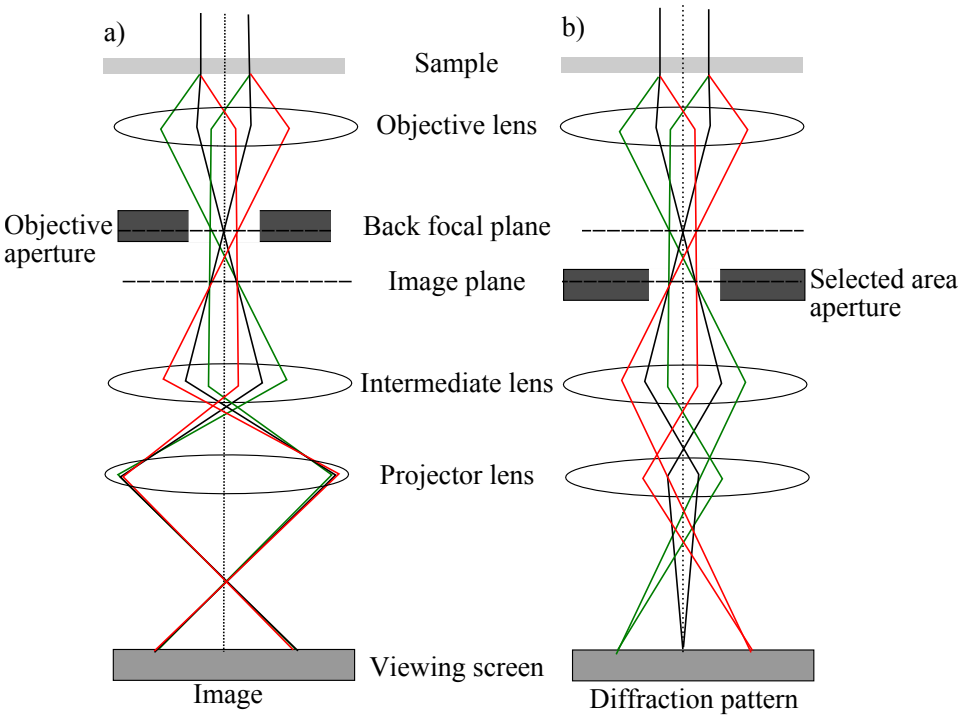

Figure 3.4: a) Imaging mode with objective aperture, producing a BF image. The image plane of the objective lens is projected down to the detection unit. b) Diffraction mode with SA aperture inserted. The back focal plane of the objective lens is projected down to the detection unit. Drawings are adapted from [51].

In diffraction mode the back focal plane of the objective lens is projected down to the screen or detection unit. This means that the intermediate lens is adjusted so that the back focal plane of the objective lens acts as the object plane of the intermediate lens. If a specific area of the sample is intended to contribute to the diffraction pattern, a selected area aperture

(SA) can be inserted in the image plane of the objective aperture, resulting in selected area diffraction pattern (SADP) .

3.2.2 Diffraction pattern analysis

The DP contains the intensity distribution in the diffracted spots as described in Section 3.1.2. DPs are very useful as they contain all information about the orientation of the crystal relative to the electron beam. And if more than one phase is included into the sample area under investigation, information about the orientation relationship between the phases is also contained in the DP. In the following section the importance of the structure factor and the routine for indexing a DP and defining an OR are described.

The structure factor of aluminium

The structure factor, given in Equation 3.13, defines the resulting reciprocal lattice from a material. The actual reciprocal lattice of a crystal consists of the reciprocal lattice point where the structure factor $F_{\mathbf{g}} \neq 0$. This means that the reciprocal Bravais lattice defined in Equation 3.11 differs from the real reciprocal lattice of the crystal because the structure factor $F_{\mathbf{g}}$ is zero, for some reciprocal lattice vectors $\mathbf{g}$. These reflections are known as kinematically forbidden reflections.

Aluminium has a fcc structure, containing four atoms in the unit cell. The atoms have the atomic coordinates

$$\mathbf{r}_1 = (0,0,0), \mathbf{r}_2 = \left(\frac{1}{2},\frac{1}{2},0\right), \mathbf{r}_3 = \left(\frac{1}{2},0,\frac{1}{2}\right), \mathbf{r}_4 = \left(0,\frac{1}{2},\frac{1}{2}\right). \tag{3.25}$$

For a given reciprocal lattice vector $\mathbf{g}$, as defined in Equation 3.10, the structure factor will be

$$\begin{aligned} F(\mathbf{g}) &= \sum_i^4 f_{\mathrm{Al}}(\mathbf{g}) \exp(-2\pi(hu_i + kv_i + lw_i)) \\ &= f_{\mathrm{Al}}(\mathbf{g})(1 + \exp(\pi i(h+k)) + \exp(\pi i(h+l)) + \exp(\pi i(k+l)). \end{aligned} \tag{3.26}$$

f_{Al} is the atomic scattering amplitude for Al [51, 54], and h, k, l are positive integers. The resulting structure factor of Al is then

$$\begin{aligned} F(\mathbf{g}) &= 4f_{\mathrm{Al}} \text{ if } h,k,l \text{ are all odd or all even,} \\ F(\mathbf{g}) &= 0 \text{ if } h,k,l \text{ are mixed odd and even.} \end{aligned} \tag{3.27}$$

Indexing diffraction patterns

The next step is to index the reciprocal lattice vectors **g** in the diffraction pattern. Figure 3.5 illustrates the geometry for diffraction patterns in the TEM.

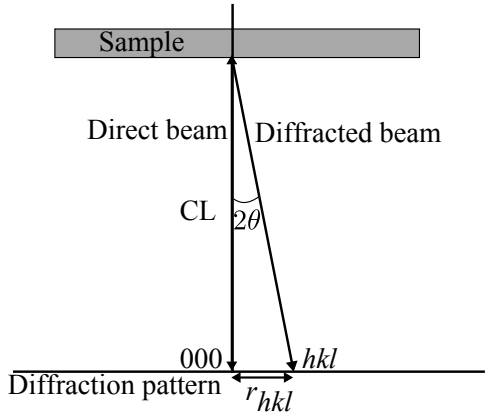

Figure 3.5: Geometry when acquiring diffraction patterns in the TEM.

The scattering angle 2θ is defined as the angle between the direct beam and the diffraction spot hkl, a distance r_{hkl} from the central spot 000. CL is the camera length. Bragg's law in Equation 3.7, the atomic distance d given in Equation 3.8, and the geometry consideration $\tan 2\theta = r_{hkl}/\mathrm{CL}$ from Figure 3.5 may now be combined. When taking into consideration that θ is very small, the following expression for the sum of hkl results

$$h^2 + k^2 + l^2 = \left(\frac{r_{hkl} \cdot a}{\lambda \cdot \mathrm{CL}}\right)^2 . \tag{3.28}$$

As all quantities on the right hand side are either constants or measurable in the diffraction pattern, this equation can be used directly when analysing DP. CL and λ are given by the microscope, and the distance r_{hkl} can be measured in the diffraction pattern. The combination of Equation 3.28 with the extinction rules in Equation 3.27 is needed to index the reflections in a diffraction pattern. It is also very useful to compare the ratio of distances between two spots with the measured ratio between r_{hkl} distances to check for correct indexing.

Figure 3.6 a) shows a simulated diffraction pattern of the $[1\bar{1}1]_{\mathrm{Al}}$ zone axis with indexed reflections. The direction of the specimen $[uvw]$, i.e. the zone axis, is determined by the cross product of two reflections, e.g. $\mathbf{g}_{\bar{2}02} \times \mathbf{g}_{022}$,

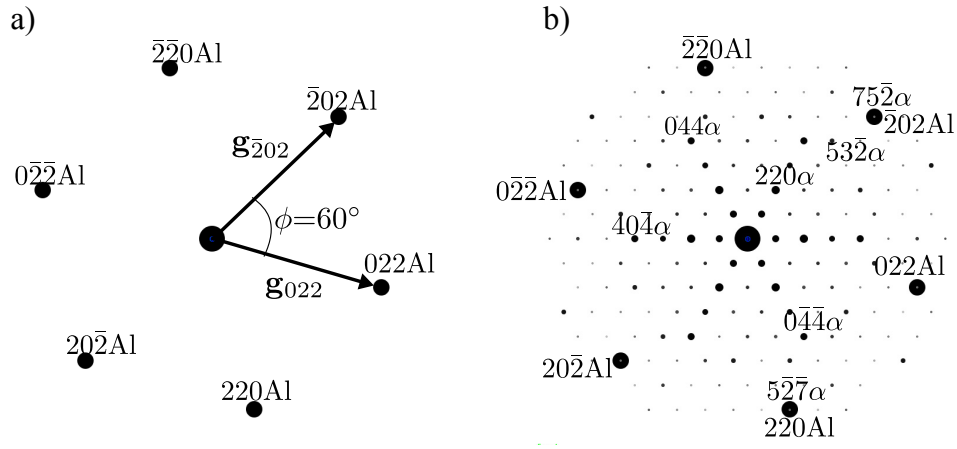

Figure 3.6: a) Simulation of $[1\bar{1}1]_{\mathrm{Al}}$ zone axis diffraction pattern. b) Combined diffraction pattern of the Al and the α-Al(Fe,Mn)Si phase.

see Figure 3.6 a). All reflections are perpendicular to the zone axis, such that this is an easy way to control if the indexing is correct. In addition, the angle between two diffraction spots should be calculated from the expression $\cos\phi = \frac{\mathbf{g}_{\bar{2}02} \cdot \mathbf{g}_{022}}{|\mathbf{g}_{\bar{2}02}||\mathbf{g}_{022}|}$, and compared with the physical angle ϕ measured in the diffraction pattern, also illustrated in Figure 3.6 a).

In Figure 3.6 b) the combined diffraction pattern of Al and the α-Al(Fe,Mn)Si phase is simulated. When two phases are present in the same diffraction pattern, the indexing quickly becomes more complicated. However, the difference in lattice parameter and the symmetry of the patterns make it possible to distinguish between reflections belonging to the different phases. An additional complicating factor is the presence of double diffraction, scattering by two planes in the same phase or two planes in two phases.

How the crystal structure of two phases are oriented in relation to each other are defined by the orientation relationship, which can be determined from the combined diffraction pattern of the two phases. The notation for planes, directions and reflections in both reciprocal and real space are given in Table 3.1. For cubic systems real and reciprocal lattice vectors with the same indices are parallel. As an example the reciprocal direction $(022)_{\mathrm{Al}}$ is perpendicular to the real space plane $(022)_{\mathrm{Al}}$, and these two vectors are parallel.

To define the OR uniquely both parallel directions (zone axis $[uvw]$ in real space) and parallel planes ((hkl) in real space) must be determined. An OR

Table 3.1: Notation of planes, directions and reflections in real and reciprocal space [51].

Real space	Reciprocal space	Notation
Particular direction	Particular plane	$[uvw]$
General direction	General plane	$\langle uvw \rangle$
Particular plane	Particular direction	(hkl)
General plane	General direction	$\{hkl\}$
Diffracting plane	Indexed reflection	hkl

will be given in the form

$$[uvw]_{\text{matrix}} // [uvw]_{\text{particle}}, (hkl)_{\text{matrix}} // (hkl)_{\text{particle}}. \tag{3.29}$$

The OR given from the diffraction pattern in Figure 3.6 b) is then $[1\bar{1}1]_{\text{Al}} // [1\bar{1}1]_{\alpha}$, $(022)_{\text{Al}} // (2\bar{5}\bar{7})_{\alpha}$.
Paper III discusses how and why this is the most commonly observed OR for the α dispersoid phase [38].

3.2.3 High resolution TEM

High Resolution (HR) TEM imaging mode is a phase contrast imaging technique. The image is formed by the interference between the direct beam and the diffracted beams. The electrons scattered to the highest angles (high spatial frequencies) will produce the finest details in the images. These scattered electrons may have opposite phase compared to the direct beam, resulting in a contrast reversal which complicates the imaging. To understand this contrast reversal, an intensity or object transfer function for the image formation process is defined as [51]

$$T(\mathbf{u}) = A(\mathbf{u})E(\mathbf{u})2\sin(\chi(\mathbf{u})). \tag{3.30}$$

In this equation, $\mathbf{u}$ is a reciprocal lattice vector, the spatial frequency for a diffracted direction, and $A(\mathbf{u})$ the aperture function. The objective aperture cuts off high spatial frequencies due to the radius of the aperture. The chromatic effects of the objective lens and the spatial coherence of the electron gun are included in the envelope function $E(\mathbf{u})$. The envelope function causes the same effect as the aperture function, such that high spatial frequencies are damped out.

The phase distortion function $\chi(\mathbf{u})$ in Equation 3.30, is defined as

$$\chi(\mathbf{u}) = \pi\Delta f\lambda\mathbf{u}^2 + \frac{1}{2}\pi C_s\lambda^3\mathbf{u}^4 = \frac{2\pi}{\lambda}\left(C_s\frac{\lambda^4\mathbf{u}^4}{4} + \Delta f\frac{\lambda^2\mathbf{u}^2}{2}\right). \tag{3.31}$$

χ depends on the defocus value Δf chosen to form the image, the spherical aberration C_s, the wavelength of the electrons λ and the spatial frequency $\mathbf{u}$.

For negative $T(\mathbf{u})$ the phase contrast will be positive and atoms appear dark at bright background. An as large as possible spatial frequency area is wanted before at a given u, $T(\mathbf{u})$ becomes 0, as high spatial frequencies correspond to high spatial resolution. At this point no information is transmitted and for larger spatial frequencies the phase contrast is reversed. This point will represent the spatial resolution limit where the image can be directly interpreted [51].

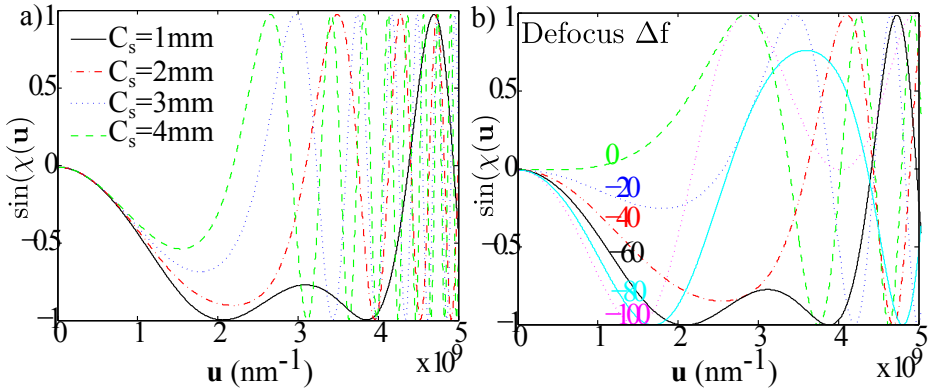

Figure 3.7: $\sin(\chi(\mathbf{u}))$ for a) Δ f=-60 nm and varying C_s, and b) for C_s=1 mm and varying defocus Δf.

Figure 3.7 a) shows $\sin(\chi(\mathbf{u}))$ at 200kV at a defocus Δf = -60 nm, with varying spherical aberration C_s. As can be seen from the figure, minimal spherical aberration is preferable. In Figure 3.7 b) $\sin(\chi(\mathbf{u}))$ is plotted with a spherical aberration C_s=1 mm and varying defocus values. Comparing defocus values of -60 nm and -80 nm shows that increasing the defocus too much reduces the spatial resolution. The crossover point will be positioned at lower spatial frequencies for defocus of -80 nm compared to -60 nm. The optimal balance between the spherical aberration with a negative value of focus Δf, is defined as the Scherzer defocus

$$\Delta f_{\mathrm{Sch}} = -1.2(C_s\lambda)^{1/2}. \tag{3.32}$$

At this defocus all the diffracted beams will have nearly a constant phase to the first phase contrast cross over. This is the best condition without a phase change. In state of the art TEMs today, multi pole lenses are used to correct for the spherical aberration, and Scherzers defocus can be circumvent.

3.2.4 Scanning transmission electron microscopy

In STEM mode the electron beam is converged and focused into a probe when hitting the sample. The electron probe is scanned across the sample in a raster and for each probe position the transmitted electrons are detected. Each pixel in the STEM image therefore corresponds to the integrated scattered intensity hitting the detectors for a certain probe position. In Figure 3.8 the STEM acquisition geometry is schematically illustrated. The magnification of the STEM image is determined by the size of the scanned area, and not by magnifying lenses as in the TEM mode. As no lenses are used after the specimen to form the image, the probe size is very important as it is the limiting factor for the spatial resolution in STEM mode. To optimise the probe size, alignment is important to get the desired quality of the image. Spherical aberrations in the lens forming the probe are affecting the probe size, therefore probe aberration corrected microscopes give better high resolution STEM images [55]. In this work, STEM has been used with tomography to determine dispersoid morphology in Paper IV [56]. High resolution was not needed or required for this work.

At each probe position on the specimen a convergent beam electron diffraction (CBED) pattern will be formed in the detector plane, which is the diffraction plane. The direct or scattered beam is used to form the image by choosing different detectors. Figure 3.8 shows the bright field (BF) and high angle annular dark field (HAADF) detector geometry in STEM mode.

A BF detector is used to detect the signal on the optical axis. The BF detector is a circular detector, see Figure 3.8, with a size smaller than the size of the direct beam CBED disc. In BF STEM the convergence angle of the beam may be adjusted to allow the CBED discs from the direct and diffracted beam to overlap. Where these discs overlap, there will be interference. The BF detector signal then corresponds to the central disc and its overlap regions with the first order diffraction discs [57]. The BF STEM images show phase contrast, as the HR TEM image, with a phase distortion function given in Equation 3.31. However, at low magnification

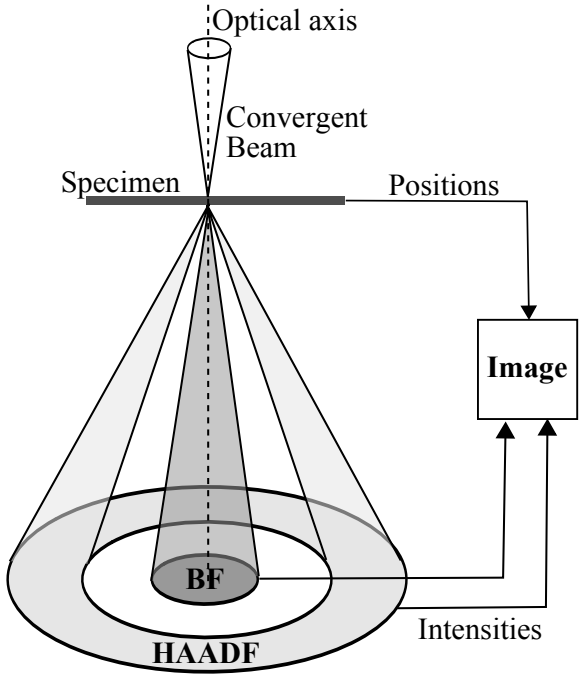

Figure 3.8: Schematic drawing of the STEM image acquisition geometry. The circular BF and annular HAADF detector geometries are shown.

BF STEM, diffraction and mass thickness contrast are present as for BF TEM.

The HAADF detector is an annular ring detector, see Figure 3.8, with an inner angle larger than 50 mrad. The high angle scattered intensity for each position of the probe when scanned over the sample is integrated over the detector. The high angle scattered electrons incidenting on to the HAADF detector consists of Rutherford scattered electrons, and thermally diffuse scattered electrons. Rutherford scattering is electron scattering by the atomic nuclei. Thermal diffuse scattering (TDS) is scattering to high angles through phonon interactions. These high angle scattered electrons are incoherent, and little or no phase contrast is present. Therefore the problem of contrast reversal due to dynamical diffraction is circumvent. The scattered intensity is highly dependent on the atomic number Z of the atoms in the specimen, and the image intensity is proportional to about Z^2 [58, 59].

3.2.5 STEM Tomography

Conventional (S)TEM only provides two dimensional (2D) projections of a three dimensional (3D) structure. To overcome this limitation tomography may be applied. The mathematical basis of tomography techniques used today are the Radon transform, the projection of an object into a lower dimensional space and its inverse form. It was published by Radon in 1917 [60], and is described below. The most well known application of 3D tomography reconstruction is the X-ray computerised tomography (CT) scanner for medical applications [61, 62]. Tomography techniques now have a wide range of applications in various fields, such as medicine, biology, nano technology and material research. TEM tomography was first applied to biological materials in 1968 [63–65]. Later it has been applied to study a wide range of materials, such as catalysts and metals [66].

The projection requirement states that the intensity of the 2D projections should vary as a monotonically function of the object that is reconstructed [67, 68]. The BF TEM signal is dominated by diffraction and mass thickness contrast. For thin and weakly scattering crystalline materials or amorphous samples it can be assumed that the mass thickness contrast dominates the signal and the projection requirement is fulfilled. Therefore, BF TEM imaging can usually be applied for amorphous and biological materials.

For crystalline samples, like Al, the diffraction contrast in BF mode degrades the quality of a tomography series significantly, as the diffraction contrast is not continuous through the tomography series and the projection requirement will not be fulfilled. However, for the HAADF STEM signal the intensity is approximately proportional to the atomic number Z^2 and the thickness of the sample, and the diffraction contrast component is limited for the high angle annular detector. Therefore the HAADF STEM signal is very well suited for tomography. Figure 3.9 illustrates the difference in contrast for the two imaging modes. As can be seen, the HAADF image of the α-Al(Fe,Mn)Si dispersoids in Figure 3.9 b) is much better suited for tomography than the corresponding BF TEM image in Figure 3.9 a).

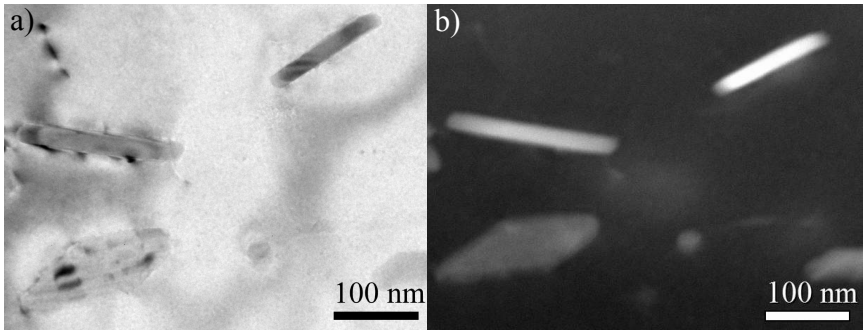

Figure 3.9: a) BF TEM and b) HAADF STEM images of α-Al(Fe,Mn)Si dispersoids.

Acquisition and alignment

In practice the acquisition of a tomography series in the TEM is performed by tilting the sample around one axis, with an as large as possible tilt range. Images are acquired at specified tilt intervals. Different geometries can be applied for the tomography acquisition, such as conical, dual tilt and single tilt acquisition. Single tilt acquisition is the most straight forward and commonly used technique [69]. For single tilt acquisition, the sample is tilted around one axis of the holder with predefined tilt steps θ. The sample is mounted in a dedicated tomography single tilt holder with a high tilt range of $\pm 80°$. The pole piece gap of the objective lens limits the possible tilt range, therefore the tomography holder tip is as thin as possible.

In order to obtain a high quality tilt-series, the area for investigations must be carefully selected. The chosen area should be tilted to high angles in order to check if the area can produce a good tilt series before the acquisition starts. The specimen thickness and possible shadowing from the holder or the sample provide possible limitations to the tilt range. The sample should not be too thick as the electron path length t is increased by a factor $t/\cos\theta$, when tilted an angle θ [70]. At the same time, if the sample is too thin, it may not contain complete features of interest. When an area with possibility for high tilting range is found, the tomography series can be acquired.

It is essential that the area imaged at each projection is the same and that the focus is maintained. Software routines for automatic positioning and focusing are available. However, manual adjustments for each tilting step are recommended to ensure an as high as possible quality of the acquired series. This is regarded as worthwhile as the subsequent processing of data

sets is rather time-consuming.

The alignment of the acquired projections is not perfect, neither by the automatic software routines or by manually alignment. Therefore, after acquisition of the tomography series, all the projections must be aligned before reconstruction. In projection, the relative position and shape of the object change during the acquisition of the tilt series. The two most common methods for alignment are cross correlation and fiducial markers. fiducial markers are common for biological samples, and are often realized by spherical colloidal gold particles which are dispersed as recognizable features in the sample. For samples with only special areas suited for analysis, as for Al, this method is difficult to use [68]. It would have been difficult to place the fiducial markers at the wanted positions. However, so-called land mark options are available in commercial software, recognizable features in the series are marked and these features are used for alignment [71]. Cross correlation routines can be applied for specimens like Al where fiducial markers are not very well suited. Cross-correlation algorithms can measure the shift between common features in the projections. Due to the change in object shape due to tilting, it should be carried out in a sequential way [57, 67, 69].

Also the tilt axis direction and position must be found, as the reconstruction algorithms use this information. If misaligned, arcs of intensity around the actual tilt axis will be the result. The individual projections should be rotated and shifted to minimize this effect [68, 69]. After alignment the projection series can be reconstructed.

Reconstruction

The Radon theorem states that a three dimensional object can be reconstructed from two dimensional projections [60, 72]. The Radon transform R_f is the mapping of a real space object D, described by a function $f(x, y)$, along all possible projection lines L

$$R_f = \int_L f(x, y) ds, \tag{3.33}$$

where ds is the unit length of L. The radon transform converts the point (x, y) in real space into a line in Radon space (l, θ), where l is the line perpendicular to the projection line L and θ is the projection angle. Inverting the Radon transforms of a continuous number of projections covering the whole angular space will then lead to a reconstruction of the object. The

inverse Radon transform is the basic principle of reconstruction algorithms as described above. Due to the discrete number of projections and limitations of the projection angle θ when acquiring a tomography series in TEM or STEM, the reconstruction will be imperfect. The goal of the tomography reconstruction is an as good as possible reconstruction despite these limitations [57, 68, 69, 73].

The projection slice theorem states that a projection at a given angle θ is a central slice through the Fourier transform of that object. The practical implementation of the Fourier reconstruction is however not only the simple inverse transform [57, 68]. The Fourier reconstructions are complicated to implement and will not be treated further.

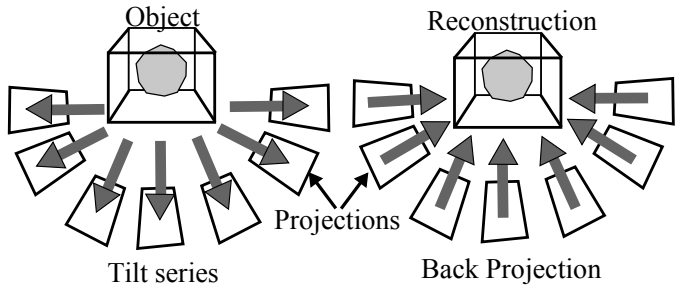

Figure 3.10: Schematic drawing of the back-projection reconstruction. Figure adapted from [70, 74]

An easier method to implement is the method of direct back-projection. This process is schematically shown in Figure 3.10. It is based on the principle that a point in space can be uniquely described by three lines passing through it. A complex object needs more lines to be uniquely defined, but the principle remains the same. The inverse of such a ray is a projection. By smearing out each projection at the given projection angle θ in the tilt series back into a 3D space, a line is generated that will uniquely describe the object in that projection direction. The superposition of all the back projected lines at different angles will generate the original object if the number of projections are sufficiently high [57, 74].

Each of the projection lines will intersect the Fourier space at zero frequency, as stated in the projection slice theorem. Figure 3.11 shows schematically the lines representing each of the projections, where θ is the projection angle and α is the maximum tilt range. The sampling frequency of each projection line is equal, but the amount of data close to the centre of the

Fourier space will have a much higher density, as illustrated in Figure 3.11. This results in a blurring of the reconstruction because of an enhancement of the low spatial frequencies, and suppression of high spatial frequencies. As described in Section 3.2.3, the high spatial frequencies are needed to obtain an as high as possible spatial resolution. The effect of uneven sampling of spatial frequencies can be corrected for by adding a weighting filter in the Fourier space to the simple back projection to improve the uneven frequency distribution due to higher sampling frequency near the centre of the Fourier space after back projection. This type of reconstruction is called a weighted back projection (WBP) [57, 68].

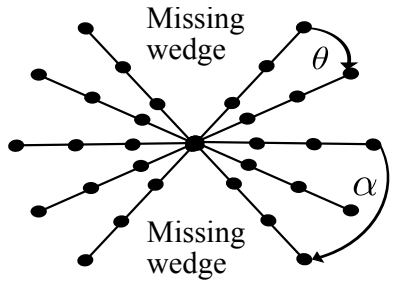

Figure 3.11: Illustration of the non uniform sampling in Fourier space. Figure adapted from [68].

Due to the limited number of projections a back projection is never perfect. If the reconstruction is reprojected along the projection angles, the reconstructed projections will not be identical with the original ones. The difference can be back projected into reconstruction space and used to correct the reconstruction. This process can be repeated iteratively to obtain an as good as possible fit between the original projections and the reconstruction. The algebraic reconstruction technique (ART), or simultaneous iterative reconstruction technique (SIRT) are the most commonly used iterative reconstruction algorithms [57]. In this work, the WBP was applied, as it gave the best reconstruction of the data. However, the SIRT and ART algorithms were also tested.

To obtain an as high as possible resolution in the reconstruction, the tilt range and number of projections should both be as large as possible. While the resolution parallel to the tilt axis is equal to the original resolution, the resolutions in the other perpendicular directions depend on the number of acquired projections N and the diameter D of the reconstructed area. The

resolution d is defined as [57, 75]

$$d = \frac{\pi D}{N}. \tag{3.34}$$

It is assumed that N reconstructions are spread out over an angle π. As illustrated schematically in Figure 3.11, the limited tilt range leads to a missing wedge of information [68]. In the direction parallel to the optical axis the resolution will be degraded further because of the missing wedge of information. The resolution is degraded by an elongation factor related to the maximum tilt angle. The elongation e in the direction of the missing wedge depend on the maximum tilt angle α, and are expressed as [57, 68]

$$e = \sqrt{\frac{\alpha + \sin\alpha\cos\alpha}{\alpha - \sin\alpha\cos\alpha}}. \tag{3.35}$$

Figure 3.12 shows a volume containing α-Al(Fe,Mn)Si dispersoids, reconstructed using the WBP algorithm. The figure shows slices through the reconstructed volume. The white feature in the encircled areas represent the same dispersoid in the volume. In a) the slice in the xy plane is shown, where the y-axis corresponds to the tilt axis. The resolution along this direction is better than in the x and z directions. In b) the reconstructed volume is tilted to another viewing direction, such that slices of the volume in the yz and xz planes are also shown. In the direction of the optical axis, corresponding to the z-axis in Figure 3.12, the reconstruction is more blurred, an elongation along this direction is also observable.

Visualisation

Different approaches are used for 3D visualisation, depending on the dataset. Voxel projection, surface rendering and segmentation are among the methods commonly used. The voxel projection is good for visualising complex internal structures of materials, and was therefore not relevant in this study. Surface rendering produces a polygonal surface. Most commonly, an isosurface is generated. A single threshold intensity is used to produce a polygon following the intensity. This is less computer demanding as only the surface of the dataset is produced. Often the intensity at the boundaries of the object is not uniform, and the chosen intensity threshold may not be the correct to visualise the true morphology of the surface. A manual adjustment of the threshold levels may be appropriate [57, 70].

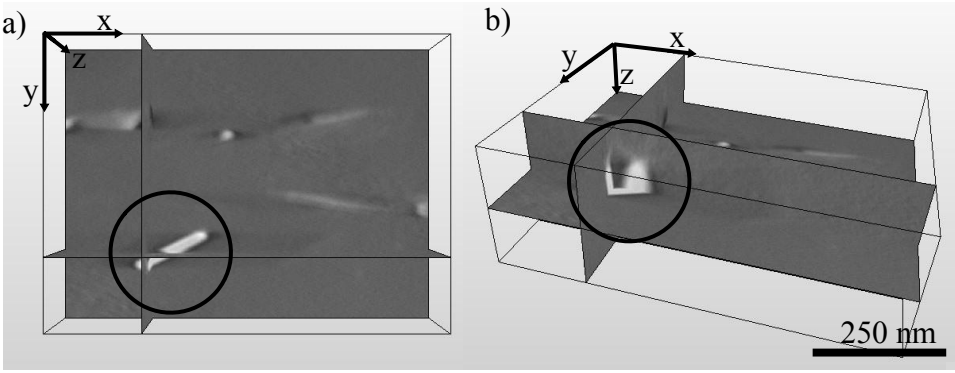

Figure 3.12: Slices of the WBP reconstruction volume of α-Al(Fe,Mn)Si dispersoids studied in Paper IV [56]. a) WBP reconstruction in the xy plane. The resolution in the direction of the tilt axis, in this case the y-axis is good. b) The same slices of the WBP volume as in a), along the optical axis, in this case the z axis, the reconstruction is blurred and elongated.

In the segmentation method, the goal is to separate the region containing the object of interest from the surroundings. The boundary between the inner and outer structure (e.g. dispersoid and Al matrix) is drawn for each segment, either automatically, semi-automatically or manually. One of the simplest automatic segmentation methods uses threshold of intensity to detect the object boundaries. Once the segmentation is performed through the whole object, it can be visualised [57].

In Paper IV [56], manual segmentation was combined with semi-automatic segmentation. A polygonal surface was created on the basis from the manual segmentation. Figure 3.13 shows the visualisation of the α-Al(Fe,Mn)Si dispersoids from the WBP reconstruction shown in Figure 3.12 [56]. The encircled dispersoid in Figure 3.12 corresponds to the encircled dispersoid in Figure 3.13.

Software packages

Various software programs are available for the data acquisition and further processing. In this work, Gatan Digital Micrograph with the tomography plug-in was used for acquisition. It also has the possibility to do reconstruction [76]. ImageJ is a freeware used for alignment and reconstruction [71, 77, 78]. Avizo is a licensed software and was used for visualisation of the reconstructions in this work [79].

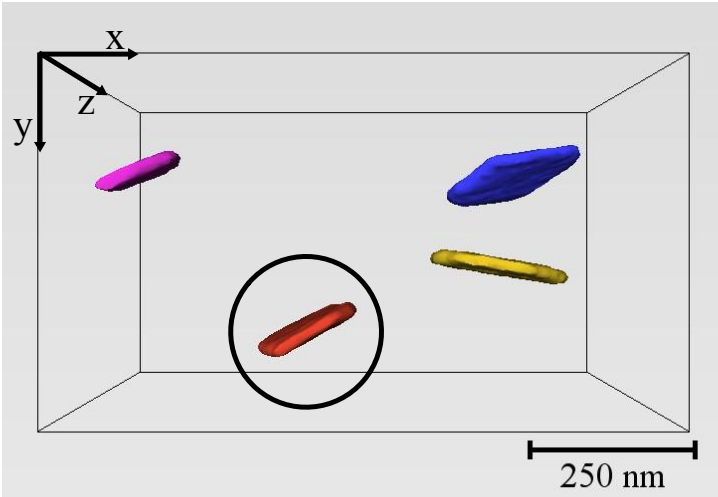

Figure 3.13: Visualisation of the WBP reconstruction of the α-Al(Fe,Mn)Si dispersoids in Figure 3.12.

3.2.6 Energy dispersive X-ray spectroscopy

Energy dispersive X-ray spectroscopy (EDX) collects the characteristic X-ray photons emitted due to inelastic scattering of electrons. The high energy electron beam interacts with the core electron of an atom in the sample and the core electron may then be ejected above the Fermi level to an unfilled state, leaving the atom in an ionized state. An electron from an outer orbital will fill the inner core orbital and a characteristic X-ray photon can be emitted. The energy of this photon equals the difference in binding energy between the two electron orbitals. This energy difference is characteristic for the specific element in the sample which the X-ray was emitted from. The electron beam may also interact inelastically with the atomic nucleus and X-rays of a continuous energy range up to the beam energy may be emitted. This X-ray signal is known as *bremsstrahlung*. An EDX spectrum consists of the characteristic X-rays and the bremsstrahlung [51]. Usually the EDX detector is side mounted on the TEM column just above the specimen, between the upper and lower objective pole piece.

The EDX spectrum is used to identify the elements present in the sample. The relative concentration of different elements can be estimated from the relative peak intensities. A high enough count rate of X-rays is essential to give sufficient intensity to the characteristic peaks. Therefore the sample should not be too thin and the intensity of the incident probe should

be sufficiently high. As a consequence of the high count rate, the spatial resolution is not too high in EDX measurements. EDX is most efficient for detection of heavy elements. X-rays from light elements are few and may be absorbed within the thick sample. Also low efficiency of the detector, high background and low energy resolution may hinder the detection of light elements [51].

EDX measurements were performed in Paper II for compositional analysis of constituent and dispersoid phases.

3.2.7 Electron energy loss spectroscopy

Electron energy loss spectroscopy (EELS) detects the inelastically scattered electrons which have gone through the specimen. EELS gives information about chemical composition and the electronic structure of the atoms in the sample [80]. From the EELS signal bonding, nearest neighbour atomic structure, dielectric response, the free electron density, the band gap and the specimen thickness can be obtained. The electrons are deflected 90° by a magnetic field onto a detector. The Lorentz force causes the electrons to be more deflected the larger the energy loss, and the electrons will hit the detector at different spatial positions according to their energy loss.

The spectrum is divided into a low loss and high loss region, below and above ∼50 eV. The low loss part of the spectrum contains the large peak from the elastically forward scattered electrons and the plasmon peak resulting from collective oscillations of the conduction electrons. The low loss region also contains the electrons which have interacted with the weakly bound outer shell electrons in the valence and conduction band. These electrons control electronic properties of the specimen. The high loss part of the spectrum contains information from the interaction of the beam electrons with the core electrons. This part of the spectra contains elemental information and in addition information about bonding and atomic positions [51].

In this work, EELS was applied for thickness measurements in Paper I [20]. The thickness is important for calculation of micro structural parameters such as number density of dispersoids. The TEM specimen thickness t can be found from the formula

$$t = \lambda \ln \frac{I_t}{I_0}, \tag{3.36}$$

where I_0 is the zero loss peak intensity, I_t is the total intensity in the low loss region up to 50 eV and λ is the mean free path of the electrons. The

mean free path in Al at 150 keV is 111 nm [81].

The interpretation of EELS spectra is more complex than the straight forward EDX analysis, as the EDX spectrum contains only elemental information. EELS requires thin specimens, and has a better spatial resolution than EDX. EELS is efficient for detecting also light elements. Therefore it can be argued that EELS and EDX are complementary techniques.

3.2.8 TEM sample preparation

In order to obtain good TEM images, it is essential to prepare good samples. The sample materials were provided from Hydro aluminium, Sunndalsøra with different alloy compositions. Samples were taken from the half radius locations of the ingots and cut into 2×2×1 cm pieces. Various low temperature homogenisation treatments were performed, as described in Chapter 2.3.3. After annealing, 2-3 mm slices of the material were cut out and mechanically polished down to 50-100 µm thin foils. From these foils 3mm discs were cut out.

A Struers TenuPol-5 electron polishing machine was used for sample polishing [82]. An electrolyte consisting of 1/3 nitric acid and 2/3 methanol was cooled down by liquid nitrogen, and electro polishing performed at -25°. The voltage and current through the specimen influence the surface topology [83]. For the 3xxx Al alloys studied in this thesis, the optimal voltage was around ∼20 V, with a current through the specimen of ∼50-150 mA. The resulting samples contained several holes of different size and characteristics. The edges around these holes may be thin enough to be electron transparent, and thus used for the TEM analysis.

Instruments

A Jeol 2010F FEG TEM operating at 200 kV and a Philips CM30 TEM operating at 150 kV were used in this thesis. An EDX detector from Oxford Instruments was used for the composition measurements in Paper II. The Jeol 2010F was used for HAADF STEM tomography in Paper IV. The microscope was equipped with STEM BF and ADF detectors. Diffraction work, statistics and BF TEM were mainly performed at the Philips CM30. Thickness measurements in Paper I were done on CM30 with a parallel electron energy loss spectrometer (PEELS) from Gatan, model 601.

Chapter 4

Other experimental techniques

4.1 Scanning electron microscopy

The scanning electron microscope (SEM) has a similar working principle as the STEM. An electron beam is focused by electromagnetic lenses and scanned over a sample in a raster at the specimen surface. In a SEM the signals from the secondary electrons (SE), backscattered electrons (BSE), Auger electrons, X-rays and cathodoluminescence can be used (see Figure 3.1). In conventional SEMs the sample is often a bulk sample, and the BSE and SE signals are the ones used for image formation. Figure 4.1 illustrates the interaction volume for the SE, BSE and X-rays in the SEM. The penetration depth increases with increasing incident primary electron energy and decreases with atomic number Z [80, 84].

The primary electron beam will scatter inelastically on the atomic electrons in the sample, and the secondary electrons escaping the sample are detected as the SE signal. The SE have low energy and interact with other atomic electrons. The average distance travelled is therefore very short and most of the SE electrons do not escape the sample. The SE escaping the surface are generated within a very small depth from the sample surface of only a few nm, and from an area a bit larger than the electron beam, as illustrated in Figure 4.1. As a consequence the SE signal is very surface sensitive with a large depth of field, resulting in a good so-called topographical contrast. The SE are detected by a scintillator photomultiplier system. Due to the low

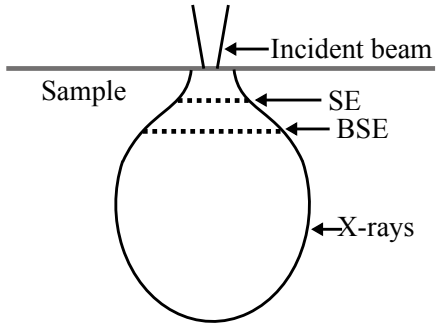

Figure 4.1: Illustration of the interaction volume from the surface of the SEM specimen for the SE, BSE and X-rays. The figure is adapted from [80].

energy of the SE they are accelerated by an applied bias voltage towards the scintillator which emits light to the photomultiplier tube [84]. Figure 4.2 a) shows an SE image of an α-Al(Fe,Mn)Si constituent particle extracted from the Al matrix. As can be seen, the morphology of the particle is branched, and the SE image shows a good topological contrast [80, 84].

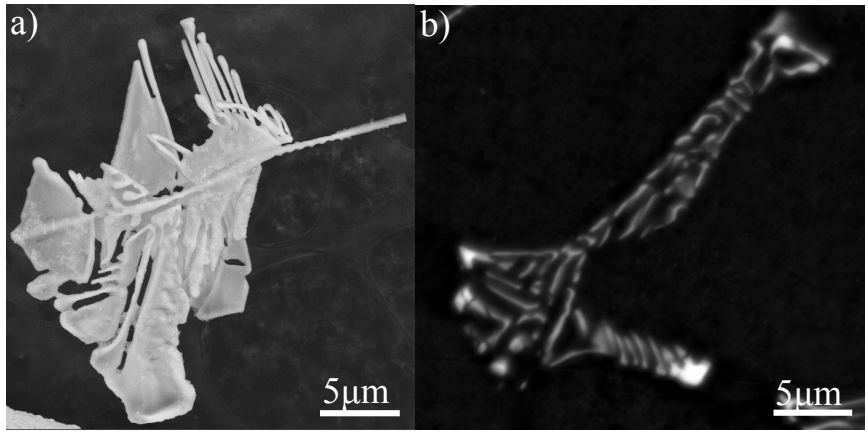

Figure 4.2: a) SE micrograph of branched constituent α-Al(Fe,Mn)Si phase extracted from the Al matrix. b) BSE micrograph of constituent α-Al(Fe,Mn)Si phase embedded in Al matrix.

The other commonly used signal in the SEM is the BSE signal, which is dominated by the primary incident electrons which have been scattered elastically through a broad annular range. The elastically scattered electrons have almost the same energy as the incident primarily electrons as they have only gone through a small energy exchange with the sample. The

BSE signal is collected by an annular scintillator detector with a large solid angle. The cross section for high angle elastic scattering is proportional to the atomic number squared, Z^2. Therefore the BSE image shows a good atomic number contrast, analogous to the HAADF STEM image. Electrons detected in the BSE detector may have been scattered from depths equal half the penetration depth of the incident primary electrons, which could be in the range of ∼100 nm, depending on the atomic number of the material. As a consequence the depth of field is much smaller [80, 84]. Figure 4.2 b) shows a BSE micrograph of an α-Al(Fe,Mn)Si constituent particle embedded in the Al matrix with an 'open crocodile jaw' appearance.

The characteristic X-rays are also a commonly detected signal in the SEM, and the instrument configuration is similar to the EDX setup described in Section 3.2.6.

In Paper II, SEM was used to study constituent phases. A Zeiss Supra SEM with a SE detector was used for morphology studies, while a Hitachi SU-6600 with a BSE detector was used for Z contrast imaging.

4.2 Mechanical testing and conductivity measurements

As described in Chapter 2.2, the mechanical strength is a very important material property for the aluminium alloys. The strength of the Al alloys can be measured in various ways. Often strength measurements are a first step before further studies are performed, as the measurements answer which conditions would be interesting for further studies. In Paper I, tensile testing and Vickers hardness measurements were performed, in addition to conductivity measurements.

Tensile testing

Tensile testing is a standard method to test the material strength. A typical tensile specimen rod geometry is shown in Figure 4.3 a). The specimen rod is stretched by an increasing force, and the tensile stress (force/area) is measured in correspondence to the strain (relative elongation) of the material. A result of the tensile testing provides an engineering stress-strain curve, as shown in Figure 4.3 b). The characteristic tensile strength and

yield strength, explained in Chapter 2.2, are found from the engineering stress-strain curve.

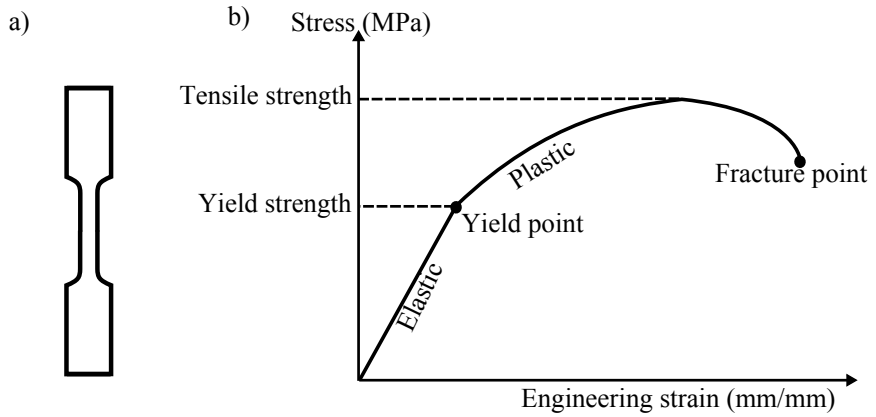

Figure 4.3: a) Typical tensile specimen geometry. b) Engineering stress strain curve, with specific characteristic points indicated.

Vickers hardness measurements

Vickers hardness (HV) is a measure of the materials ability to oppose plastic deformation [85, 86]. HV measurement is an alternative method to tensile testing by measuring the hardness. The yield strength commonly scales with the HV measurements. It is quick and easy to perform, and no special sample geometry is needed, except that the sample need to be flat and relatively smooth. However, it provides less information than a complete stress-strain curve.

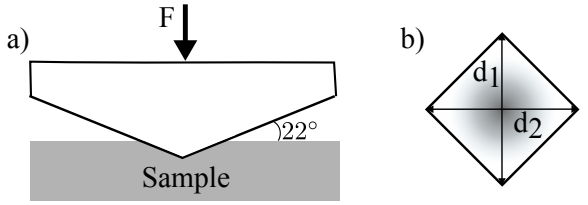

Figure 4.4: a) Schematic drawing of the diamond tip of the HV machine. b) An applied force F results in an indentation.

The measurements are performed by pushing a square based diamond pyramid tip down to the sample surface with a known force F, and measure

the average length $\bar{d}$ of the indentation diagonals d_1 and d_2 (which have the same length for sufficiently homogenised materials). Figure 4.4 shows a schematic drawing of the diamond tip a) and the resulting indentation b). The angle of the diamond is 22° to the horizontal plane. The HV is the ratio of F/A, where A is the area of the indentation. HV is given by the formula [85, 86]

$$\mathrm{HV} = \frac{2F\cos(22^\circ)}{\bar{d}^2}. \tag{4.1}$$

A Matsuzawa DVK-1S machine was used for the hardness measurements in Paper I.

Conductivity measurements

Electrical conductivity measurements give insight in the solid solution levels in the Al alloys. Electrical conductivity of Al alloys can be measured by a so called Eddy current instrument. The Eddy currents are induced by a time varying magnetic field and are measured by a probe (electromagnet) [87]. The relationship between electrical conductivity (EC) and the concentrations of alloying elements in solid solution [88, 89] was used to calculate the volume fraction of dispersoids in Paper I.

4.3 Butanol particle extraction

In Paper II constituent particles extracted from the Al matrix were analyzed. The particles were extracted by the Butanol method described by Simensen et al. [90, 91]. The dissolution was performed in a glass instrument, as shown in Figure 4.5 [90].

First the Al piece were cleaned in an acid solution to obtain a clean surface. Then the Al sample was dissolved in distilled 1-butanol. The butanol must be very clean to avoid oxidation. The dissolution was carried out in an Ar atmosphere with a pressure of ∼600 kPa, at 120°C. After the dissolution, the butanol and the aluminium butoxide are filtered through a Teflon filter, a H_2 gas is released in this process. The residue undissolved particles at the filter paper are the constituent and dispersoid phases, which were further analysed in Paper II [48]. Figure 4.2 a) is a SE micrograph of branched constituent α-Al(Fe,Mn)Si particle extracted from the Al matrix.

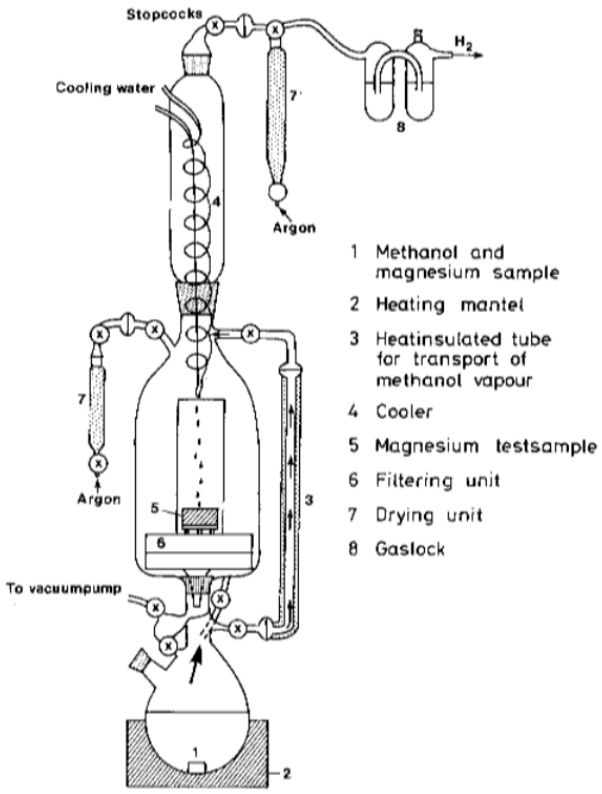

Figure 4.5: The glass instrument used to dissolve and extract the dispersoids and constituents from the Al matrix in Paper II [48]. The figure is taken from Simensen et al. [90].

Chapter 5

Conclusions and outlook

This thesis have resulted in four journal papers representing the scientific contributions of this work. They are all studies of 3xxx Al alloys after low temperature homogenisation. The main focus has been on the α-Al(Fe,Mn)Si dispersoid phase. These dispersoids have been studied with several techniques and in different perspectives. In the following the main findings and conclusions from the work, based on the four papers are presented. Furthermore, an outlook for new studies that can broaden the understanding of this topic is discussed.

5.1 Conclusions

In Paper I the influence of Mn and Si contents on the precipitation behaviour of α-Al(Fe,Mn)Si dispersoids during low temperature annealing was quantitatively studied. Strength measurements in the form of HV measurements and tensile testing were performed. Number density, size and morphology distributions and volume fraction statistics were calculated from TEM analysis. Volume fractions of dispersoids were also estimated from measurements of the electrical conductivity. A significant dispersion hardening effect was achieved by low temperature annealing. The combination of annealing temperature, annealing time and alloy composition strongly influenced the dispersion hardening effect. The most pronounced dispersion hardening was achieved in the alloy with the highest Mn and Si contents. An increased content of Si and Mn enhanced the precipitation of dispersoids, and the volume fraction of dispersoids increased. Both the yield strength and ten-

sile strength were significantly improved after 12 hours annealing at 375 °C, or as heated to 450 °C. For longer annealing times the strength decreased due to particle coarsening and consequently a reduced number density of dispersoids. The dispersion hardening effect was explained by the Orowan bowing mechanism.

The α-Al(Fe,Mn)Si dispersoids follow the commonly observed OR $\langle 1\bar{1}1\rangle_{\mathrm{Al}}$ // $\langle 1\bar{1}1\rangle_{\alpha}$, $\{011\}_{\mathrm{Al}}$ // $\{5\bar{2}\bar{7}\}_{\alpha}$. In Paper III, this OR is confirmed by diffraction studies of numerous dispersoids. The α-Al(Fe,Mn)Si dispersoids are simple cubic icosahedral quasi crystal approximant phases. They consist of a three layered Mackay icosahedron structure. The commonly observed OR of the α-Al(Fe,Mn)Si dispersoids were explained by assuming that the Mackay icosahedron composing the α-Al(Fe,Mn)Si phase had a fixed orientation, similar to that of the icosahedral quasi-crystal existing in Al. As a consequence of this assumption, only two generically different orientations of the α-Al(Fe,Mn)Si dispersoids and Al matrix are likely. Some ORs were observed in Paper III, which were deviating from the commonly observed OR. These could be related to mirror variants relative to the icosahedral 3-fold or 5-fold axes of the hypothetical Mackay icosahedron fixed in the Al matrix.

The Fe and Mn contents in the α-Al(Fe,Mn)Si dispersoids were measured by EDX. In Paper II it was shown that the edges of a α-Al(Fe,Mn)Si dispersoid contain more Fe than the central part. The α-Al(Fe,Mn)Si dispersoids probably precipitated without Fe, i.e. as α-AlMnSi. Fe diffused into the dispersoids afterwards during growth and annealing.

A methodology for a combined study of HAADF STEM tomography and diffraction of α-Al(Fe,Mn)Si dispersoids was developed in Paper IV. This methodology leads to a coupling of the 3D morphology and OR between α-Al(Fe,Mn)Si dispersoids and the Al matrix. Tomography series acquisitions and diffraction studies of the same dispersoids were performed, while keeping track of tilting directions. The study also provided information about trace directions and possible facet normals for the side edges of the dispersoids. Dispersoids in an alloy with high Si and Mn contents were studied after homogenisation for 24 hours at 450 °C. Most dispersoids were found to follow the commonly observed OR, as found in Paper III.

In Paper II the constituent phases which have precipitated at grain boundaries during solidification, were studied. The alloys were annealed for 24 hours at 450 °C. Two alloys were studied, one with high and one with low Si content. The constituent phases were studied both extracted from the Al

matrix by the butanol method and embedded in the Al matrix. X-ray analysis were performed to determine lattice parameters after particle extraction. Chemical compositions were determined by EDX. The ORs between constituents and Al matrix were studied. The constituents were located at grain boundaries, and had precipitated in connection to one of the grains during solidification. The constituents therefore show an OR to one of the Al grains at the Al grain boundary.

Al_6(Fe,Mn) constituent particles precipitated in the alloy with low Si content. Some constituents which were transformed from the Al_6(Fe,Mn) to α-Al(Fe,Mn)Si were found. The same OR as found for Al_6Mn and Al_6(Fe,Mn) dispersoids were found for the OR between the Al_6(Fe,Mn) constituents and one of the Al grains. In the alloy with high Si content, α-Al(Fe,Mn)Si constituents were found. These constituents were larger than the Al_6(Fe,Mn) constituents, and had a more complex morphology. Both types of constituents had rounded edges due to Oswald ripening. For the constituent α-Al(Fe,Mn)Si particles, various ORs were found which are different from the most common OR of α-Al(Fe,Mn)Si dispersoids in 3xxx alloys. However, the same coincident planes as often observed for the α-Al(Fe,Mn)Si dispersoids were observed.

5.2 Outlook

As can be understood from Paper III, the α-Al(Fe,Mn)Si is structurally complex. The finding that the Mackay icosahedron internal in the α-phase has a fixed orientation in relation to Al, opens up the possibility for further studies of the nucleation of these phases. Studies of the early state of these phases at the clustering stage, may reveal the atomic arrangement at the initial state. These clusters may be possible to detect by HAADF STEM studies. Nowadays EELS instrumentation opens up the possibilities to obtain more chemical information down to the atomic scale. The core loss region of the spectrum may give compositional information about the Mn/Fe ordering in these initial clusters [92, 93]

Also HAADF STEM studies of the dispersoids at a later stage may resolve some of the structural features of the phase. However, in all projected directions there is atomic overlap, making it difficult to resolve the atomic structure. The atomic bindings at the interface between the Al and dispersoids could be studied by EELS and maybe these analyses together with HR HAADF STEM could shed some more light on the α-phase. Furthermore,

the gradient of the Fe content, probably caused by the diffusion of Fe into the α-dispersoids during homogenisation treatment, as found in Paper II, could be studied more quantitatively by EELS. EDX studies of compositions may also give more insight into this phase.

Further work on the methodology of combining HAADF STEM tomography and diffraction would be interesting. More dispersoids could be imaged and reconstructed, and the methodology could also be applied to other systems. In Paper II, the WBP algorithm was used in ImageJ. No improvements were made by testing the ART and the SIRT algorithms. As the program is sort of a black box software, without too may tuning possibilities, a new implementation of these algorithms could possibly improve the reconstructions.

On the experimental side of the combined HAADF STEM tomography and diffraction study, improvements could also be made. The diffraction work and HAADF STEM tomography was performed in two different microscopes, which introduced additional challenges due to the change of sample holder. The reason for this was the one dimensional tilt range of the tomography holder. A high range double tilt axis holder would make this easier, as there would not be a need to change the holder. An in plane rotation holder with a high tilt range might also ease the process, however, the tilting to zone axis orientations of the dispersoids by applying such a holder would be tedious.

Bibliography

[1] J. A. S. Green. *Aluminum Recycling and Processing for Energy Conservation and Sustainability.* ASM International, 2007.

[2] E. Nes. The Effect of Fine Particle Dispersion on Heterogeneous Recrystallisation. *Acta Metallurgica*, 24:391 – 398, 1976.

[3] F. J. Humphreys. The Nucleation of Recrystallisation at Second Phase Particles in Deformed Aluminum. *Acta Metallurgica*, 25:1323 – 1344, 1977.

[4] G. Hausch, P. Furrer, and H. Warlimont. Recrystallisation and precipitation in Al-Mn-Si Alloys. *Zeitscrift für Metallkunde*, 69:174 – 180, 1978.

[5] H. D Merchant, J. G. Morris, and D. S. Hodgson. Characterization of Intermetallics in Aluminum Alloy 3004. *Materials Characterization*, 25:339 – 373, 1990.

[6] J. P. Suni, R. D. Doherty, P. A. Hollinshead, T. N. Rouns, and R. T. Shuey. The effect of dispersoids on recrystallisation kinetics and grain structure in hot deformed AA3004. *Aluminum Alloys*, 2:1203 – 1208, 1998.

[7] W. B. Hutchinson, A. Oscarsson, and Å. Karlsson. Control of microstructure and earing behaviour in aluminium alloy AA 3004 hot bands. *Materials Science and Technology*, 5:1118 – 1127, 1989.

[8] A. K. Vasudevan and R. D. Doherty. *Aluminum alloys-contemporary research and applications.* Academic Press San Diego, 1989.

[9] P. C. M. de Haan, J. van Rijkom, and J. A. H. Söntgerath. The Precipitation Behaviour of High purity Al-Mn Alloy. *Materials Science Forum*, 217-222:765 – 770, 1996.

[10] Y. Li and L. Arnberg. Quantitative study on the precipitation behavior of dispersoids in DC-cast AA3003 alloy during heating and homogenization. *Acta Materiala*, 51:3415 – 3428, 2003.

[11] Y. Li and L. Arnberg. Precipitation behavior in DC-cast AA3003 alloy during heat treatment, *Light Metals*. 991 – 997, 2003.

[12] V. Elser and C. H. Henley. Crystal and Quasicrystal Structures in Al-Mn-Si Alloys. *Physical Review Letters*, 55:2883 – 2886, 1985.

[13] G. Guyot and M. Audier. A quasicrystal structure model for Al-Mn. *Philosophical Magazine B*, 52:L15 – L19, 1985.

[14] A. L. Mackay. A dense non-crystallographic packing of equal spheres. *Acta Crystallographica*, 15:916 – 918, 1962.

[15] J. R. Davies. *Aluminum and Aluminum Alloys*. ASM International, 1993.

[16] W. M. Haynes, T. J. Bruno, and D. R. Lide. *CRC Handbook of Chemistry and Physics*. 95th Edition, CRC Press, Internet Version, 2015.

[17] G. Gaustad, E. Olivetti, and R. Kirchain. Improving aluminum recycling: A survey of sorting and impurity removal technologies. *Resources, Conservation and Recycling*, 58:79–87, 2012.

[18] J. D. Verhoeven. *Fundamentals of Physical Metallurgy*. John Wiley & Sons New York, 1975.

[19] Y. Li, A. M. F. Muggerud, A. Olsen, and T. Furu. Precipitation of partially coherent α-Al(Mn,Fe)Si dispersoids and their strengthening effect in AA3003 alloy. *Acta Materialia*, 60:1004 – 1014, 2012.

[20] A. M. F. Muggerud, E. A. Mørtsell, Y. Li, and R. Holmestad. Dispersoid strengthening in AA3xxx alloys with varying Mn and Si content during annealing at low temperatures. *Materials Science and Engineering A*, 567:21 – 28, 2013.

[21] P. A. Hollinshead. Effect of preheat treatment on ingot structure and recrystallisation of brass component of rolling texture in hot rolled AA 5182. *Materials Science and Technology*, 8:57 – 62, 1992.

[22] O. Engler, P. Yang, and X. W. Kong. On the formation of recrystallization textures in binary Al-1.3% Mn investigated by means of local texture analysis. *Acta Materialia*, 44:3349 – 3369, 1996.

[23] L. F. Mondolfo. *Aluminum Alloys: Structure and Properties*. Butterworth & Co London, 1976.

[24] L. Bäckerud, E. Król, J. Tamminen, and G. Chai. *Solidification Characteristics of Aluminum Alloy: Wrought Alloys*. Scanaluminum, Universitetsforlaget AS Oslo, 1986.

[25] M. Cooper and K. Robinson. The Crystal Structure of the Ternary Alloy α(AlMnSi). *Acta Crystallographica*, 20:614 – 617, 1966.

[26] K. Sugiyama, N. Kaji, and K. Hiraga. Re-Refinemenet of α-(AlMnSi). *Acta Crystallographica Section C*, C54:445 – 447, 1998.

[27] H. A. Fowler, B. Mozer, and J. Sims. Triple-shell symmetry in α-(Al,Si)-Mn. *Physical Review B*, 37:3906 – 3913, 1988.

[28] M. Cooper. The crystal structure of the ternary alloy α(AlFeSi). *Acta Crystallographica*, 23:1106 – 1107, 1967.

[29] U. Mizutani. *Hume-Rothery Rules for Structurally Complex Alloy Phases*. CRC Press New York, 2011.

[30] M. V. Jarić and D. Gratias. *Extended Icosahedral Structures*. Academic Press San Diego, 1989.

[31] D. C. Koskenmaki, H. S. Chen, and K. V. Rao. Coherent orientation relatioship between an icosahedral phase and a cubic α phase in melt-spun Al-Si-Mn. *Physical Review B*, 33:5328 – 5332, 1986.

[32] J. M. Dubois, C. Janot, and J. Pannetier. Preliminary diffraction study of icosahedral quasi-crystals using isomorphous substitution. *Physics Letters A*, 115:177 –181, 1986.

[33] J. Pannetier, J. M. Dubois, C. Janot, and A. Bilde. Thermal transformation of icoshaderal quasiperiodic crystals of the Al-Mn system. *Philosophical Magazine B*, 55:435 – 457, 1987.

[34] E. A. Stern and Y. Ma. Evidence for the microcrystallites in the icosahedral AlMnSi. *Philosophical Magazine Letters*, 56:103 – 108, 1987.

[35] V. Hansen, J. Gjønnes, and B. Andersson. Quasicrystals as part of the precipitation sequence in an industrially cast alluminum alloy. *Journal of Material Science Letters*, 8:823 – 826, 1989.

[36] V. Hansen and J. Gjønnes. Quasicrystals in an aluminium alloy matrix and the transformation to α-AlMnSi via intermediate stages. *Philosophical Magazine A*, 73:1147 – 1158, 1996.

[37] V. Hansen and J. Gjønnes. Approximants and Intermediate Stages during Transformation from a Quasicrystalline to a Crystalline Phase in an Al-Mn-Si Alloy. *Acta Crystallographica Section A*, A52:125 – 132, 1996.

[38] A. M. F. Muggerud, Y. Li, R. Holmestad, and S. J. Andersen. Mackay icosahedron explaining orientation relationship of dispersoids in al alloys. *Submitted to Acta Crystallographica Section B*, 2014.

[39] A. D. I. Nicol. The structure of $MnAl_6$. *Acta Crystallographica*, 6:285 – 292, 1953.

[40] L. K. Walford. The Structure of the Intermetallic Phase $FeAl_6$. *Acta Crystallographica*, 18:287 – 291, 1965.

[41] P. Furrer. Gefügenäderungen bei der Wärmebehandlung von Al-Mn-Stranggußbarren. *Zeitschrift für Materialkunde*, 70:699 – 706, 1979.

[42] E. Trømborg, A. L. Dons, and L. Arnberg. Investigation of the Al_6(Fe, Mn) to α–Al(Fe,Mn)Si phase transformation during homogenisation of AA3003 and AA3004 aluminum alloys, *ICAA3 Trondheim*, 270, 1992.

[43] D. T. L. Alexander and A. L. Greer. Solid-state intermetallic phase tranformations in 3XXX aluminium alloys. *Acta Materialia*, 50:2571 – 2583, 2002.

[44] D. T. L. Alexander, R. G. Hamerton, H. Cama, and A. L. Greer. Investigating the Alpha Transformation - a Solid-State Phase Change of Dispersed Intermetallic Particles from an Al_6(Fe, Mn) Phase to an α–Al–(Fe, Mn)–Si Phase, *Light Metals*. 771 – 776, 2002.

[45] Y. Li, A. Olsen, A. Johansen, and L. Arnberg. TEM study of eutectoid phase transformation of intermetallic particles from Al_6(Fe,Mn) to α-Al(Mn,Fe)Si phase in AA3003 alloy, *TMS Letters*, 991 – 997, 2005.

[46] Y. Li and L. Arnberg. Evolution of eutectic intermetallic particles in DC-cast AA3003 alloy during heating and homogenization. *Materials Science and Engineering A*, 347:130 – 135, 2003.

[47] H. Watanabe, K. Ohori, and Y. Takeuchi. Phase change in 3004 base alloys at elevated temperatures. *Aluminium*, 60:e310 – e313, 1984.

[48] A. M. F. Muggerud, Y. Li, and R. Holmestad. Composition and orientation relationships of constituent particles in 3xxx aluminum alloys. *Philosophical Magazine*, 94:556 – 568, 2014.

[49] P. Donnadieu, G. Lapasset, and T. H. Sanders. Manganese-induced ordering in the α-(Al-Mn-Fe-Si) approximant phase. *Philosophical Magazine Letters*, 70:319 – 326, 1994.

[50] M. Knoll and E. Ruska. Das Elektronenmikroskope. *Zeitschrift für Physik*, 78:318 – 339, 1932.

[51] D. B. Williams and C. B. Carter. *Transmission Electron Microscopy.* Springer New York, 2009.

[52] M. De Graef. *Introcuction to conventional transmission electron microscopy.* Cambridge University Press, 2003.

[53] C. J. Humphreys. The scattering of fast electrons by crystals. *Report on Progress in Physics*, 42:1825 – 1887, 1979.

[54] P. C. Hemmer. *Faste stoffers fysikk.* Tapir Forlag Trondheim, 1987.

[55] E. M. James and N. D. Browning. Practical aspects of atomic resolution imaging and analysis in STEM. *Ultramicroscopy*, 78:125 – 139, 1999.

[56] A. M. F. Muggerud, J. C. Walmsley, R. Holmestad, and Y. Li. Combining HAADF STEM tomography and electron diffraction for studies of α-Al(Fe,Mn)Si dispersoids in 3xxx aluminium alloys. *Submitted to Philosophical Magazine*, 2014.

[57] S. J. Pennycook and P. D. Nellist. *Scanning Transmission Electron Microscopy.* Springer New York, 2011.

[58] S. J. Pennycook. Structure determination through Z-contrast microscopy. *Advances in Imaging and Electon Physics*, 123:173 – 206, 2002.

[59] P. D. Nellist and S. J. Pennycook. The Principles of Interpretation of Annular Dark-field Z-Contrast Imaging. *Advances in Imaging and Electron Physics*, 113:147 – 203, 2000.

[60] J. Radon. Über die Bestimmung von Funktionen durch ihre Integralwerte längs gewisser Mannigfaltigkeiten. *Berichte über die Verhandlungen der Königlich Sächsischen Gesellschaft der Wissenschaften zu Leipzig, Mathematisch-Physische Klasse*, 69:262 – 277, 1917.

[61] A. M. Cormack. Representation of a Function by Its Line Integrals, with Some Radiological Applications. *Journal of Applied Physics*, 34:2722 – 2727, 1963.

[62] G. N. Hounsfield. A method and apparatus for examination of a body by radiation such as X or gamma radiation. The Patent Office London England, 1972.

[63] D. J. De Rosier and A. Klug. Reconstruction of Three Dimensional Structures from Electron Micrographs. *Nature*, 217:130 – 134, 1968.

[64] W. Hoppe, R. Langer, G. Knesch, and C. Poppe. Protein-Kristallstrukturanalyse mit Electronstrahlen. *Naturwissenschaften*, 55:333 – 336, 1968.

[65] R. G. Hart. Electron microscopy of unstained biological material: The polytropic montage. *Nature*, 159:1464 – 1467, 1968.

[66] P. A. Midgley and R. E. Dunin-Borkowski. Electron tomography and holography in materials science. *Nature Materials*, 8:271 – 280, 2009.

[67] J. Frank. *Electron Tomography: Three-Dimensional Imaging with the Transmission Electron Microscope.* Plenum Press New York, 1992.

[68] P. A. Midgley and M. Weyland. 3D electron microscopy in the physical sciences: The development of Z-contrast and EFTEM tomography. *Ultramicroscopy*, 96:413 – 431, 2003.

[69] M. Weyland. *Two and Three Dimensional Nanoscale Analysis: New Techniques and Applications.* PhD thesis, University of Cambridge England, December 2001.

[70] R. Deheghan-Niri. *Advanced Transmission Electron Microscopy Studies of Cobalt Fischer-Tropsch Catalysts.* PhD thesis, Norwegian University of Science and Technology Norway, August 2012.

[71] C. O. Sorzano, C. Messaoudi, M. Eibauer, J. R. Bilbao-Castro, R. Hegerl, S. Nickell, S. Marco, and J. M. Carazo. Marker-free image registration of electron tomography tilt-series. *BMC Bioinformatics*, 124, 2009.

[72] S. R. Deans. *The Radon Transform and Some of Its Applications.* Wiley New York, 1983.

[73] N. Yao and Z. L. Wang. *Handbook of microscopy for nanotechnology.* Kluwer Academic Publishers New York, 2005.

[74] P. A. Midgley, M. Weyland, T. J. V Yates, I. Arslan, R. E. Dunin-Borkowski, and J. M. Thomas. Nanoscale scanning transmission electron tomography. *Journal of Microscopy*, 223:185 – 190, 2006.

[75] R. A. Crowther, D. J. DeRosier, and A. Klug. The Reconstruction of a Three-Dimensional Structure from Projections and its Application to Electron Microscopy. *Proceedings of the Royal Society London*, 317:319 – 340, 1970.

[76] Gatan, Software products, *http://www.gatan.com/software/.* Accessed: 2014-05-23.

[77] M. D Abràmoff, P. J. Magalhães, and S. J. Ram. Image Processing with ImageJ. *Biophotonics International*, 11:36 – 42, 2004.

[78] C. Messaoudii, T. Boudier, CO. Sorzano, and S. Marco. Tomoj: tomography software for three- dimensional reconstruction in transmission electron microscopy. *BMC Bioinformatics*, 288, 2007.

[79] FEI Avizo® Standard, *http://www.vsg3d.com/avizo/standard.* Accessed: 2014-05-23.

[80] R. F. Egerton. *Physical Principles of Electron Microscopy.* Springer New York, 2005.

[81] T. Malis, S. C. Cheng, and R. F. Egerton. EELS log-ratio technique for specimen-thickness measurement in the TEM. *Journal of Electron Microscopy Technique*, 8:193 – 200, 1988.

[82] TenuPol-5, *http://www.struers.com/resources/elements/12/231351/TenuPol-5_English.pdf.* Accessed: 2014-05-24.

[83] S. Van Gils, S. Holten, E. Stijns, M. Vancaldenhoven, H. Terryn, and L. Mattsson. Electropolishing of aluminium: processing and assessment of visual appearance. *Surface and Interface Analysis*, 35:121–127, 2003.

[84] P. J. Goodhew, J. Humphreys, and R. Beanland. *Electron Microscopy and Analysis.* Taylor and Francis London, 2001.

[85] R. L. Smith and G. E. Sandland. An accurate method of determining the hardness of metals with particular reference to those of a high degree of hardness. *Proceedings of the Institution of Mechanical Engineers*, 1:623 – 641, 1922.

[86] H. Chandler. *Hardness Testing*. ASM International, 1999.

[87] aluMatter: Measurement of electrical resistivity, *http://aluminium.matter.org.uk/content/html/eng/default.asp?catid=158&pagesid=2144416492*. Accessed: 2014-05-16.

[88] E. Trømborg. *Phase transformations during homogenization of commercial AlMn-Alloys*. PhD thesis, The Norwegian Insitute of Technology Norway, February 1994.

[89] D. Altenpohl. *Aluminium und Aluminiumlegierungen*. Springer-Verlag Berlin, 1965.

[90] C. J. Simensen and A. Spjelkavik. Analysis of Oxides, Carbides and Iron-Rich Particles in Magnesium. *Fresenius' Zeitschrift für Analytische Chemie*, 300:177 – 182, 1980.

[91] C. J. Simensen, P. Fartum, and A. Andersen. Analysis of Intermetallic Particles in Aluminium by Dissolution of the Sample in Butanol. *Fresenius' Zeitschrift für Analytische Chemie*, 319:286 – 292, 1984.

[92] R. Sæterli, S. M. Selbach, P. Ravindran, T. Grande, and R. Holmestad. Electronic structure of multiferroic BiFeO3 and related compounds: Electron energy loss spectroscopy and density functional study. *Physical Review B*, 82:064102, 2010.

[93] E. Eberg, A. T. J. Van Helvoort, R. Takahashi, M. Gass, B. Mendis, A. Bleloch, R. Holmestad, and T. Tybell. Electron energy loss spectroscopy investigation of Pb and Ti hybridization with O at the PbTiO3/SrTiO3 interface. *Journal of Applied Physics*, 109:034104, 2011.

Part II

Papers

Paper I

Dispersoid strengthening in AA3xxx alloys with varying Mn and Si content during annealing at low temperatures.

Materials Science & Engineering A 567 (2013) 21 — 28

Materials Science & Engineering A 567 (2013) 21–28

Contents lists available at SciVerse ScienceDirect

Materials Science & Engineering A

journal homepage: www.elsevier.com/locate/msea

Dispersoid strengthening in AA3xxx alloys with varying Mn and Si content during annealing at low temperatures

Astrid Marie F. Muggerud [a,*], Eva Anne Mørtsell [a], Yanjun Li [b], Randi Holmestad [a]

[a] Department of Physics, University of Science and Technology, NTNU, N-7491 Trondheim, Norway
[b] SINTEF Materials and Chemistry, N-7465 Trondheim, Norway

ARTICLE INFO

Article history:
Received 22 November 2012
Received in revised form
4 January 2013
Accepted 5 January 2013
Available online 11 January 2013

Keywords:
Electron microscopy
Mechanical properties
Aluminium alloys
Dispersoids
Dispersion hardening

ABSTRACT

The precipitation behaviour of dispersoids in Direct Chill (DC)- cast 3xxx alloys with varying compositions of manganese and silicon has been studied during isothermal annealing at low temperatures. The evolution of density, size and volume fraction of the dispersoids has been quantitatively studied by Transmission Electron Microscopy (TEM) and electrical conductivity measurements. Moreover the influence of precipitation of dispersoids on hardness and tensile strength of the alloys is systematically investigated. A clear dispersion hardening effect from dispersoids is revealed and the hardening effect increases with increasing Mn and Si contents in the alloys. The hardening effect from dispersoids is discussed in light of the Orowan mechanism.

1. Introduction

Wrought 3xxx aluminium alloys are widely used in architecture and packaging industry. In contrast to heat treatable alloys which gain their strength through heat treatment, the 3xxx alloys mainly get their strength from work hardening and are therefore called non-heat treatable alloys [1–3]. One of the main alloying elements in 3xxx alloys is manganese [4]. Additions of Mn influence the material properties in various ways. The size and amount of intermetallic Mn-containing particles affect the grain structure development during thermomechanical processing by stimulating or retarding recrystallisation. Strengthening of the material by solid solution hardening is another way Mn influences material properties [5]. In the as-cast material, the aluminium matrix is supersaturated with Mn and Si [3]. A homogenisation before further mechanical processing is essential to eliminate micro segregation, reduce solid solution level of Mn and get the right size and density of constituent particles and fine dispersoids.

The type of dispersoids varies with composition and heat treatment. At low temperatures, two metastable phases form in binary Al–Mn alloys, these are the body centred cubic (bcc) $Al_{12}Mn$ and the orthorhombic Al_7Mn. At higher temperatures the equilibrium phase in the Al–Mn alloy is the orthorhombic Al_6Mn phase [4,6]. Additions of iron and silicon reduce the solubility of Mn in Al matrix and speed up the precipitation of Mn-containing dispersoids. Si favours the precipitation of dispersoids of the simple cubic α-Al(Mn)Si phase [2,5,7]. Fe may substitute Mn in both Al_6Mn phase and α-AlMnSi phase. When the Mn/Fe ratio is high, α-Al(Mn, Fe)Si phase has a simple cubic crystal structure, while for higher Fe content the phase may change to a body centred cubic structure [3]. The simple cubic α-Al(Mn, Fe)Si phase is the phase of the dispersoids studied in the present work.

During homogenisation at low temperatures, and during the early stage of precipitation, a quasi crystalline icosahedra phase may precipitate in 3xxx alloys [3,8–10]. It is proposed that this phase is the starting phase for α-Al(Mn, Fe)Si dispersoids that form at higher temperatures of homogenisation.

The dispersoids have strong influence on the recrystallisation behaviour of 3xxx aluminium alloys [3,7,11–15]. However, in most previous studies they are considered to have negligible hardening effects. In a previous study [16], it has been found that a significant increase of the yield strength of a DC-cast 3003 alloy can be achieved by an annealing treatment at 375 °C for 24 h. This has been attributed to the dispersion hardening effect caused by the precipitation of a large amount of fine dispersoids.

In order to fully exploit the dispersion hardening effect, a more systematic study on the influence of alloying elements, annealing temperature and annealing time on the precipitation behaviour has been done. The effects of Si and Mn content on the precipitation of dispersoids and their influence on the mechanical properties have been investigated. The dispersion hardening effect of dispersoids has been discussed based on the Orowan mechanism.

* Corresponding author. Tel.: +47 73593435; fax: +47 73597710.
E-mail address: astrid.muggerud@ntnu.no (A.M.F. Muggerud).

0921-5093/$ - see front matter © 2013 Elsevier B.V. All rights reserved.
http://dx.doi.org/10.1016/j.msea.2013.01.004

Table 1
Content of main alloying elements in the four experimental alloys.

Alloy	Fe (wt%)	Si (wt%)	Mn (wt%)
*C*1	0.530	0.152	0.392
*C*2	0.504	0.148	0.970
*D*1	0.517	0.494	0.400
*D*2	0.497	0.480	0.992

2. Experimental

The experimental materials used in this study were produced by Hydro in Norway. Four DC-cast ingots with different chemical compositions were prepared. High and low Si content was combined with high and low Mn content in order to study the influence of the alloying elements on the precipitation behaviour. Samples were taken from the half radius locations of the ingots and cut into $2 \times 2 \times 1$ cm blocks. For annealing heat treatment an air circulating furnace was used. The alloys were heat treated from room temperature with a heating rate of 50 °C/h up to annealing temperatures of 375 °C and 450 °C. At the annealing temperatures the samples were kept for 0, 1, 2, 4, 8, 12, 16 and 24 h and then quenched into cold water.

Mass spectroscopy measurements were performed to determine the chemical compositions of the alloys. The concentrations of the major alloying elements in the four alloys studied are given in Table 1. Also trace level of Cu, Mg, Zn, Cr, Ni, Pb and Sn in amounts less than 0.01 wt% were detected.

Different measurements were performed on the alloys, including electrical conductivity measurement by Foerster Sigmatest 2.069 and Vickers hardness measurement by a Matsuzawa 0.3–20 kg hardness tester. Vickers Hardness (HV) measurements were done with 1 kg load.

The alloys after 0–24 h annealing treatment at 375 °C–450 °C were machined into rods for tensile testing with a gauge length of 30 mm and inner diameter of 6 mm. The tensile tests were performed with a MTS 810 tensile testing machine at a strain rate of 0.001 s^{-1}.

TEM foils were made by electro polishing with an electrolyte containing two parts Methanol and one part Nitric acid at −20 °C using a Struers TenuPol-5 electro polishing unit. A Philips CM30 TEM operating at 150 kV was used for microstructure statistics. The microscope was equipped with an electron energy loss spectrometer (EELS) (Gatan model 601) used for TEM sample thickness measurements.

In order to calculate the number density for each sample area, the dispersoids were manually counted on the TEM micrographs. For each specimen 10 sample areas were imaged and more than 100 dispersoids were measured for each specimen. Area fraction of precipitation free zones (PFZ) was approximated by light microscopy investigations of polished samples etched in 10% Phosphorus solution. For some of the samples annealed for 0–12 h and a field emission scanning electron microscope (FESEM) Zeiss Ultra microscope was used for PFZ analysis.

3. Results and discussion

3.1. Electrical conductivity

The relationship between electrical conductivity (EC) σ and the concentrations of alloying elements in solid solution in wt%, Fe_{SS}, Mn_{SS} and Si_{SS} can be expressed as [17,18]

$$\frac{1}{\sigma} = 0.0267 + 0.032Fe_{SS} + 0.033Mn_{SS} + 0.0068Si_{SS}. \quad (1)$$

The relative concentration change of Mn and Fe in solid solution can be calculated by using Eq. (1) provided that the change of EC is only due to the change of solid solution level of alloying elements. The contribution from Si is an order of magnitude smaller than those from Fe and Mn. By neglecting the contribution of Si concentration change on the EC, the concentration change of Fe+Mn in solid solution Δ(Fe+Mn) in wt% is given by

$$(Fe+Mn)_{SS}(wt\%) = \frac{1}{0.033}\left[\frac{1}{\sigma(T)} - \frac{1}{\sigma(0)}\right], \quad (2)$$

where $\sigma(0)$ is the electrical conductivity of the as-cast material and $\sigma(T)$ is the electrical conductivity as a function of time and temperature after annealing treatment. From Eq. (2) the volume fraction of dispersoids, V_{disp} can also be estimated under the assumption that all the solute leaving the supersaturated solid solution goes into dispersoids;

$$V_{disp} = \Delta(Fe+Mn)_{SS}(wt\%)C \quad (3)$$

The constant C in Eq. (3) is given by

$$C = \frac{Mm(Al)}{Mm(Fe/Mn)}\ (\alpha\text{-units})\ \frac{V(\alpha)}{V(Al)} \approx 2.50.$$

Mm(Al) and Mm(Fe/Mn) are the molar masses of Al and the average molar mass of Fe and Mn. α-units is the number of dispersoid units created per solute atom of Mn or Fe. V(Al) and $V(\alpha)$ are the volumes occupied by each atom in the unit cells. An α-Al(Mn, Fe)Si unit cell of the type $Al_{96}(Mn, Fe)_{24}Si_{18}$ with lattice parameter 12.68 Å were used in the calculations.

Fig. 1(a) shows the electrical conductivity evolution for the four alloys during annealing at 375 °C–450 °C. There is an overall increase in the electrical conductivity with annealing time and temperature, as more and more Mn is precipitated from the supersaturated solid solution. During annealing at both 375 °C and 450 °C the EC values are much higher for *C*1 and *D*1 compared to *C*2 and *D*2, as alloys *C*1 and *D*1 have lower initial solute content of Mn. With increasing annealing time, *D*2 shows a more pronounced increase in EC than *C*2, which indicates that a high Si content accelerates the decomposition of Mn in supersaturated solid solution. Due to the same reasons, alloy *D*1 with a combination of high Si and low Mn content has the highest electrical conductivity.

Fig. 1(b) shows the volume fraction of dispersoids calculated from Eqs. (2) and (3) based on the EC measurements. An increase in volume fractions with increasing annealing temperature from 375 °C to 450 °C is present for all four alloys. Alloys *C*2 and *D*2 have the highest Mn content in solid solution available for the precipitation of dispersoids and thus have the highest calculated volume fractions of dispersoids. The calculated volume fractions for the alloys *C*1 and *D*1 are generally lower than *C*2 and *D*2 due to the lower Mn level in these alloys. *D*1 has slightly higher volume fractions for both annealing temperatures than the *C*1 alloy because the level of Si in *D*1 is higher, leading to more decomposition of supersaturated solid solution of Mn compared to *C*1.

3.2. Dispersoids

3.2.1. Morphology of dispersoids

Fig. 2 shows the morphology evolution of dispersoids in alloy *D*2 as a function of annealing time during annealing at 375 °C. Fig. 2(a) shows dispersoids after the alloy was heated to 375 °C. As can be seen, the size of the dispersoids is very small and most of the dispersoids have precipitated in the vicinity of dislocations. Heterogeneous nucleation at dislocations can reduce the nucleation energy barrier of dispersoids [19]. After 12 h annealing at 375 °C, both the size and the number density of the dispersoids

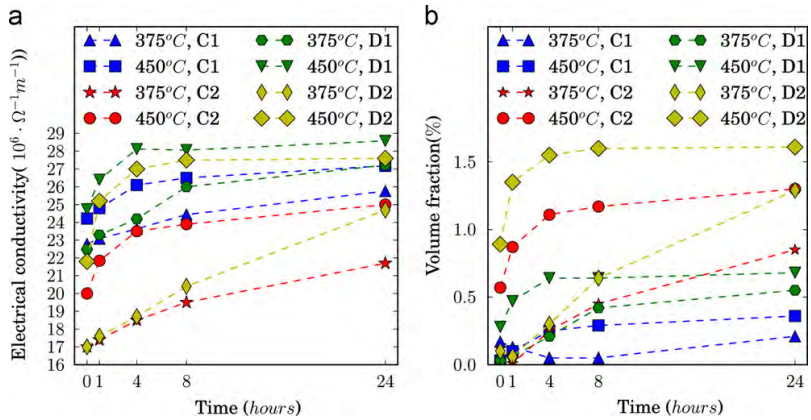

Fig. 1. (a) Electrical conductivity of alloys during annealing at 375 °C and 450 °C, and (b) Volume fraction of dispersoids calculated from electrical conductivity.

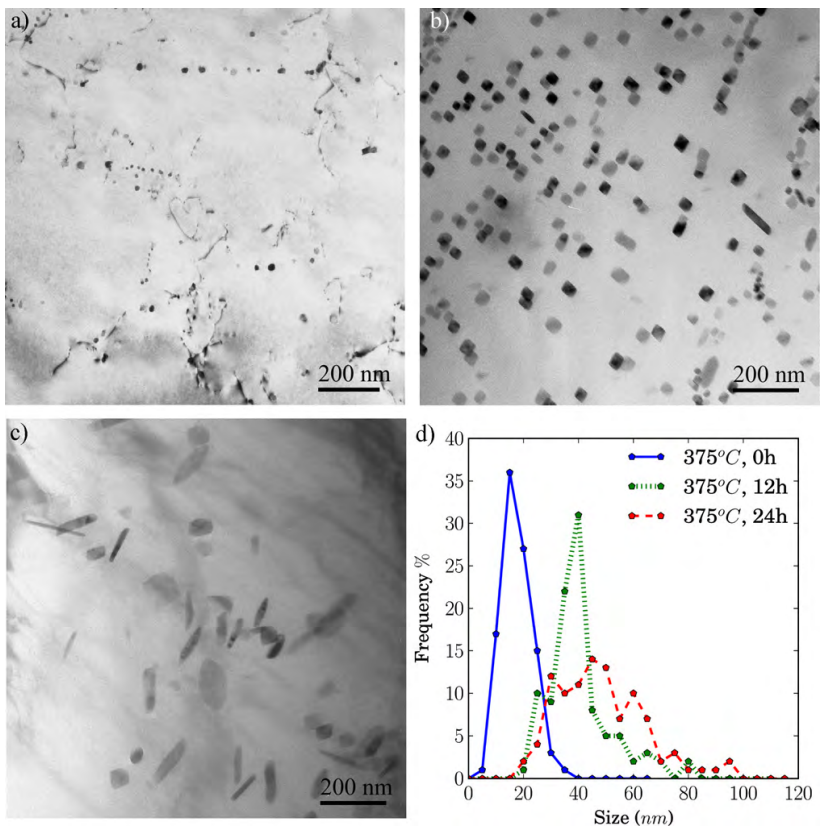

Fig. 2. Evolution of dispersoid morpholgy in alloy *D*2 during annealing at 375 °C. (a) As-heated to 375 °C, (b) 12 h annealing, (c) 24 h annealing, and (d) histogram showing the size distribution of dispersoids (equivalent diameter) after annealing at 375 °C for 0, 12 and 24 h.

have increased as shown in Fig. 2(b). The dispersoids grow in size as a consequence of continuous decomposition of solid solution supersaturated with Mn and Si in the matrix [3]. It is interesting to note that most of the dispersoids have nearly a cubic shape and seem to have the same orientation to the Al matrix.

After 24 h annealing at 375 °C shown in Fig. 2(c), the dispersoids have grown in size, but the number density of dispersoids has decreased. This is due to the coarsening of dispersoids [3].

Fig. 2(d) shows the histogram of the size distributions of dispersoids in alloy *D*2 after annealing at 375 °C for 0, 12 and

24 h. The frequency of dispersoids with larger equivalent diameters goes up as the annealing time is increased. A larger scatter in size is also present when the annealing time is increased. The shrinkage of dispersoids due to the coarsening may explain why small dispersoids are also present after long time of annealing.

3.2.2. Number density and size of dispersoids

Fig. 3(a) shows the number density of the four alloys as annealed at 375 °C and 450 °C for 0, 12 and 24 h. The Mn and Si amount in the alloys has strong influence on the number density. The high content of Si in alloy *D*1 and *D*2 leads to enhanced decomposition of the solid solution of Mn and fast precipitation of dispersoids. The number densities of dispersoids in the two alloys have reached rather high values during heating up to the target annealing temperatures. The effect of coarsening and growth is most prominent as the number density decreases with annealing time. The number densities in alloy *C*1 and *C*2 are generally lower than for *D*1 and *D*2. The lower Si content in *C*1 and *C*2 has resulted in a slower decomposition of the solid solution of Mn. In alloy *C*1 the Mn level is also low which result in low number density of dispersoids for all annealing conditions.

The evolution of the equivalent diameter of dispersoids with time for annealing at 375 °C and 450 °C is shown in Fig. 3(b). An increase of equivalent diameter with annealing time is present for all alloys. The size of dispersoids after annealing at 375 °C is generally lower than that after annealing at 450 °C. Diffusion speed of alloying elements is much slower at 375 °C than 450 °C resulting in slower growth and coarsening of dispersoids. Alloy *D*2 has the largest average equivalent diameter after the same annealing treatment, as the amount of Mn and Si available for precipitation of dispersoids is the highest among the four alloys.

3.2.3. Precipitation free zones analysis

The area fraction of PFZs has been measured by optical microscopy images taken from deeply etched samples and SEM images taken from the as-polished samples. The area fraction of the PFZ was measured from 10 images for each sample.

Fig. 4 shows the PFZs for sample *C*2 after annealing at 375 °C for 24 and 12 h. The optical micrograph of the sample as heated to 375 °C and annealed for 24 h is shown in Fig. 4a). The distribution

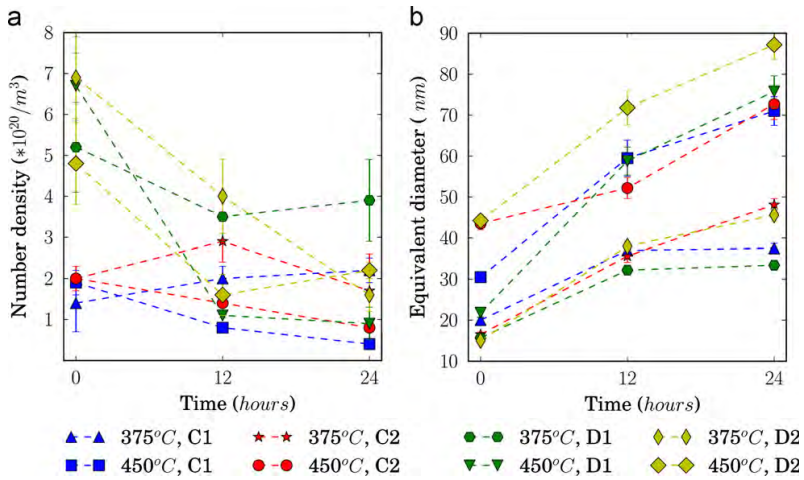

Fig. 3. (a) Number density and (b) equivalent diameter evolution of dispersoids for the four alloys after annealing at 375 °C and 450 °C for 0,12 and 24 h annealing time. The equivalent diameter increases with increasing temperature and annealing time.

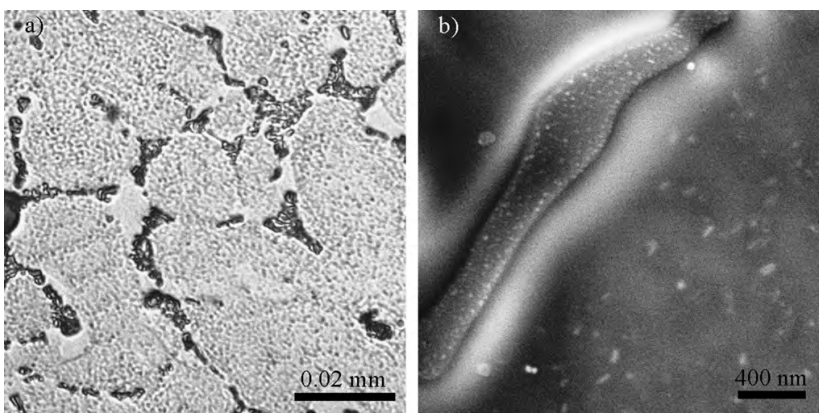

Fig. 4. Precipitation free zone evolution in sample *C*2 during annealing at 375 °C. (a) Optical micrograph for 24 h annealing treatment. The etch pits after the dispersoids in the matrix are visible, so is also the PFZs surrounding most of the constituent particles. (b) SEM micrograph after 12 h annealing. Constituent particle and surrounding Al matrix with dispersoids present close to the constituent particle.

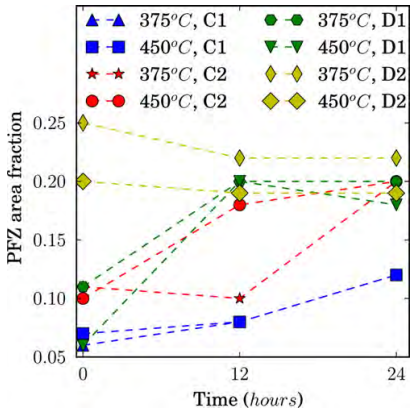

Fig. 5. PFZ evolution with time for the four alloys at annealing temperature of 375 °C and 450°C, 0 to 24 h annealing. An increase of PFZ area fraction with increasing Si and Mn amount and with annealing time can be seen for alloy *C*1, *C*2 and *D*1. For alloy *D*2 the PFZ area fractions are high for all conditions.

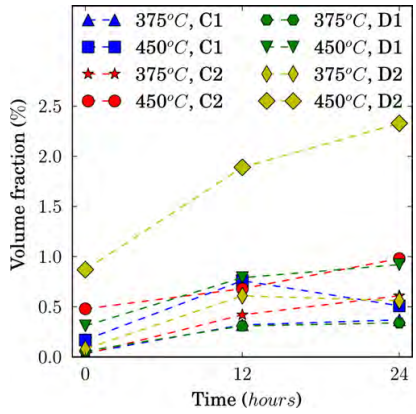

Fig. 6. Volume fraction evolution of dispersoids during annealing. The volume fraction increases with increasing annealing time and temperature. Alloy *D*2 with the highest amount of alloying elements has the highest volume fraction of dispersoids.

of dispersoids in the matrix is clearly presented by etching pits. The PFZ zones surrounding constituent particles and grain boundaries can be seen. Fig. 4(b) is a SEM micrograph after 12 h annealing time. Dispersoids were not visible in the optical micrograph, only the constituent particles could be seen. Therefore, SEM images have been taken to reveal the PFZ of those samples that could not be revealed by optical micrographs. The distance between constituent particles and dispersoids is rather small, within the range of 200–400 nm. The only contribution to the PFZ for the short annealing time samples is then the area surrounding the constituent particles and grain boundaries in addition to the area of the constituent particles themselves. Fig. 5 shows the PFZ evolution as a function of annealing time during annealing at 375 °C and 450 °C. The fraction of the PFZs increases for most cases with annealing time. The increase of PFZ is mainly due to the coarsening between fine dispersoids and coarse constituent particles. For alloy *C*1 the fraction of PFZ is small for both annealing temperatures and for all annealing times. This is because the coarsening of dispersoids is less pronounced in this alloy due to the low content of Mn and Si. Alloy *D*2, containing the highest contents of Mn and Si, has higher area fraction of PFZs for both annealing temperatures and all annealing times.

3.2.4. Volume fraction of dispersoids

In order to calculate the volume fraction of dispersoids from the TEM measurements the same procedure as described by Li and Arnberg [3] was used with some modifications. The volume fraction V_V is given by

$$V_V = \frac{K}{4}\pi\overline{D}^3 N_V. \quad (4)$$

K is the shape factor, accounting for the shape of the dispersoids, $\overline{D}$ is the average equivalent diameter of dispersoids measured from TEM images and N_V is the volumetric number density of dispersoids given by

$$N_V = N_A \frac{K\overline{D}}{t+K\overline{D}}(1-A_{PFZ}). \quad (5)$$

N_A is the area number density of dispersoids, t is the TEM foil thickness and A_{PFZ} the area fraction of PFZ.

The volume fraction evolution of dispersoids with annealing time in the four experimental alloys during annealing at 375 °C and 450 °C is shown in Fig. 6. A similar trend can be seen for all the alloys, but with some scatter in the result values of the volume fractions. The volume fraction increases with both annealing time and temperature, which is consistent with the evolution of the measured electrical conductivity. The increase in temperature makes Mn diffuse faster and more Mn goes into the dispersoids. A longer annealing time favours the decomposition of the supersaturated solid solution resulting in increased volume fraction of dispersoids.

Alloy *D*2 has the highest volume fraction of dispersoids at 450 °C as *D*2 has both high Mn and Si content. Alloy *C*2 has the same Mn content but lower Si content than *D*2. The lower Si content has resulted in a much lower volume fraction of dispersoids than in alloy *D*2 after annealing at 450 °C. For *C*1 with both low Mn and Si content the volume fraction increase with both annealing temperature and time is less pronounced. Despite the higher content of Si in alloy *D*1, the volume fraction is still low due to the low Mn content.

When comparing the volume fractions in Fig. 6 with the volume fractions calculated from the electrical conductivity measurements presented in Fig. 1(b), the same trends can be seen. The volume fraction is increasing with annealing temperature, time and with the amount of Mn and Si.

3.3. Mechanical properties

3.3.1. Vickers hardness

Fig. 7 shows the evolution of Vickers hardness of the four alloys as a function of annealing time at 375 °C and 450 °C. All the alloys show an enhanced hardness as heated to 450 °C at heating rate of 50 °C/h. The highest hardness can be achieved by heating the alloys to 450 °C or by 12 h annealing at 375 °C. For 450 °C annealing the hardness drops with annealing time for all four alloys.

It can be seen that the chemical composition has a strong influence on the hardness values of the alloys after the same annealing treatment. Alloy *C*1 in Fig. 7(a), which has low content of Mn and Si, has the lowest hardness. With a higher content of Mn, alloy *C*2 in Fig. 7(b) has markedly higher hardness than alloy *C*1. Alloy *D*1 in Fig. 7(c) with a high content of Si, also has much higher hardness than alloy *C*1. Alloy *D*2 in Fig. 7(d), with the highest Mn and Si contents among the four alloys, has the highest hardness values. Increasing the content of Si and Mn in 3xxx

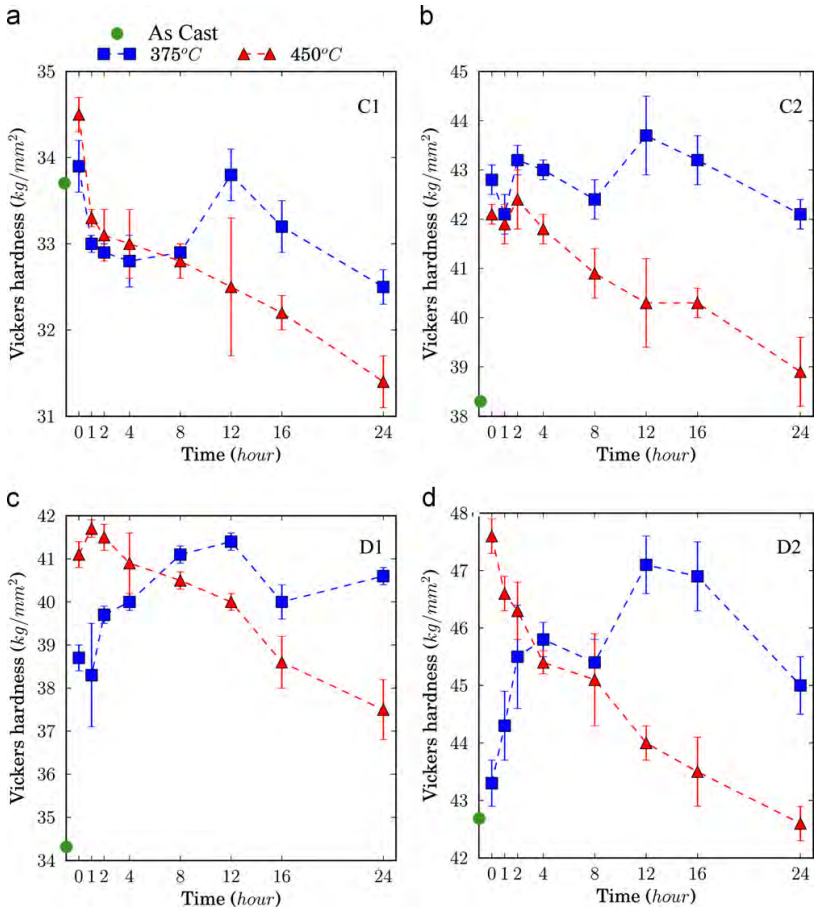

Fig. 7. Evolution of Vickers hardness of the four alloys during annealing at 375 °C and 450 °C. As-cast hardness values are also indicated. (a) Alloy *C*1, (b) Alloy *C*2, (c) Alloy *D*1, and (d) Alloy *D*2. A pronounced increase in hardness for all four alloys, as heated to 375 °C with 12 hours annealing time and as heated to 450 °C, is observed.

alloys can significantly increase the hardness of the alloys in the as-annealed state.

3.3.2. Tensile properties

The typical engineering stress–strain curves of the alloys for as-cast state and as heated to 375 °C and 450 °C and after 24 h annealing are presented in Fig. 8. For the same alloy, the yield strength has been much improved by heating to 450 °C or by annealing at 375 °C for 24 h comparing to the as-cast state. Since the solid solution level of Mn and Si in the as-annealed state is much lower than in the as-cast state, the strength improvement should be attributed to dispersion hardening. By comparing different alloys, it can be seen that the Mn and Si contents have a strong influence on both the yield strength and tensile strength of the alloys. After the same annealing treatment, the yield strength increases with increasing Mn and Si content in the alloys. Alloy *D*2 with the highest Mn and Si content, has the highest yield strength and tensile strength. The evolution of yield strength with Mn and Si contents in the alloys and the annealing treatment is consistent with the hardness evolution of the alloys.

Table 2 lists the measured yield strength values for the four alloys as-cast, as annealed at 375 °C for 24 h and as-heated to 450 °C. The contributions to yield strength from dispersoids calculated from TEM measurements are listed.

3.3.3. Strengthening mechanisms

The contribution of dispersoids to the yield strength of alloys, σ_D, due to the Orowan bowing mechanism can be calculated from the Ashby–Orowan equation [20]

$$\sigma_D = \frac{0.84MGb}{2\pi(1-\nu)^{1/2}\lambda}\ln\frac{r}{b}. \quad (6)$$

M is the Taylor factor, G the shear modulus of the Al matrix, b the Burgers vector of dislocations in Al and ν the Poison ratio. The interspacing of dispersoids λ depends on the radius r and volume fraction f of dispersoids:

$$\lambda = r\left(\frac{2\pi}{3f}\right)^{1/2}. \quad (7)$$

According to Eq. (6) and (7), the yield stress due to dispersion hardening increases with increasing volume fraction and decreasing size of dispersoids. The yield strength of the alloys as annealed at 375 °C, 24 h and heated to 450 °C are calculated and listed in Table 2. An improvement of yield stress as high as 32 MPa caused

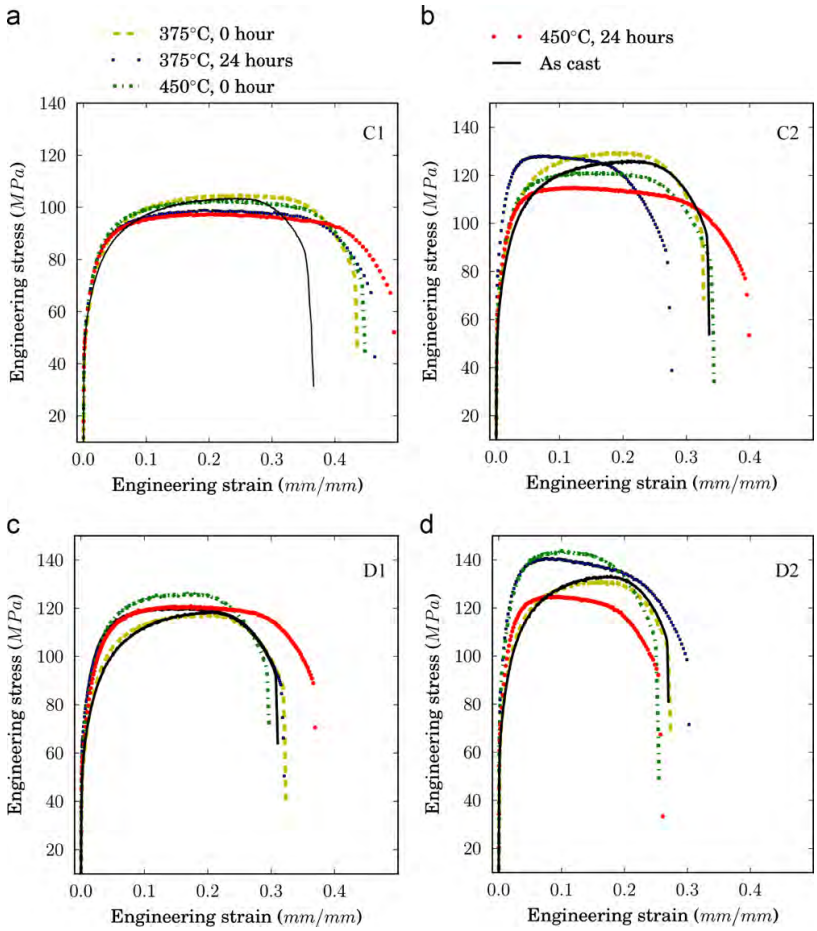

Fig. 8. Engineering stress–strain curves of the alloys as-cast, as-heated to 375 °C and 450 °C and as-annealed for 24 hours. (a) *C*1. (b) *C*2. (c) *D*1. and (d) *D*2.

Table 2
Yield strength for $\varepsilon = 0.002$ strain for as cast and as annealed at 375 °C, 24 h and 450 °C, 0 h. Difference in yield strength between as-cast state and as-annealed state and the contribution to yield strength from dispersoids calculated from TEM measurements are listed. Measured values are given in MPa.

Alloy	Heat treatment (°C, hours)	Yield strength σ_C in as cast state (MPa)	Yield Strength σ_A after annealing (MPa)	Increase in yield strength $\Delta\sigma = \sigma_A - \sigma_C$ (MPa)	Dispersoid Contribution to yield strength (MPa)
*C*1	375, 24	52.9	56.7	3.8	24.0
*C*1	450,0	52.9	56.3	3.4	19.0
*C*2	375, 24	63.5	86.6	23.1	25.5
*C*2	450,0	63.5	73.1	9.6	24.4
*D*1	375, 24	60.4	72.7	12.3	25.1
*D*1	450,0	60.4	67.6	7.2	32.9
*D*2	375, 24	72.6	91.3	18.7	25.4
*D*2	450,0	72.6	82.7	10.1	32.5

by dispersoids has been achieved in alloys *D*1 and *D*2 by heating the material to 450 °C followed by water quenching. However, the increase in the measured yield strength of the alloys by annealing treatment is much lower than the calculated yield strength increase caused by precipitation of dispersoids. This should be attributed to the reduced solute strenthening as a result of the reduction of the concentration of Mn and Si in solid solution during annealing treatment.

4. Conclusions

The influence of Mn and Si contents on the precipitation behaviour of dispersoids in AA3xxx alloys during low temperature annealing has been quantitatively studied. It is found that increasing Si and Mn contents enhance the precipitation of dispersoids. After the same annealing treatment, the density and volume fraction of dispersoids increase with increasing Si or Mn content in the alloy. Mechanical property tests show that a significant dispersion hardening effect can be achieved in 3xxx alloys by low temperature annealing with a combination of right annealing temperature and annealing time. The most pronounced dispersion hardening effect has been achieved in the alloy containing the highest Mn and Si contents. Both the yield strength and tensile strength have been much improved after 12 h annealing at 375 °C or as-heated to 450 °C with a heating rate of 50 °C/h. The dispersion hardening effect of dispersoids has been explained by the Orowan bowing mechanism.

Acknowledgements

This work has been supported by the KMB project MoReAl financed by The Research Council of Norway, and the industrially partners Hydro and Sapa Technology. Dr. J. Friis, SINTEF Materials and Chemistry, is acknowledged for writing a Python script that has been used as a basis for the PFZ analysis.

References

[1] J. Courbon, Mater. Sci. Forum 331–337 (2000) 17–30.
[2] D.T.L. Alexander, A.L. Greer, Acta Mater. 50 (2002) 2571–2583.
[3] Y.J. Li, L. Arnberg, Acta Mater. 51 (2003) 3415–3428.
[4] N.A. Belov, D.G. Eskin, A.A. Askenov, Multicomponent Phase Diagrams: Applications For Commercial Aluminum Alloys, Elsevier Ltd, Oxford, 2005.
[5] P.C.M. de Haan, J.v. Rijkom, J.A.H. Söntgerath, Mater. Sci. Forum 217–222 (1996) 765–770.
[6] D.B. Goel, U.P. Roorkee, P. Furrer, H. Warlimont, Aluminium 50 (1974) 511–516.
[7] G. Hausch, P. Furrer, H. Warlimont, Z. Materialkunde 69 (1978) 174–180.
[8] V. Hansen, J. Gjønnes, B. Andresson, J. Mater. Sci. Lett. 8 (1989) 823–826.
[9] V. Hansen, J. Gjønnes, Philos. Mag. A 73 (1996) 1147–1158.
[10] V. Hansen, J. Gjønnes, Acta Crystallogr. 52 (1996) 125–132.
[11] F.J. Humphreys, Acta Metall. 25 (1977) 1323–1344.
[12] E. Nes, Acta Metall. 24 (1976) 391–398.
[13] J.P. Suni, R.D. Doherty, P.A. Hollinshead, T.N. Rouns, R.T. Shuey, in: ICAA6, Aluminum alloy, their physical and mechanical properties, Toyohashi Japan, 1998, pp. 1203–1208.
[14] Y.J. Li, L. Arnberg, Light metals, TMS, 2003 991–997.
[15] H.D. Merchant, J.G. Morris, D.S. Hodgson, Mater. Charact. 25 (1990) 339–373.
[16] Y.J. Li, A.M.F. Muggerud, A. Olsen, T. Furu, Acta Materiala 60 (2011) 1004–1014.
[17] D.D. Altenpohl, Aluminium und Aluminiumlegierungen, 1965.
[18] E. Trømborg, in: PhD Thesis, NTH, Norway, 1994.
[19] D.A. Porter, K.E. Easterling, M.Y. Sherif, Phase Transformations in Metals and Alloys, third ed., Taylor & Francis Group, London, 2009.
[20] M.F. Ashby, in: AIME Conference Proceedings, New York Meeting Society, New York, 1966.

Paper II

Composition and orientation relationships of constituent particles in 3xxx aluminum alloys

Philosophical Magazine 94, 6 (2014) 556 – 568

Philosophical Magazine, 2014
Vol. 94, No. 6, 556–568, http://dx.doi.org/10.1080/14786435.2013.857796

Taylor & Francis
Taylor & Francis Group

Composition and orientation relationships of constituent particles in 3xxx aluminum alloys

Astrid Marie F. Muggerud[a]*, Yanjun Li[b] and Randi Holmestad[a]

[a]*Department of Physics, Norwegian University of Science and Technology, NTNU, N-7491 Trondheim, Norway;* [b]*SINTEF Materials and Chemistry, N-7465 Trondheim, Norway*

(*Received 31 July 2013; accepted 15 October 2013*)

Constituent and dispersoid phases in two Direct Chill-cast 3xxx aluminum alloys after low-temperature annealing, with different silicon content have been studied. The lattice parameters, chemical composition, morphology and orientations relationships of constituent particles with regard to Al matrix have been addressed. Al_6(Fe,Mn) is found to be the most prominent constituent phase in the alloy with a low Si content. The orientation relationship between aluminum matrix and this phase is determined as $[\bar{1}\,\bar{1}\,\bar{2}]_c//[\bar{1}\,1\,\bar{1}]_{Al}$, $(3\,3\,\bar{3})_c//(0\,\bar{2}\,\bar{2})_{Al}$, which is consistent with the orientation relationships of Al_6(Fe,Mn) dispersoids. α–Al(Fe,Mn)Si constituent particles in the Si rich alloy have been found to have various possible orientations. A gradient of Fe content is found in the α–Al(Fe,Mn)Si dispersoids due to slow diffusion of Fe into dispersoids during annealing.

Keywords: aluminum alloys; TEM; electron diffraction; orientation relationship

1. Introduction

Constituent particles form during solidification of wrought non-heat treatable 3xxx aluminum alloys. The constituent phases are very important in these Al alloys as they influence recrystallization, grain size, texture and mechanical properties [1,2].

With Mn, Fe and Si as the main alloying elements, Direct Chill (DC)-cast 3xxx alloys contain mainly two types of constituent particles, an orthorhombic Al_6(Fe,Mn) phase and a body centred cubic (bcc) α–Al(Fe,Mn)Si phase [3]. A high Si content favours the formation of α–Al(Fe,Mn)Si, while the Al_6(Fe,Mn) phase predominates in alloys with less Si content. The Al_6(Fe,Mn) phase may transform to the bcc α–Al(Fe,Mn)Si phase during homogenization heat treatment if the Si level is sufficiently high in the alloy. This phase transformation has been extensively studied [4–10]. The phase selection of intermetallic particles during solidification is also dependent of the nucleation undercooling and growth kinetics of different eutectics [11].

In the as-cast state, the Al matrix is supersaturated with Mn and Si [12]. Homogenization has to be carried out to reduce the solid solution level and get the optimum size and density of both the larger constituent particles and the smaller dispersoids before mechanical processing. Although recent studies show that dispersoids precipitated during low-temperature

*Corresponding author. Email: astrid.muggerud@ntnu.no

homogenization also have a significant strength contribution [14,15], work hardening is the main strengthening mechanism of the 3xxx alloys [5,12,13].

Recently, many studies have been conducted on the precipitation behaviour of dispersoids, and the orientation relationships (ORs) between dispersoids and the aluminum matrix [11–20]. For the $Al_6(Fe,Mn)$ dispersoids an OR of $[\bar{1}\,1\,0]_p//[2\,1\,\bar{1}]_m$, $(0\,0\,1)_p//(3\,\bar{1}\,5)_m$ has been found as the most common [26]. Moreover, studies of the α–Al(Fe,Mn)Si dispersoids have revealed various ORs [18–20]. In a recent study, the α–Al(Fe,Mn)Si dispersoids have been shown to be partly coherent with the Al matrix, following a common OR $[1\,\bar{1}\,1]_p//[1\,\bar{1}\,1]_m$, $(5\,\bar{2}\,\bar{7})_p//(1\,1\,0)_m$ [14].

The type and morphology of constituent particles formed during solidification are much dependent of the nucleation and growth kinetics of the particles [11], which are strongly correlated to the OR and the interfacial energy between the constituent particles and aluminum matrix. However, little work has been reported on the OR between constituent particles and Al matrix. Detailed information on phase type, lattice parameters, morphology and compositional studies of dispersoids and constituents is also lacking. Such studies are important for an in-depth understanding of the nucleation mechanisms and growth behaviour of particles in these alloys. Therefore, the main goal of this work is to carry out a systematic study on the type, morphology and compostion, and also orientation relationships of constituent particles and the aluminum matrix.

2. Experimental

Two DC cast billets with different Si contents produced by Hydro Aluminum in Norway were studied. The chemical compositions of the alloys were measured by mass spectroscopy and are given in Table 1. In addition to the main alloying elements Fe, Si and Mn, traces of Cu, Mg, Zn, Cr, Ni, Pb and Sn in amounts less than 0.01 wt% were detected. In the rest of this work, the Si-poor alloy is called Alloy 1 and the Si-rich is called Alloy 2, according to Table 1.

An air circulating furnace was used for heat treatments. The alloys were heated from room temperature with a heating rate of 50 K/h up to the annealing temperature of 450°C, then annealed for 24 h before water quenching. In order to have a more throughout study of the material and phase properties after low-temperature annealing, the same annealing treatment of 450°C and chemical composition of alloys was used in the present study, as in [15].

Transmission Electron Microscopy (TEM) foils were made by electro polishing of thin discs with an electrolyte containing two parts Methanol and one part of Nitric acid at −20°C using a Struers TenuPol-5 electro polishing unit, applying a voltage of 20 V and a current of ∼150 mA.

Extraction of constituent particles and dispersoids by Butanol dissolution was done. Details of the dissolution method are given elsewhere [21,22]. The extracted powders were analysed by powder x-ray diffraction (XRD) (Siemens D 5000) to determine the phases and lattice parameters of different particles. Pure Si was used as the reference sample material for XRD lattice parameter determination.

A Phillips CM30 TEM operating at 150 kV was used for microstructure investigations and electron diffraction studies. A Jeol 2010F TEM operating at 200 kV equipped with an energy dispersive X-ray spectrometer (EDS) detector from Oxford Instruments was used

Table 1. Chemical composition of alloy 1 and 2, main alloying elements.

Alloy	Fe [wt%]	Mn [wt%]	Si [wt%]
1	0.504	0.970	0.148
2	0.497	0.992	0.480

for the composition measurements. Nano-beam mode was used to reduce the volume of matrix included in the measurements in the TEM.

For the Scanning Electron Microscopy (SEM) studies, a Zeiss Supra SEM with a Secondary Electron (SE) detector was used for morphology studies, while a Hitachi SU-6600 with a Back Scattered Electron (BSE) detector was used for atomic number contrast micrography.

3. Results and discussion

3.1. *Phase identification by XRD*

XRD spectra of the extracted powders from alloy 1 and alloy 2 are shown in Figure 1(a) and (b), repectively. The Si peaks stem from the reference sample material. Table 2 summarizes the identified phases and their lattice parameters.

In alloy 1, one Al_6(Fe,Mn) phase and two α–Al(Fe,Mn)Si phases are identified. Al_6(Fe,Mn), labelled c in Figure 1(a), is the predominant constituent phase. The measured values of the lattice parameters given in Table 2 are in between the lattice parameters of Al_6Fe and Al_6Mn [23]. The phase labelled as α1c in Figure 1(a) is the constituent α–Al(Fe,Mn)Si phase and the phase labelled α1d is the α–Al(Fe,Mn)Si dispersoid phase in alloy 1.

Two types of the α–Al(Fe,Mn)Si phase are also identified in alloy 2. α2c in Figure 1(b) is the constituent phase and α2d in alloy 2 in Figure 1(b) is the dispersoid phase. Both are α–Al(Fe,Mn)Si phases, but have slightly different lattice parameters, as seen from Table 2.

3.2. *Chemical composition of particles*

EDS measurements of the chemical composition of constituent particles and dispersoids were performed in order to determine the composition of the phases. An average Fe/(Fe+Mn) ratio of 0.60 was measured in constituent Al_6(Fe,Mn) phase c in alloy 1. Since the fraction of α–Al(Fe,Mn)Si constituent particles transformed from Al_6(Fe,Mn) constituents is very small, no measurement was performed on these particles.

In alloy 2, the constituent α–Al(Fe,Mn)Si phase, labelled as α2c, has an average Fe/(Fe+Mn) ratio of 0.65. The constituent particles in both alloys have a relatively high Fe content, as they have precipitated during solidification of the alloys.

For alloy 1, the dispersoid phase labelled as α1d has an average Fe/(Fe+Mn) ratio of 0.08. For alloy 2, the Fe/(Fe + Mn) ratio of the dispersoid phase labelled as α2d is measured to be about 0.07.

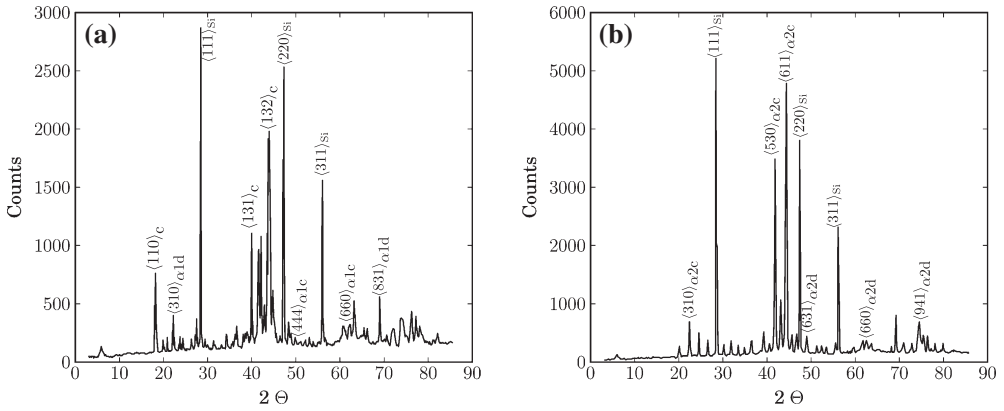

Figure 1. XRD spectrum of alloy 1 (a) and alloy 2 (b). Si is used as reference sample material. Dominating peaks are indexed with corresponding phase and lattice plane. (a) α1d is the α–Al(Fe,Mn)Si dispersoid phase, α1c is the α–Al(Fe,Mn)Si constituent phase and the constituent Al_6(Fe,Mn) phase is named c. (b) α2c is the constituent α–Al(Fe,Mn)Si phase and α2d the α–Al(Fe,Mn)Si dispersoid phase.

Table 2. Lattice parameters for the dispersoid and constituent phases in alloy 1 and 2, determined by XRD measurements.

Alloy	1	2
Constituent phase	bcc α–Al(Fe,Mn)Si (α1c)	bcc α–Al(Fe,Mn)Siα2c)
Lattice parameter (Å)	a = 12.581 ± 0.013	a = 12.589 ± 0.002
Constituent phase	orth. Al_6(Fe,Mn) (c)	
Lattice parameter (Å)	a = 6.477 ± 0.009, b = 7.490 ± 0.011 c = 8.802 ± 0.012	
Dispersoid phase	SC α–Al(Fe,Mn)Si (α1d)	SC α–Al(Fe,Mn)Si(α2d)
Lattice parameter (Å)	a = 12.655 ± 0.015	a = 12.644 ± 0.005

The content of Mn and Fe in the α–Al(Fe,Mn)Si phases can also be estimated by a linear interpolation between the lattice parameters of pure AlMnSi and AlFeSi phases, as shown in Figure 2. The shaded area is the possible lattice parameters within standard deviations between AlMnSi and AlFeSi [24,25]. The lattice parameters determined by XRD makes it possible to estimate the ratio between Fe and (Fe+Mn) in the phases. The estimated ratios are matched with the EDS measurements when using the lower area of the linear interpolation area from lattice parameters of AlMnSi and AlFeSi.

A linear interpolation for the lattice parameters of the α–Al(Fe,Mn)Si constituent in alloy 1 and 2, indexed as α1c and α2c, gives a Fe/(Fe+Mn) ratio of 0.70 in α1c and 0.65 in α2c. For α2c, this estimation is in good agreement with the EDS measurements.

For the α–Al(Fe,Mn)Si dispersoid phases in alloy 1 and 2, indexed as α1d and α2d in Figures 1 and 2, Fe/(Fe+Mn) ratios of 0.08 in α1d and 0.10 in α2d were estimated. Compared with the EDS measurements, which gave an Fe/(Fe+Mn) ratio 0.08 for α1d and

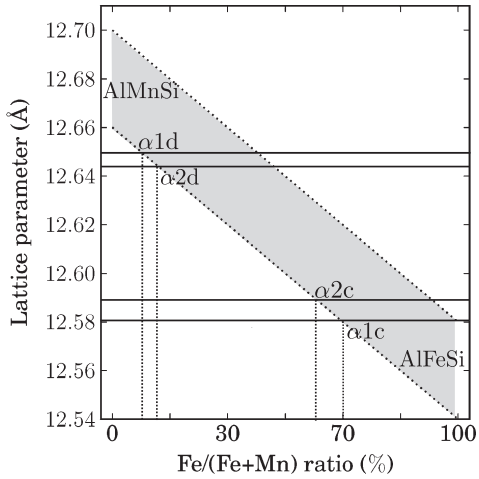

Figure 2. Lattice parameters of α1d and α1c in alloy 1 and α2d and α2c in alloy 2 plotted in a linear interpolation between lattice parameters of AlMnSi and AlFeSi. The lattice parameters of AlMnSi and AlFeSi are taken from [24,25]. This can be used to estimate the Fe and Mn compositions.

0.07 for α2d, also a good correspondence is found. We can see that alpha dispersoids contain much less Fe than the alpha constituent particles.

A large scatter in Fe and Mn content measured by EDS was found in the dispersoids in both alloy 1 and 2. The scatter is not only between various dispersoids, but also inside a single dispersoid. Figure 3(a) shows a dispersoid in alloy 2. The EDS acquisitions were performed at points 1–8. The corresponding Fe/(Fe+Mn) ratio is plotted in Figure 3(b). As seen from the figure, the edges of the dispersoid contains more Fe than the central part. This may imply that the α–Al(Fe,Mn)Si dispersoids have precipitated without Fe (as α–AlMnSi), but as the dispersoids grow, Fe diffuses into the particles. Due to the slow diffusion of Fe and Mn in the particles, a significant gradient of Fe content exists in the particles.

3.3. *Morphology of constituent particles*

Figure 4 shows overview BSE SEM micrographs of the constituent particles in alloy 1 and 2. All the particles are distributed at the grain boundaries and in the interdendritic areas. The Al_6(Fe,Mn) phase in alloy 1 is shown in Figure 4(a) and the α–Al(Fe, Mn)Si constituent phase in alloy 2 is shown in (b). The Al_6(Fe,Mn) particles (a) have a rounded shape, while the α–Al(Fe,Mn)Si particle in (b) are larger and have a more complex eutectic morphology.

Figure 5 shows TEM and SE SEM micrographs of extracted Al_6(Fe,Mn) particles from alloy 1. The constituents consist of branches which are rounded at the edges due to Oswald ripening during annealing.

Some α–Al(Fe,Mn)Si constituent particles transformed from the Al_6(Fe,Mn) phase were observed in alloy 1. An example is shown in Figure 6. The brighter spots inside the particle are the so-called Al sposts, described in [5,6], which are due to the eutectoid phase trasformation. Figure 6(b) shows the corresponding diffraction pattern of the transformed particle in (a). In (c) the simulated diffraction pattern shows good correspondence with the

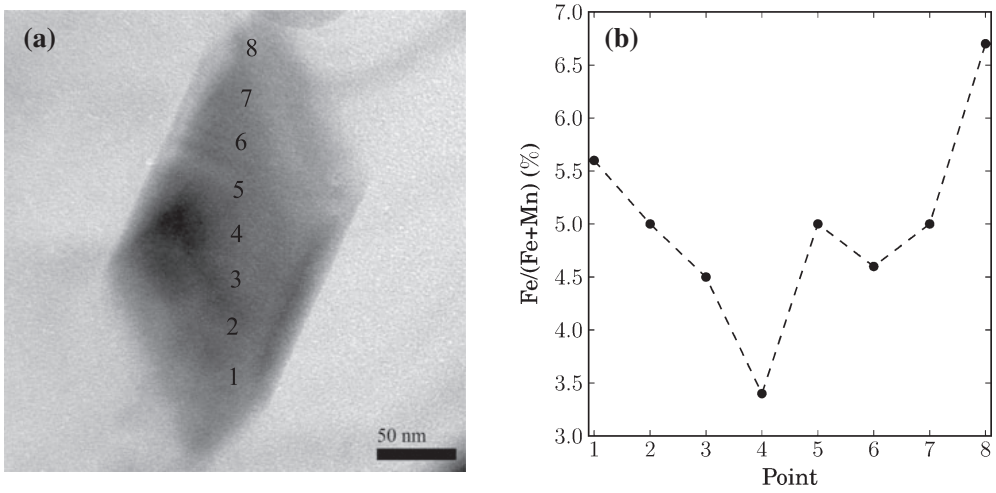

Figure 3. (a) α–Al(Fe,Mn)Si dispersoid in alloy 2, α2d. (b) EDS measurements of Fe/(Fe+Mn) ratio at 8 points along the dispersoid.

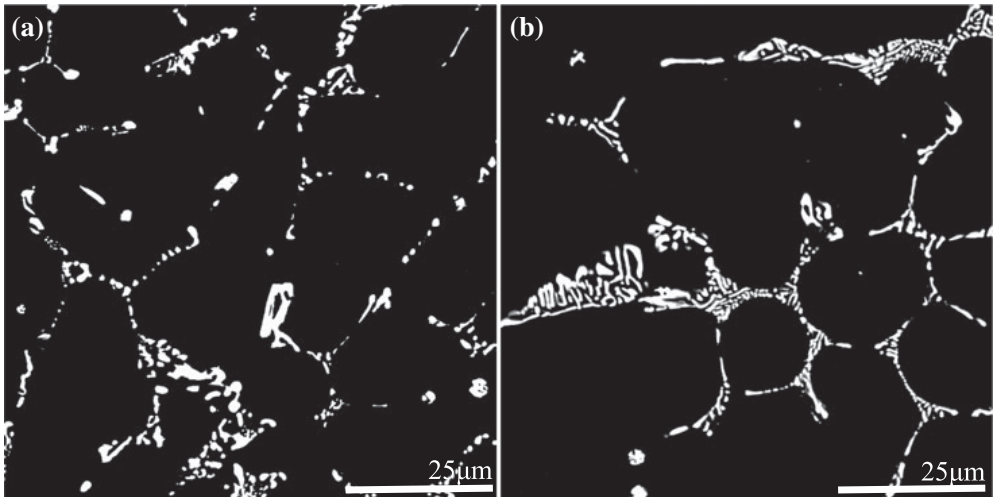

Figure 4. BSE micrographs of the constituents particles in alloy 1 and 2. (a) Al_6(Fe,Mn) particles in alloy 1. (b) α–Al(Fe,Mn)Si particles in alloy 2.

diffraction pattern in (b), verifying the bcc structure of the α- particle transformed from Al_6(Fe,Mn) particle.

Figure 7 shows the TEM and SE SEM micrograph of an extracted α–(Fe,Mn)Si constituent particle in alloy 2. This particle has a complex three-dimensional morphology. The α–(Fe,Mn)Si particles are larger and consist of more branches. The edges of the branches are rounded as for the Al_6(Fe,Mn) particles in Figure 5 due to the Oswald ripening.

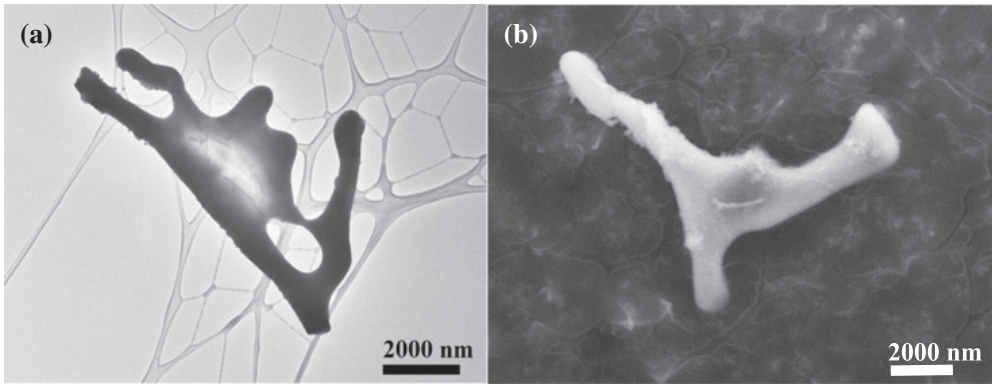

Figure 5. Extracted constituent $Al_6(Fe,Mn)$ particles from alloy 1. (a) TEM micrograph of particle (b) SE SEM micrograph of another particle. Both the TEM and SEM micrographs show the smooth and branched morphology of the constituent $Al_6(Fe,Mn)$ particles.

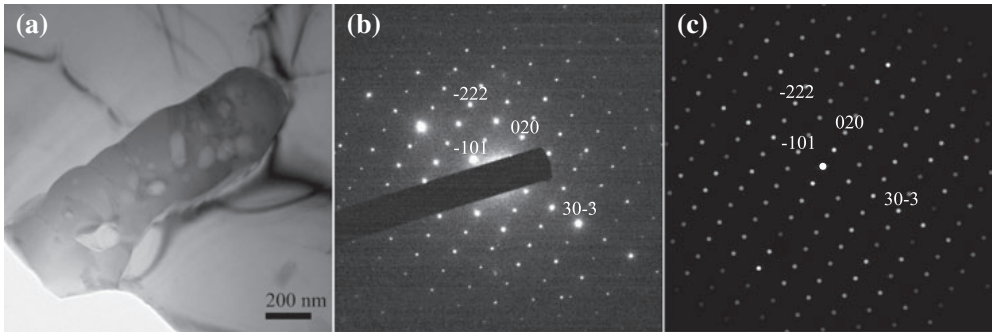

Figure 6. (a) Transformed bcc α–Al(Fe,Mn)Si constituent particle in alloy 1. (b) Diffraction pattern of zone axis $[1\,0\,1]_{\alpha}$ with corresponding simulation in (c).

3.4. *OR between Al matrix and constituent particles*

The constituent particles are often located at grain boundaries and have specific OR to one of the Al grains. Although some ripening has occurred in the constituent particles during annealing treatment, no change is expected in the OR to the Al matrix. The ORs determined after annealing treatment are therefore also representative for the constituent particles formed during solidification.

3.4.1. *$Al_6(Fe,Mn)$ constituent particles*

Figure 8(a) shows a TEM micrograph with $Al_6(Fe,Mn)$ constituent particles located at a random high-angle grain boundary of Al matrix in alloy 1. The lowest grain is oriented approximately along the $[\bar{1}\,1\,\bar{1}]_{Al}$ zone, while the upper Al grain is not along any specific low index zone axis orientation.

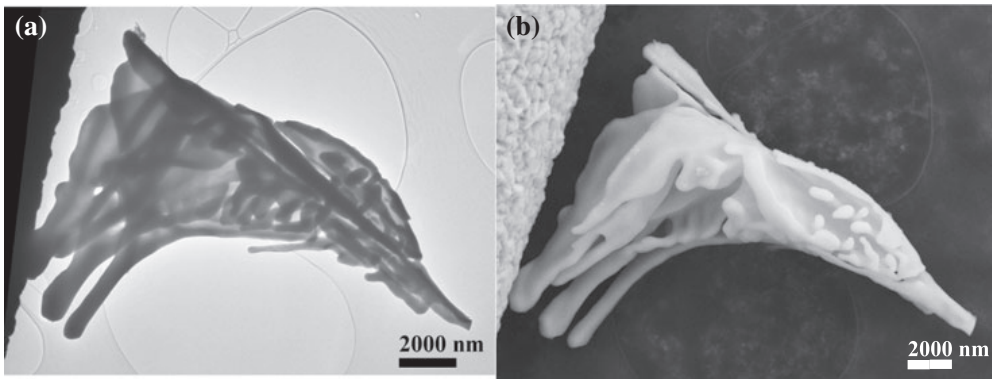

Figure 7. Extracted constituent α–Al(Fe,Mn)Si phase in alloy 2. (a) TEM micrograph of particle. (b) SEM micrograph of the same particle as in (a). The branched morphology of the phase is clear both from the TEM and the SEM micrographs.

Figure 8(b) shows a diffraction pattern of particle 1 in (a). The OR between the particle and the Al matrix can be approximately written as $[\bar{1}\,\bar{1}\,\bar{2}]_C//[\bar{1}\,1\,\bar{1}]_{Al}$, $(3\,3\,\bar{3})_C//(0\,\bar{2}\,\bar{2})_{Al}$, with a deviation angle of 3° between $(3\,3\,\bar{3})_C$ and $(0\,\bar{2}\,\bar{2})_{Al}$. The deviation of the lower Al grain $[\bar{1}\,1\,\bar{1}]_{Al}$ zone is less than 0.5°.

Figure 8(c) shows the diffraction pattern of the constituent particle 2 in (a). It shows the same OR as constituent particle 1. The zone axis of the diffraction pattern of particle 2 deviates from $[\bar{1}\,\bar{1}\,\bar{2}]_C$ with 2.2°. The edges of particle 2 towards the lower Al grain are more rounded than for particle 1.

Particles 1 and 2 have about the same orientation, which implies that the two particles probably are two branches of the same constituent particle. The constituent particle has most likely nucleated on one of the aluminum grains, and therefore shows a specific orientation with this. The surface in the upper Al grain is rounded for both of the particles, implying that the particle was attached to the upper grain after nucleation on the lower grain. During growth, it is natural that the two branches deviate a bit from the original orientation of the parent particle.

The OR in Figure 8(b) is equivalent to the orientation described by Li et al. for plate shaped $Al_6(Fe,Mn)$ dispersoids of the same phase [26]. Approximately the same OR is also found for Al_6Mn dispersoids in cold rolled Al [17] and for Al_6Mn dispersoids after annealing [16,27]. Li et al. [26] have determined a precise orientation between the $Al_6(Fe,Mn)$ dispersoids and Al matrix, $[\bar{1}\,1\,0]_C//[2\,1\,\bar{1}]_{Al}$ and $(0\,0\,1)_C//(3\,\bar{1}\,5)_{Al}$. It means that the constituent particles in Figure 8 have the same OR to Al matrix as the $Al_6(Fe,Mn)$ dispersoids. Figure 8 (d) shows the simulated diffraction pattern along $[\bar{1}\,1\,\bar{1}]_{Al}$ made using the precise orientaion determined by Li et al. [26]. A good agreement can be found between the simulated and experimental diffraction pattern.

A corresponding rotation matrix was also given to calculate the parallel directions between $Al_6(Fe,Mn)$ dispersoids and the Al matrix [26]. By applying this rotation matrix, experimental ORs found in the present work have been examined. The majority of the ORs are equivalent to the most common OR for $Al_6(Fe,Mn)$ dispersoids. This means that the constituent particles have nucleated on a pre-existing Al grain. Investigations have been

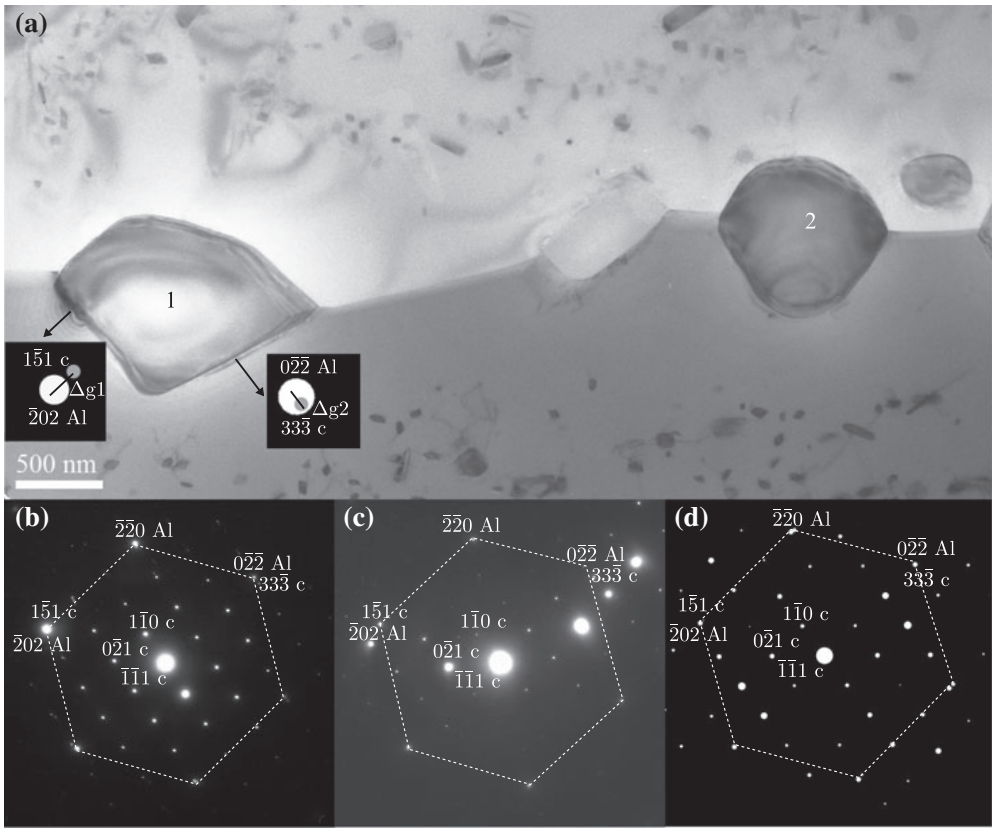

Figure 8. (a) $Al_6(Fe,Mn)$ constituent particles along an Al grain boundary in alloy 1. (b) Diffraction pattern of constituent particle 1 and lower Al grain with approximate OR $[\bar{1}\,\bar{1}\,\bar{2}]_c//[\bar{1}\,1\,\bar{1}]_{Al}$, $(3\,3\,\bar{3})_c//(0\,\bar{2}\,\bar{2})_{Al}$. (c) Diffraction pattern of constituent particle 2 and lower Al grain in (a), with deviation angle of 2.2° from $[\bar{1}\,\bar{1}\,\bar{2}]_c$. (d) Simulation of diffraction pattern with OR $[\bar{1}\,\bar{1}\,\bar{2}]_c//[\bar{1}\,1\,\bar{1}]_{Al}$, $(3\,3\,\bar{3})_c//(0\,\bar{2}\,\bar{2})_{Al}$.

done on a large number of $Al_6(Fe,Mn)$ constituents, and show that most of the particles follow the observed OR. However, also other orientations have been observed in limited number.

It is interesting to see that particle 1 in Figure 8(a) has two faceted surfaces in the lower Al grain, with specific OR between the particle and Al matrix. With the specific OR between the $Al_6(Fe,Mn)$ constituent and Al matrix, and the large differences in lattice parameters, the faceted surface may have singular structures at the interface [28,29].

Such possible singular interfaces can be identified with the Δg approach, by applying the Δg parallelism rules [28,29]. Δg is the difference vector relating the two reciprocal lattice systems. The interfaces meeting the Δg parallelism rule, namely the normal of the interface is parallel to a Δg, will likely have a singular structure. The system in Figure 8 fits the Δg parallelism rule I, with Δgs parallel to rational **g** vectors.

In Figure 8(a), two areas are magnified sections of the simulated diffraction pattern in Figure 8(d). The simulated diffraction pattern is better suited for Δg investigations due to

abberations and stigmation from the microscope in the experimental diffraction pattern. Two possible Δg singular interface directions are inserted, corresponding to reciprocal directions perpendicular to the side facets of particle 1. The direction of the Δg vector can be calculated from the reciprocal lattice directions in the two phases by $\Delta g1 = (g(1\,\bar{5}\,1)_c - g(\bar{2}\,0\,2)_{Al})$, giving $\Delta g1$ parallel with $(\bar{1}\,\bar{1}\,1)_c//(0\,1\,1)_{Al}$ plane normal directions. $\Delta g2 = (g(0\,\bar{2}\,\bar{2})_{Al} - g(3\,3\,\bar{3})_c)$ gives $\Delta g2$ parallel with $(\bar{1}\,1\,0)_c//(3\,1\,\bar{2})_{Al}$ plane normal directions.

The singular interfaces found here are different than the habit planes found for dispersoids of the same phase. This is natural as the dispersoids and constituent phases have precipitated under different conditions. The dispersoids precipitate in the solid, while the constituent particle form in the liquid metal.

3.4.2. *α–Al(Fe,Mn)Si constituent particles*

In alloy 2, the bcc α–Al(Fe,Mn)Si constituents are also located at Al grain boundaries and interdendritic areas. In this study, different ORs have been found between the matrix and the α–Al(Fe,Mn)Si constituents.

Figure 9(a) shows two branches of the same large constituent α–Al(Fe,Mn)Si particle. Both particle 1 and particle 2 are located inside the left Al grain, which is oriented along $[1\,1\,1]_{Al}$. Particle 2 is connected to the high-angle Al grain boundary, stippled in Figure 9(a).

Figure 9(b) shows the diffraction pattern of particle 1 and left Al grain taken along $[1\,1\,1]_{Al}$, with a deviation angle of 2.0° from $[1\,1\,3]_\alpha$ zone axis. The OR in Figure 9(c) can be written approximaetly as $[1\,1\,1]_{Al}//[1\,1\,3]_\alpha$, $(\bar{8}\,2\,2)_\alpha//(2\,0\,\bar{2})_{Al}$. The plane normal directions $(\bar{8}\,2\,2)_\alpha$ and $(2\,0\,\bar{2})_{Al}$ have a deviation angle of approximately 2°. Figure 9(d) shows a simulated diffraction pattern of the OR in (c), and a very good correspondence is found.

Figure 10(a) and (d) show bcc α–Al(Fe,Mn)Si constituents at an Al grain boundary, with the left grain tilted to the $[1\,0\,1]_{Al}$ zone axis in (a) and the right grain tilted to $[1\,0\,1]_{Al}$ zone axis in (d), respectively. The grain boundary is a high-angle grain boundary with a tilting angle between the two $[1\,0\,1]_{Al}$ zone axis of 19° and rotation angle of 55° between the two grains.

Particle 1 is related to the left Al grain with an approximate OR of $[1\,0\,1]_{Al}//[2\,0\,5]_\alpha$, $(\bar{5}\,1\,2)_\alpha//(\bar{1}\,1\,1)_{Al}$ shown in the diffraction pattern in Figure 10(b). The angle between plane normal directions $(\bar{5}\,1\,2)_\alpha$ and $(\bar{1}\,1\,1)_{Al}$ is approximately 4°. Particle 1 does not show any OR with the right Al grain. The corresponding simulation of the OR in Figure 10(b) is shown in Figure 10(c).

Figure 10(e) shows the diffraction pattern of the right Al grain and particle 2, with an approximate OR $[1\,0\,1]_{Al}//[1\,2\,3]_\alpha$, $(5\,2\,\bar{3})_\alpha//(0\,2\,0)_{Al}$. The angle between the plane normal directions $(5\,2\,\bar{3})_\alpha$ and $(0\,2\,0)_{Al}$ is approximately 4°. It is interesting to see that $(5\,2\,\bar{3})_\alpha$ and $(0\,2\,0)_{Al}$ are nearly coincident. For α–Al(Fe,Mn)Si dispersoids precipitated in 3xxx alloys, $\{5\,2\,3\}_\alpha$ and $\{0\,0\,2\}_{Al}$ are also the most frequently observed coincident planes [14]. Constituent 2 does not show any orientation relationship with the left Al grain. Figure 10(f) shows the corresponding simulated diffraction pattern of the OR in Figure 10(e). A good agreement between experimental and simulated diffraction patterns can be seen.

As the two constituents in Figure 10(a) and (d) are related to different Al grains, they belong to two different larger constituent particles.

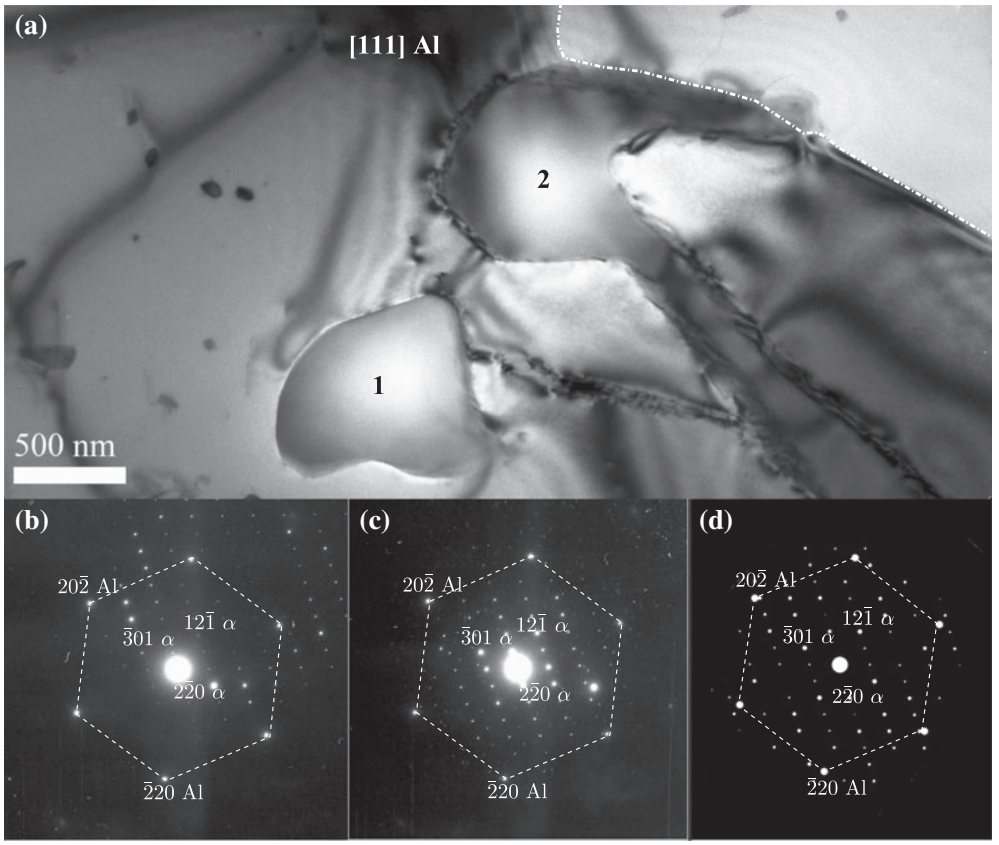

Figure 9. (a) Two branches of constituent bcc α–Al(Fe,Mn)Si phase in alloy 2. Particle 2 is at the grain boundary. Left Al grain oriented along $[1\,1\,1]_{Al}$. The grain boundary is stippled in white. (b) Diffraction pattern of particle 1, zone axis $[1\,1\,1]_{Al}//[1\,1\,3]_{\alpha}$, 2° deviation from $[1\,1\,3]_{\alpha}$. (c) Diffraction pattern of particle 2 with zone axis $[1\,1\,1]_{Al}//[1\,1\,3]_{\alpha}$, $(\bar{8}\,2\,2)_{\alpha}//(2\,0\,\bar{2})_{Al}$. (d) Simulation of diffraction pattern in (c).

The rotation matrix used by Li et al. [14] for α–Al(Fe,Mn)Si dispersoids was applied to examine the ORs found for the constituent phase. No match with the common OR for dispersoids was found, except the above-mentioned coincident plane pair $(5\,2\,\bar{3})_{\alpha}//(0\,2\,0)_{Al}$.

In contrast to the Al_6(Fe,Mn) constituent particles, the α–Al(Fe,Mn)Si constituent particles do not show the same OR as the α–Al(Fe,Mn)Si dispersoids. This can be attributed to different conditions for the nucleation of the two phases, one at high temperature during solidification, the other at lower temperature during annealing.

Nucleation and growth undercooling are important parameters for the phase selection in the Fe and Mn bearing systems, see i.e. [11]. The α–Al(Fe,Mn)Si constituents and the Al_6(Fe,Mn) constituents show strong OR with the Al matrix, meaning that the particles have nucleated on the Al grains. The possibility for good lattice matching at the interface between particle and Al matrix may lower the nucleation and growth undercooling for the Al_6(Fe,Mn) and α–Al(Fe,Mn)Si phases. It will also influence the kinetics of the eutectic growth of constituent particles and favour the formation of a specific morphology of the particles.

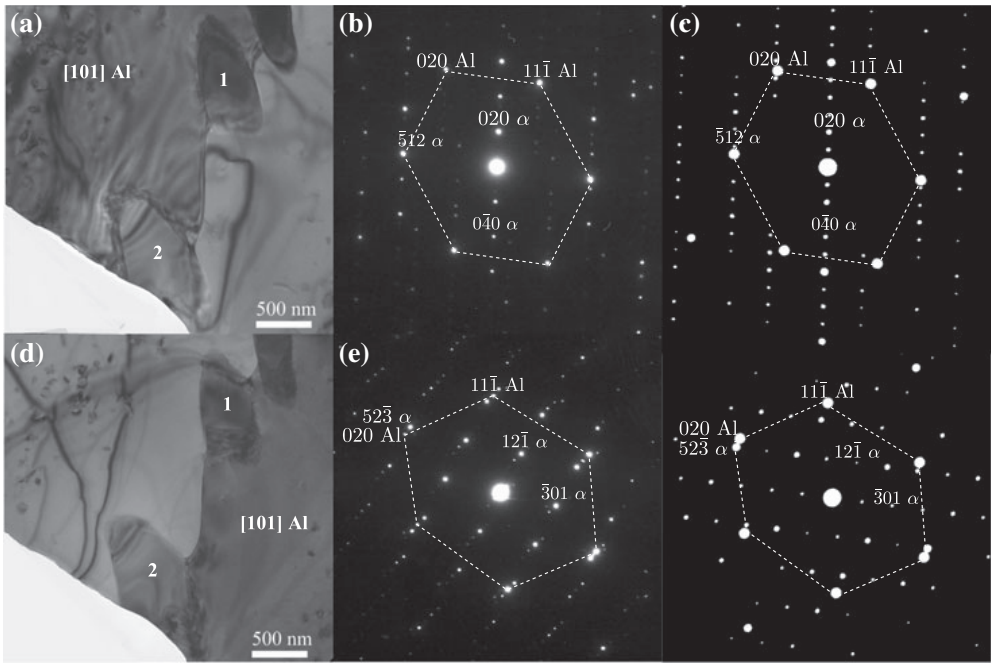

Figure 10. (a) Constituent bcc α–Al(Fe,Mn)Si particles at an Al grain boundary in alloy 2. Left grain at $[1\,0\,1]_{Al}$ zone axis. (b) Diffraction pattern of left Al grain and particle 1 in (a) with parallel zones $[1\,0\,1]_{Al}//[2\,0\,5]_{\alpha}$, $(\bar{5}\,1\,2)_{\alpha}//(\bar{1}\,1\,1)_{Al}$. (c) Simulation of diffraction pattern in (b). (d) Right Al grain at $[1\,0\,1]_{Al}$ zone axis. (e) Diffraction pattern of right Al grain and particle 2 with OR $[1\,0\,1]_{Al}//[2\,0\,5]_{\alpha}$, $(5\,2\,\bar{3})_{\alpha}//(0\,2\,0)_{Al}$ zone axis. (f) Simulation of diffraction patten in (e).

4. Conclusion

Lattice parameters, chemical compostions and orientation relationships of orthorhombic $Al_6(Fe,Mn)$ constituent particles in a low Si content alloy, α–Al(Fe,Mn)Si constituent particles in a high Si content Al alloy and α–Al(Fe,Mn)Si dispersoids in both alloys have been studied.

Lattice parameters have been determined by XRD, and the Fe and Mn content have been measured by EDS. α–Al(Fe,Mn)Si dispersoids have likely precipitated as AlMnSi during annealing and Fe have diffused into the dispersoid during growth.

The α–Al(Fe,Mn)Si constituent particles are larger and show a more complex morphology than the $Al_6(Fe,Mn)$ constituent particles. Both phases have rounded edges due to Oswald ripening.

Orientation relationship studies of the constituent particles show that the constituent orthorhombic $Al_6(Fe,Mn)$ phase has the same OR as found for Al_6Mn and $Al_6(Fe,Mn)$ dispersoids, namely $[\bar{1}\,1\,0]_c//[2\,1\,\bar{1}]_{Al}$, $(0\,0\,1)_c//(3\,\bar{1}\,5)_{Al}$.

For the constituent α–Al(Fe,Mn)Si particles, various ORs were found which are different from the most common OR of α–Al(Fe,Mn)Si dispersoids in 3xxx alloys. However, the same coincident planes $\{5\,2\,3\}_{\alpha}$ and $\{0\,0\,2\}_{Al}$, as between α–Al(Fe,Mn)Si dispersoids and Al matrix were found.

Acknowledgements

This work has been supported by the KMB project MoReAl financed by The Research Council of Norway, and the industrially partners Hydro and Sapa Technology. Sindre Bunkholt, NTNU, is acknowledged for help with BSE SEM imaging. Christian Simensen is acknowledged for help with particle extraction and orgainzation of the XRD measurements.

References

[1] F. Humphreys, Acta Metall. 25 (1977) p.1323.
[2] E. Nes, Acta Metall. 24 (1976) p.391.
[3] L. Backerud, E. Krol and J. Tamminen, *Solidification Characteristics of Aluminum Alloy: Wrought Alloys*, Vol. 1, Skanaluminium, Univeritetsforlaget AS, Oslo, 1986.
[4] H. Watanabe, K. Ohori and Y. Takeuchi, Aluminium (English Edition) 60 (1984) p.e310.
[5] D.T.L. Alexander and A.L. Greer, Acta Mater. 50 (2002) p.2571.
[6] D.T.L. Alexander, R.G. Hamerton, H. Cama and A.L. Geer, Light Met. 50 (2002) p.2571.
[7] W. Hutchinson, A. Oscarsson and A. Karlsson, Mater. Sci. Technol. 5 (1989) p.1118.
[8] Y.J. Li and L. Arnberg, Mater. Sci. Eng., A 347 (2003) p.130.
[9] P. Furrer, Zeitscrift für Metallkunde 70 (1979) p.699.
[10] E. Trömborg, A.L. Dons and L. Arnberg, Investigation of the Al6(Fe, Mn) to α–Al(Fe, Mn)Si phase transformation during homogenisation of AA3003 and AA3004 aluminum alloys, ICAA3, Trondheim, 1992, p.270.
[11] Y.J. Li and L. Arnberg, Acta Mater. 52 (2004) p.2673.
[12] Y. Li and L. Arnberg, Acta Mater. 51 (2003) p.3415.
[13] J. Courbon, Mater. Sci. Forum 331–337 (2000) p.17.
[14] Y.J. Li, A.M.F. Muggerud, A. Olsen and T. Furu, Acta Mater. 60 (2012) p.1004.
[15] A.M.F. Muggerud, E.A. Mørtsell, Y. Li and R. Holmestad, Mater. Sci. Eng., A 567 (2013) p.21.
[16] J.I. Kong, J.I. Suk and S.W. Nam, J. Mater. Sci. Lett. 15 (1996) p.763.
[17] P. Yang, O. Engler and H.-J. Klaar, J. Appl. Phys. 32 (1999) p.1105.
[18] P. Donnadieu, G. Lapasset and T.H. Sanders, Philos. Mag. Lett. 70 (1994) p.319.
[19] V. Hansen, B. Anderson, J.E. Tibbals and J. Gjønnes, Metall. Mater. Trans. B 26B (1995) p.839.
[20] V. Hansen and J. Gjønnes, Philos. Mag. A: Phys. Condens. Matter: Defects Mech. Prop. 73 (1996) p.1147.
[21] C.J. Simensen and A.I. Spjelkavik, Z. Anal. Chem. 300 (1980) p.177.
[22] C.J. Simensen, P. Fartum and A. Andersen, Fresenius Z. Anal. Chem. 319 (1984) p.286.
[23] W.B. Pearson, *The Crystal Chemistry and Physics of Metals and Alloys*, Wiley Interscience, New York, 1972.
[24] M. Cooper, Acta Cryst. 20 (1966) p.614.
[25] M. Cooper, Acta Cryst. 23 (1967) p.1106.
[26] Y. Li, W. Zhang and K. Marthinsen, Acta Mater. 60 (2012) p.5963.
[27] J.I. Kong, J.I. Suk and S.W. Nam, Mater. Lett. 28 (1996) p.385.
[28] W.-Z. Zhang and G.C. Weatherly, Prog. Mater. Sci. 50 (2005) p.181.
[29] W.Z. Zhang and X.P. Yang, J. Mater. Sci. 46 (2011) p.4135.

Paper III

Mackay icosahedron explaining orientation relationship of dispersoids in Al alloys

Accepted for publication in Acta Crystallographica Section B

Mackay icosahedron explaining orientation relationship of dispersoids in Al alloys

Astrid Marie F. Muggerud[a]*, Yanjun Li[b], Randi Holmestad[a] and Sigmind J. Andersen[c]
[a] NTNU, Department of Physics, Trondheim, N-7491, Norway
[b] NTNU, Deparment of Materials Science and Engineering, Trondheim, N-7491, Norway
[c] SINTEF Materials and Chemistry, Trondheim, N-7465, Norway

Correspondence email: astrid.muggerud@ntnu.no

Synopsis The orientation of dispersoids of the cubic icosahedral quasicrystal approximation phase α-Al(Fe,Mn)Si in aluminium matrix have been studied by electron diffraction. The commonly observed orientation relationship is explained by an internal fixed orientation of the inner part Mackay icosahedron of the structure.

Abstract The orientation relations (ORs) of the cubic icosahedral quasicrystal approximation phase α-Al(Fe,Mn)Si have been studied after low temperature annealing of a 3xxx wrought aluminum alloy by transmission electron microscopy. From diffraction studies it was verified that the most commonly observed OR for the α-Al(Fe,Mn)Si dispersoids is $[1\,\bar{1}\,1]\,\alpha$ // $[1\,\bar{1}\,1]$ Al, $(5\bar{2}\bar{7})\,\alpha$ // (011) Al. This orientation could be explained by assuming that the Mackay icosahedron (MI) internal in the α-phase has a fixed orientation in relation to Al, similar to that of the icosahedral quasi-crystals existing in this alloy system. It is shown that mirroring of the MI normal to high symmetry icosahedral directions explains alternative orientations, which are therefore likely to be caused by twinning of the fixed MI. Only one exception was found, which was related to the MI of the T-phase in Al-Mg-Zn.

1. Introduction

The medium strength 3xxx wrought aluminum alloys, with Mn as main alloying element, are used in various applications such as packaging and architecture (Courbon 2000; Alexander & Greer 2002; Li & Arnberg 2003). 3xxx aluminum alloys are "non-heat treatable alloys" as they gain their strength mainly through work hardening. Homogenization is the essential first processing step before further mechanical processing, and is performed to eliminate micro segregation, reduce solid solution level of Mn and obtain the right size and density of both constituent particles and dispersoids.

Dispersoids are important because of their influence on mechanical properties such as hardness, on recrystallization and texture development (Li & Arnberg 2003; Humphreys 1977; Nes 1976; Suni *et al.* 1998; Li & Arnberg 2003; Merchant *et al.* 1990; Hausch *et al.* 1978). By controlling the homogenization treatment a desired amount and distribution of dispersoids can be obtained. Recent studies have shown a remarkable hardening effect caused by the precipitation of a large amount of fine dispersoids during low temperature annealing (Li *et al.* 2012; Muggerud *et al.* 2013).

Composition and heat treatment govern the types of dispersoids to precipitate. In addition to Mn, Fe and Si are always present in commercial 3xxx alloys. The Si and Fe content reduces

the solubility of Mn in the Al matrix and enhances the precipitation of dispersoids (Hausch *et al.* 1978). The two main types of dispersoids in the commercial 3xxx alloys are the cubic α-Al(Mn,Fe)Si phase and the orthorhombic Al_6(Fe,Mn) phase (Li & Arnberg 2003; Li & Arnberg 2003; Hausch *et al.* 1978¸ Hutchinson *et al.* 1989; deHaan *et al.* 1996). With a low Si content α-Al(Mn,Fe)Si phase exists at low temperatures, but dissolve at higher temperatures. The Al_6(Fe,Mn) phase precipitates as the stable phase in alloys with a low Si content (Li & Arnberg 2003; Li & Arnberg 2003; Hausch *et al.* 1978; Alexander *et al.* 2002; Furrer 1979). In alloys with a high Si content Al_6(Fe,Mn) do not precipitate, which means that the Si stabilizes α-Al(Mn,Fe)Si. The variation of Mn/Fe ratio of α-Al(Mn,Fe)Si will slightly change its crystal structure. It is simple cubic (sc) when the content is low, while a higher content of Fe results in a body centred cubic (bcc) structure, as well as a smaller cell (Tiballs *et al.* 2001; Tiballs *et al.* 1989).

The crystal structure of α-AlMnSi was described by Cooper *et al.* (1966) and has later been refined (Sugiyama *et al.* 1998; Fowler *et al.* 1988) . The unit cell belongs to space group Pm-3 (#200), contains 138 atoms and has a lattice parameter of 12.68Å. It is nearly bcc since the main structural components are two almost identical Mackay icosahedra (Mackay 1962) (MIs) centered at 000 and ½,½,½ (Elser & Henley 1985; Guyot & Audier 1985). Ideally, the MI here is a 54 atom aggregate composed of three concentric polyhedra: two 12 atoms icosahedra surrounded by a shell of 30 Al atoms located outside each of the 30 icosahedral two-fold edges, forming an icosidodecahedron. While the inner icosahedron of the MI is a mix of Al and Si, the second icosahedron contains the 12 Mn and/or Fe atoms. The remaining 30 atoms may be considered to form outer shared shells binding the MIs together. Figure 1 shows the three layered structure of the MacKay icosahedron.

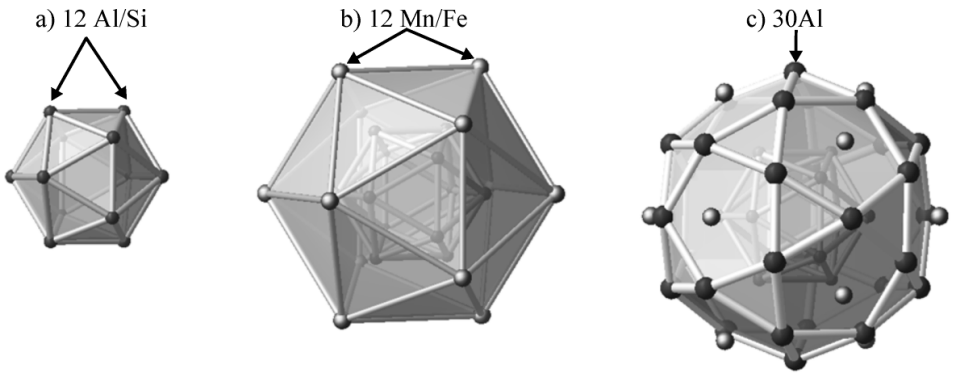

Figure 1 The three-layered structure of the 54 atom MI in the α-phase viewed along a 3-fold axis, coinciding with a <111> α direction. The MI contains three concentric shells. a) The inner icosahedron of 12 Al/Si atoms. b) The surrounding icosahedron consisting of 12 Mn/Fe atoms. c) Al-atoms outside each of the 30 twofold edges of the Mn/Fe icosahedron constitute an icosidodecahedron. Similar figures can be found in Jarić & Gratias (1989).

In α-AlFeSi, the two MIs at the corner and in the center are identical. This results in a bcc structure, with space group Im-3 (#204) (Cooper 1967) and a smaller lattice constant of 12.56Å. The dispersoids in the present study are α-dispersoids, containing both Fe and Mn, sc structured with space group Pm-3. In a previous study of the dispersoids in the same alloy and under under the same annealing conditions as used in the present work, the ratio

Fe/(Fe+Mn) was measured to be 0.10. The lattice parameter was determined as 12.644±0.005Å by x-ray diffraction (Muggerud *et al.* 2014) .

The α-Al(Mn,Fe)Si phase is a so-called "quasicrystalline" approximant. Several studies have been conducted on the transformation from icosahedral quasicrystalline (IQC) to crystalline α-phase for the Al-Mn-Si system (Hansen *et al.* 1989; Hansen & Gjønnes 1996; Dubois *et al.* 1986; Pannetier *et al.* 1987; Stern & Ma 1987; Koskenmaki *et al.* 1986). Koskenmaki *et al.* (1986) reported the coherent directional orientation relationship (OR) between the IQC phase and the cubic α-phase in a rapid solidified Al-Mn-Si alloy. Investigating such approximant phases is important for better understanding of quasicrystals. The IQC will also, as commonly the initially formed phase nucleating the dispersoids, be directly coupled to the mechanical properties of the alloys, by governing dispersoid development, numbers and sizes.

Various ORs between Al matrix and the α–Al(Fe,Mn)Si dispersoids have been reported in earlier studies (Hansen & Gjønnes 1996; Hansen *et al.* 1995). In recent work the most common OR for the cubic α–Al(Fe,Mn)Si was determined to be

OR1: $[1\,\bar{1}\,1]\,\alpha$ // $[1\,\bar{1}\,1]$ Al, $(5\bar{2}\bar{7})\,\alpha$ // (011) Al (Li & Arnberg 2003; Li *et al.* 2012) (1)

The dispersoids were found to be partly coherent with the Al matrix. In the present work the most common OR is verified as OR1. Although not observed here, the simplest OR is obviously when the unit cells of Al and the α-phase are parallel. This OR will in the following be referred to as OR2. It is shown how OR1 and OR2 both relate to the MI and the IQC orientation in the Al matrix. A few exceptions from the OR are discussed.

2. Experimental

The experimental material was a DC cast billet produced by Hydro Aluminum AS, Norway. The chemical composition of the alloy was measured to 0.50 wt% Fe, 0.48 wt% Si and 0.99 wt% Mn by mass spectroscopy. Samples were taken from the axial center of the 20 cm ingot and cut into 2x2x1 cm^3 blocks. An air circulating furnace was used for the low temperature homogenization treatment from room temperature with a heating rate of 50°C/hour up to 450°C. The samples were homogenized for 12 or 24 hours before water quenching. TEM foils were prepared by electro-polishing with a Struers TenuPol-5 electro polishing unit at -20°C, with an electrolyte containing methanol and nitric acid. Two transmission electron microscopes (TEMs) were used, a Philips CM30 operated at 150 kV, and a Jeol 2010F operated at 200kV.

3.1 Results and discussion

3.1 Observed orientation relationships

A large number of dispersoids were studied with respect to their OR with the aluminum matrix. Table 1 shows the alloy composition, observed OR, number of dispersoids observed and heat treatment. In addition to the present investigations, Li *et al.* (2012) studied ~50 dispersoids in an AA3003 alloy. As can be seen in the table, the vast majority of the dispersoids follow OR1 (Li *et al.* 2012), as defined in Equation 1.

Table 1 Alloy composition, homogenisation treatment and OR of the α-dispersoids in the present and the alloy in the work of Li *et al.* (2012).

Alloy	Alloying elements (wt%)	OR	Number of dispersoids	Heat treatment
1	0.99 Mn, 0.50 Fe, 0.48 Si	OR1	~40	50°C/hr to 450°C, 12-24 hr annealing, water quenching
		$[100]\alpha$ // $[100]$Al, $(053)\alpha$ // (001)Al	1	
		$[100]\alpha$ // $[111]$Al, $(001)\alpha$ // $(10\bar{1})$Al	1	
		$[101]\alpha$ // $[105]$Al, $(010)\alpha$ // (010)Al	1	
		$[411]\alpha$ // $[11\bar{1}]$Al, $(\bar{2}\bar{1}9)\alpha$ // $(\bar{1}0\bar{1})$Al	1	
2	1.15 Mn, 0.58 Fe, 0.20 Si	OR1	~50	50°C/hr to 300°C, 24 hr annealing, water quenching (Li *et al.* 2012).
		$[100]\alpha$ // $[100]$Al, $(011)\alpha$ // (001)Al	1	

3.2 Explaining the most commonly observed orientation relationship

As mentioned in the introduction, Koskenmaki *et al.* (1986) found that the IQC phase and the cubic α-phase in a rapidly solidified Al-Mn-Si alloy show a simple orientation relation. Three $<100>\alpha$ directions are parallel to three orthogonal 2-fold icosahedral axes, and all $<111>\alpha$ directions are parallel to 3-fold icosahedral axes. This is exactly the orientation relation between the internal MI and the α-phase itself, which means that the (iso-symmetric) IQC and this MI have identical orientation. The OR of the IQC (or the internal MI) suffices to explain the most important orientation relation OR1 and also OR2 in Al of the α-phase. Note that this all depends on the assumption of a single IQC orientation in Al.

As shown by Elser *et al.* (1985) and Guyot *et al.* (1985), for the IQC phase, the 2-fold, 3-fold and 5-fold rotational symmetry axes of the icosahedron fall either along some low index Al directions or along irrational directions, where one or more indices must be approximated by a series of Fibonacci numbers (F_n)[1], and where limits are expressed by the golden mean $\tau = \frac{1}{2}\left(1+\sqrt{5}\right) = 2\cos\frac{\pi}{5}$.

There are 30 edges in an icosahedron associated with 2-fold axes. From these axes orthogonal vector sets can be selected. In Figure 2, an icosahedron is viewed along a 2-fold a) and 3-fold

[1] The series starts as 1, 1, 2, 3, 5, 8, 13,$\cdots F_n$, and the next Fibonacci number is obtained by adding the current number to the previous ($F_{n+1} = F_{n-1} + F_n$).

b) direction. Two generic orthogonal basis vector sets are indicated, with black and grey arrows. They are completely equivalent from the perspective of the icosahedron. One such set always coincides with unit cell bases of the α-phase. This means the $<100>$ and $<\tau\tau^2 1>$ type sets shown in Figure 2 a) are identical. Two vector sets which may represent the two generic systems are $\{[100], [010], [001]\}$ and $\{[\tau\tau^2\bar{1}], [\tau^2\bar{1}\tau], [\bar{1}\tau\tau^2]\}$, shown also as **a**, **b**, **c** and **a'**, **b'**, **c'** in Figure 2 a). The 5-fold axes refer to indices without parentheses, while vector indices for 2-fold directions are given in square brackets.

With the <100> type bases, the unit cells of Al and α-phase are parallel, and all $<111>$ directions are common and parallel with 3-fold MI axes. This gives rise to orientation relation OR2. For the $<\tau\tau^2 1>$ type, while the internal MI is oriented identically with the first type, the unit cell of the α-phase is not, and the three orthogonal basis vectors now fall along irrational directions in the aluminum and just one of the $<111>$ directions is common. This gives rise to the most frequently observed orientation relation OR1, defined by Equation 1. This means that the α-phase has at least one $<111>$ direction common with the aluminum matrix. From symmetry, there are four equivalent $<\tau\tau^2 1>$ type base systems for the icosahedron, these cannot be separated from each other unless different variants occur in the same Al grain, and for example in the same diffraction pattern.

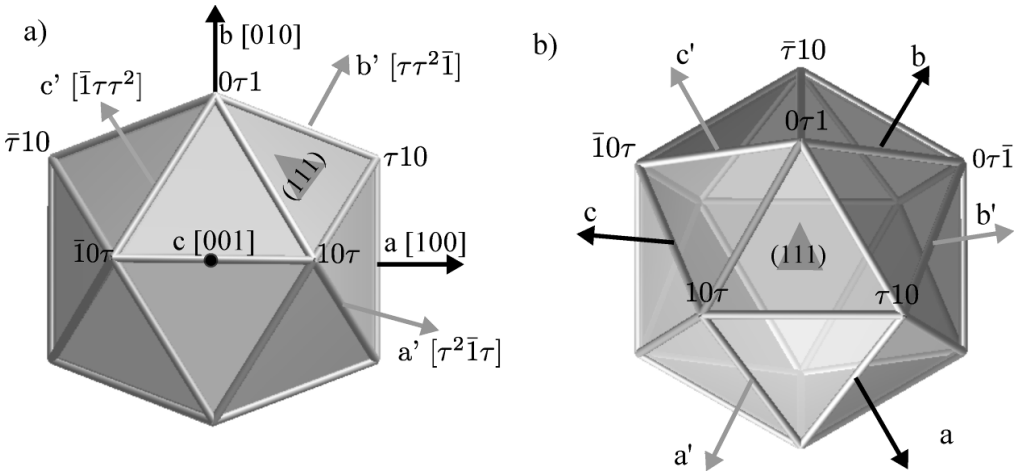

Figure 2 An icosahedron viewed along two of its symmetry axes; 2-fold a) and 3-fold b). Triples of 2-fold axes represent orthogonal bases for the α-phase in Al coordinates. The $<\tau\tau^2 1>$ set represents irrational Al directions (gray arrows) denoted **a'**, **b'**, **c'** (OR1). The $<100>$ set (black arrows denoted ***a***, ***b***, ***c***) has bases parallel with Al (OR2). Coordinates of type $\tau 10$ show icosahedral vertices giving directions of 5-fold symmetry. 2-fold directions are given in brackets. b) shows that both systems have a common (111) plane.

The corners in Figure 2 a) and b), define the 5-fold directions, all of type $<\tau 10>$. Summing two such neighboring 5-fold axes gives a 2-fold direction by using the relation

$$\tau^n + \tau^{n+1} = \tau^{n+2} \qquad (2)$$

where n is a positive or negative integer. As an example **b'** = [$\tau\tau^2\bar{1}$], the sum of [$0\tau\bar{1}$] and [$\tau 10$], since $\tau + 1 = \tau^2$, easily seen in Figure 2 b).

The most commonly observed orientation relation OR1, given in Equation 1 is now understandable. The first part of OR1 says that a $<111>$ zone is common for α and Al. In the second part of OR 1 in Equation 1, plane indices are not identical. The second set, $<\tau\tau^2 1>$, in Figure 2 a) is chosen. One of the $<110>$ Al directions normal to **[**111**]**, for example **[**$10\bar{1}$**]**, should coincide in the α-system with $<257>$ α type direction. Expressing the Al unit in terms of the second set (disregarding vector length), we obtain

$$[10\bar{1}]\ \text{Al} = [\tau\tau^2\bar{1}] - [\bar{1}\tau\tau^2] = [\tau^2, 1, -(\tau^2+1)] \sim [52\bar{7}]\,\alpha. \qquad (3)$$

The same types of indices are obtained with the two other $<110>$ vectors normal to $[111]$ direction.

To sum up, with the $<100>$ type bases, the $<100>$ axes of Al and α-phase are parallel, and all $<111>$ directions are common. This gives rise to orientation relation OR2. For the $<\tau\tau^2 1>$ type, while the internal MI is oriented identically with the first type, the unit cell of the α-phase is not. The three orthogonal basis vectors now fall along irrational directions in the aluminum and just one of the $<111>$ directions is common. This gives rise to the most frequently observed orientation relation OR1, defined by Equation 1. Both these ORs can be said to have arisen from the same IQC if the respective dispersoid are decomposed from such phase. Looking at a single MI, OR1 and OR2 are identical. The α-dispersoids are also important in e.g. the 6xxx Al alloy system. Since several other Fe and Mn containing particles in Al alloys are known to contain icosahedral units it is likely that the icosahedron explanation model described above is not restricted to just the α-dispersoids of the 3xxx alloy system.

3.3 Examples of the most common orientation relationship

One example of OR1 is given in Figure 3, where the bright field (BF) images in a) and d) show the same α–Al(Fe,Mn)Si dispersoid in two orientations after 24 hours homogenization at 450°C. Diffraction patterns of the corresponding orientations are shown in b) and e), and simulated diffraction patterns in c) and f) respectively. There is a good match between the simulated and recorded diffraction patterns. The dispersoid in Figure 3 b) is indexed as a common $<111>$ zone of Al and the α-phase. To connect the two zones, absolute directions are necessary. Here $[111]\,\alpha$ and $[11\bar{1}]$ Al were chosen as zone axes. It is found that $7\bar{5}\bar{2}\,\alpha$ and 022 Al reflections overlap, which indicates the particle is in orientation OR1. The dispersoid is found to have the follow relation: $[111]\,\alpha$ // $[11\bar{1}]$ Al, $(7\bar{5}\bar{2})\,\alpha$ // (011) Al.

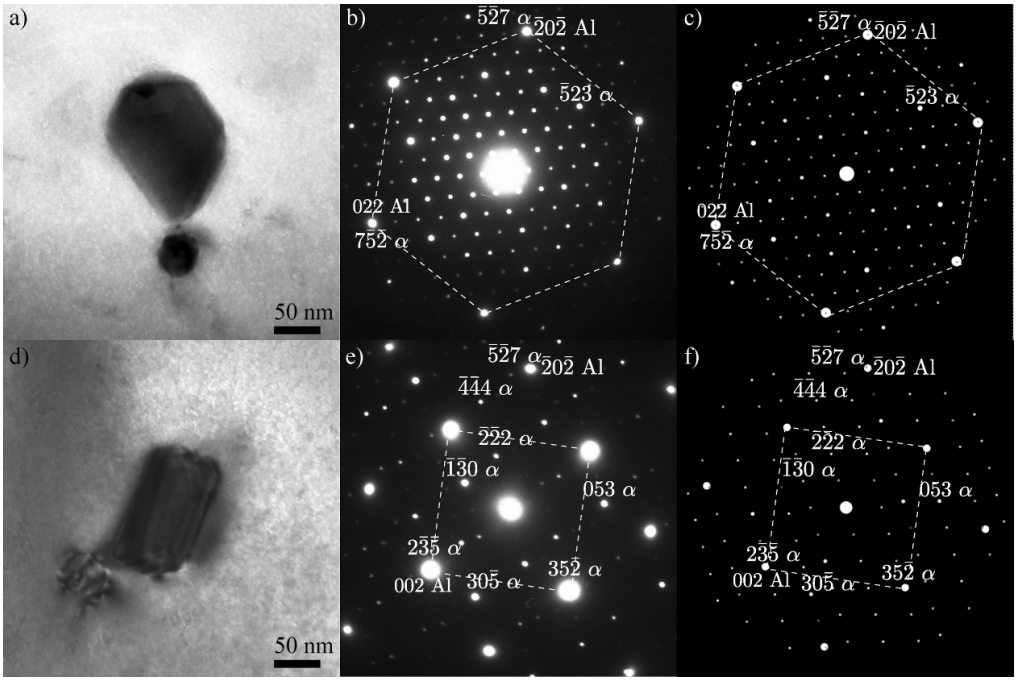

Figure 3 BF images and diffraction patterns of the same α-dispersoid in two orientations. a) and b) Dispersoid along zone axes of **[**111**]**α // **[**11$\bar{1}$**]**Al. c) Corresponding simulation of diffraction pattern in b). d) and e) Dispersoid tilted to zone axes of **[**8$\bar{3}$5**]**α // **[**010**]**Al. f) Corresponding simulation of diffraction pattern in e).

After tilting, as shown in Figure 3 d), e) and f), the OR of the dispersoid can be determined as **[**8$\bar{3}$5**]**α// **[**010**]**Al, **(**2$\bar{3}\bar{5}$**)** α //**(**001**)** Al, which should be an alternative way of giving OR1. To see this, one can notice that the indices of the α -phase spots are part of the two Fibonacci (vector) sequences

$$\mathbf{[}3\,\bar{1}2\mathbf{]},\ \mathbf{[}5\bar{2}3\mathbf{]},\ \mathbf{[}8\bar{3}5\mathbf{]},\ \cdots\ [\tau^2\bar{1}\tau] \text{ and } \mathbf{[}1\bar{2}\bar{3}\mathbf{]},\ \mathbf{[}2\bar{3}\bar{5}\mathbf{]},\ \mathbf{[}3\bar{5}\bar{8}\mathbf{]},\ \cdots\ [1\bar{\tau}\overline{\tau^2}]. \qquad (4)$$

The limits of the Fibonacci sequences are mutually normal vectors, i.e. $[\tau^2\bar{1}\tau]\cdot[1\bar{\tau}\overline{\tau^2}]=0$, and equal to the bases **a'** and **-c'** shown in Figure 2. The dispersoid therefore follows the common OR1. The physical tilt of the specimen in the microscope must be equal to the angle between the zone axes in both phases in order for the system to be consistent. Between **[**11$\bar{1}$**]**Al and **[**010**]**Al the tilt angle is 54.7°, almost identical with the tilt from **[**111**]**α to **[**8$\bar{3}$5**]**α of 54.3°. These tilt angles between the zone axes are in a very good correspondence with the experimental estimated tilt of the specimen holder of 55.1°. The indexing of the OR system is consistent.

Figure 3 a) and d) also illustrate that the shape of the dispersoid is complex. In the (111) Al zone of Figure 3 a) the projection shows 5 facets, while in the (001) Al zone in b) a more rectangular morphology is apparent. More images are needed to determine the real shape.This

illustrates how a TEM micrograph may easily lead to misinterpretation of the true morphology of objects.

Figure 4 a) shows an α–Al(Fe,Mn)Si dispersoid after 12 hours homogenization at 450°C. By tilting, the dispersoid morphology is found to be plate-like and is viewed edge on in Figure 4. A higher resolution of part of the right-hand side interface of a) is given in b). In c) the corresponding fast Fourier transform (FFT) image is shown. The OR of the dispersoid and the surrounding Al matrix is found from the FFT pattern to be $[75\bar{2}]\alpha$ // $[110]$Al, $(1\,\bar{1}\,1)\alpha$ // $(1\,\bar{1}\,\bar{1})$Al, which is equivalent with OR1 as given in Equation 1. There is a near coincidence of the reflections $1\,\bar{1}\,\bar{1}$ Al with $3\bar{3}3\,\alpha$, and $00\bar{2}$ Al with $3\bar{5}\bar{2}\,\alpha$. The first pair implies a common $<111>$ zone. The second pair shows a vector of Fibonacci indices, see Equation 3, extending along an Al base. This implies a set of irrational directions parallel with the Al bases. The dispersoid in Figure 4 is therefore also a variant of the most common OR1.

In Figure 4 b) the directions along and perpendicular to the habit plane trace are shown. The dispersoid and matrix planes along the zone axes have a very small misfit of planar spacing, only 0.01%, given by $d^{\alpha}_{75\bar{2}}$=1.4317Å and d^{Al}_{220} =1.4315Å. Along the habit plane trace are the vectors $[1\bar{3}\bar{4}]\alpha$ and $[\bar{1}12]$Al, which show a very good match in the associated planes, having a misfit of only 0.004%, given by $3d^{Al}_{\bar{2}24}$ = 2.4798 Å, and $d^{\alpha}_{1\bar{3}\bar{4}}$=2.4797 Å. However, the misfit of planar spacing between $(1\,\bar{1}\,1)\alpha$ and $(1\,\bar{1}\,\bar{1})$Al habit planes of the two phases is rather large, 3.9% given by $d^{\alpha}_{1\bar{1}\bar{1}}$=7.300 Å and $3d^{Al}_{1\bar{1}\bar{1}}$= 7.014 Å. Thus, there is a better match along the habit plane compared to along the planes normal to the habit plane. This explains why the dispersoid has a plate shape. In Figure 4 a) the length of the dispersoid is ~150 nm, while the thickness is ~25 nm. The coinciding plane pair normal $(3\bar{5}\bar{2})\alpha$ // $(00\bar{2})$Al in the habit plane, indexed in Figure 3 c), was also present in the habit plane $(\bar{5}4\bar{2})\alpha$ // $(12\,\bar{1})$Al found in another alloy by Li *et al.* (2012). The lattice parameter for the α-dispersoid used is 12.644 Å, based on the measurements of the lattice parameter in the same alloy (Muggerud *et al.* 2014).

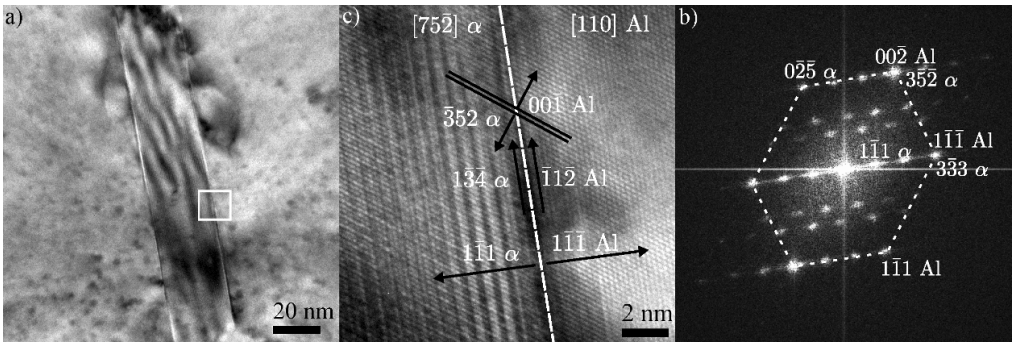

Figure 4 a) Plate like α- dispersoid viewed edge on. b) Higher resolution of the area marked with a square in a). The directions along and perpendicular to the habit plane trace are shown. c) FFT of the micrograph in b), indicating OR $[75\bar{2}]\alpha$ // $[110]$Al, $(1\,\bar{1}\,1)\alpha$ // $(1\,\bar{1}\,\bar{1})$Al.

Even though the majority of the dispersoids follow one OR, the picture is more complex regarding the habit planes, as is evident from the examples in Figures 3 and 4, where these dispersoids, with the exact same OR have obtained very different morphology. The semi-coherent nature of the dispersoids results in many possible habit plane candidates for the dispersoids following the commonly observed OR1. Also, the variation of lattice parameter of the α-phase with changing contents of Fe and Mn will change the preferential habit plane and therfore the final morpholgy.

3.4 Deviations from the commonly observed orientation relationship

OR2, with the unit cells of Al and α-phase parallel, and all $<111>$ directions common has not been observed experimentally in this work. However, different variants of OR2 with one $<100>$ direction in common for Al and the α-phase have been observed, as listed in Table 1. These ORs can be described by growth from an initially OR2 along different mirror planes of the icosahedron in the α-phase. Two such mirror plane variants of OR2 are shown in the following. In addition, another type of OR, also deviating from the commonly observed OR1 are presented and discussed.

Figure 5 a) shows a bright field TEM micrograph of an α-dispersoid in the alloy presented as alloy 2 in Table 1 (Li *et al.* 2012). The dispersoid has plate shaped morphology. The corresponding diffraction pattern and simulated diffraction pattern are shown in b) and c). The dispersoid is found to follow an OR $[001]\alpha$ // $[001]$Al, $(110)\alpha$ ~// (010)Al. As described above, in the icosahedron model OR2 has all <100> Al axes parallel to the <100> two-fold icosahedron axis in the α-phase. One $<001>$ direction is common for Al and the α-phase in Figure 5. The OR shown in Figure 5 can be explained from OR2, with a mirror plane with 3-fold axis as normal vector.

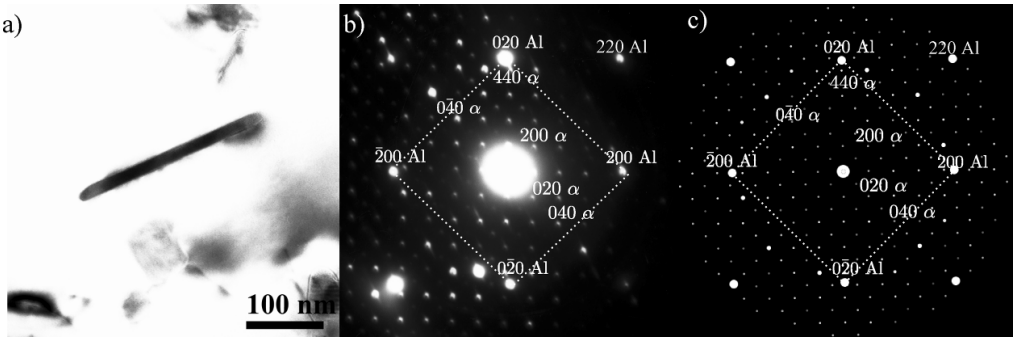

Figure 5 a) Bright field TEM image of an α-dispersoid, b) diffraction pattern and c) corresponding simulated diffraction pattern showing OR $[001]$ Al // $[001]\alpha$, (010) Al // $(110)\alpha$.

Figure 6 a) shows a 2-fold projection of the icosahedron along the common $[001]\alpha$/Al direction (OR2). The OR of Figure 5 is produced when two icosahedra share a (3-fold) face, but grow mirrored. The shared face to the left on the top of Figure 6 a) represents a mirror plane with the stippled icosahedron.

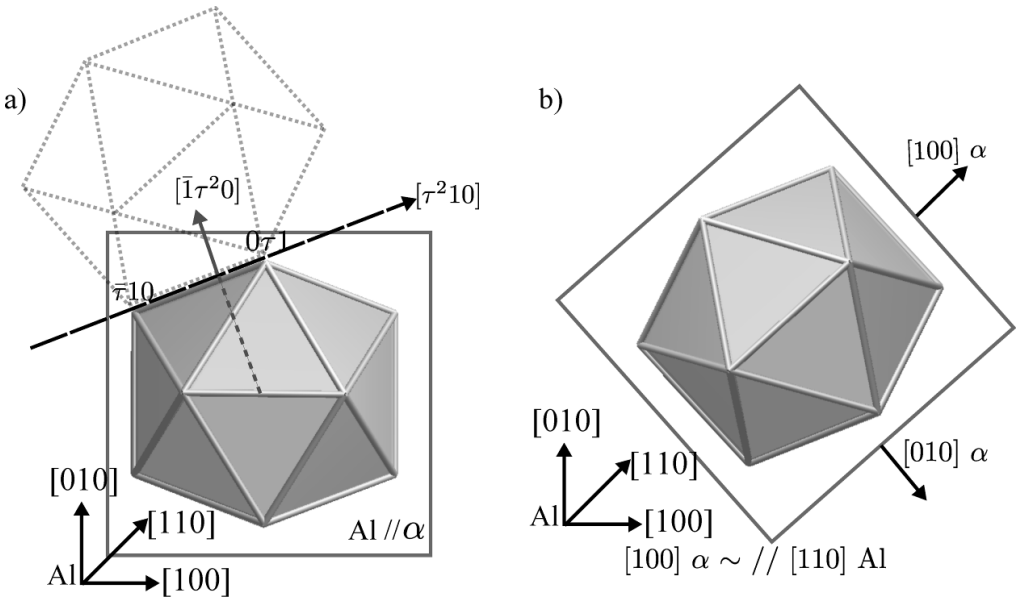

Figure 6 a) 2-fold projection of the icosahedron along the common **[**010**]** α/Al direction, with mirror plane trace $[\tau^2 10]$. b) Resulting icosahedron after mirroring, with the plane pair **(**110**)** α and **(**100**)** Al approximately parallel. The square represents the respective unit cell orientations of α.

The normal to this face is the 3-fold axis $[\bar{1}\tau^2 0]$. The direction can be found by the respective three 5-fold axes surrounding the face, $[\bar{\tau}10]$, $[0\tau 1]$ and $[0\tau\bar{1}]$ (not shown). The direction of the trace of the mirror plane is the stippled vector $[\tau^2 10]$. The resulting icosahedron is shown in Fig 6 b) with the plane pair **(**110**)** α ~// **(**010**)** Al. The deviation angle between the $<110>$ Al and $<100>$ α directions (or vice versa) is measured to ~3.1° in the diffraction pattern in Figure 5 b). It fits nicely with the theoretical deviation angle θ of 3.2°, with mirror angle 2ω:

$$2\omega = 2\angle([100]\cdot[\tau^2 10]) = 2\cos^{-1}(\frac{\tau}{\sqrt{3}}) = 41.8^o,\ \theta = 45^o - 2\omega = 3.2^o. \qquad (5)$$

If the mirrored icosahedron with orientation shown in Figure 6 b) is repeated on the expense of the parent icosahedron shown in Figure 6 a), the (α-phase) OR in Figure 5 b) can be obtained.

Figure 7 shows an α-dispersoid with a cube shape, tilted to two different zone axes in a) and d) around the common **[**010**]** axis. From the diffraction pattern and corresponding simulated diffraction pattern of the dispersoid and surrounding Al matrix in Figure 7 b) and c), the dispersoid is found to follow the OR **[**101**]** α // **[**501**]** Al, **(**010**)** α // **(**010**)** Al. In Figure 7 d), the dispersoid is tilted to the zone axies of **[**305**]** α // **[**100**]** Al, as shown in the diffraction pattern in e).

The angle between [101]α and [305]α, and between [501]Al and [100]Al are 14.0° and 11.3°, respectively. A high index zone such as [501]Al is easily misaligned with a few degrees, especially if the particle is thin normal to the zone axis.

In Figure 7 f) a high resolution image of the lower left area in d) is shown. The plane pair (020)α // (020) Al coincides with the side edges of the particle in both orientations and is the likely habit plane for this dispersoid. A very strong moiré pattern can be seen on the particles in the habit plane direction. The periodicity of the fringes is given by the inverse difference between the reciprocal lattice vectors in the two systems $\boldsymbol{g}_{\mathrm{M}} = \boldsymbol{g}_2 - \boldsymbol{g}_1$ (Williams & Carter 2009). Here $\boldsymbol{g}_1 = \boldsymbol{g}^{\alpha}_{060}$ and $\boldsymbol{g}_2 = \boldsymbol{g}^{\mathrm{Al}}_{020}$, according to Figure 7. The resulting periodicity $d_{\mathrm{M}} = \left|\boldsymbol{g}_{\mathrm{M}}\right|^{-1} = 5.4$ nm, in perfect correspondence to the measured moiré periodicity in Figure 7. a) of 5.4 nm.

One <001> direction is common for Al and the α-phase in Figure 7, as for the dispersoid in Figure 5. Also the OR shown in Figure 7 can be explained from OR2, however with a slightly more complex mirror plane direction than for the dispersoid in Figure 5. Kuo *et al.* (2002) explains how there are two possible ways to connect two Mackay icosahedrons together through a 5-fold rotation axis. Two icosahedrons of the same OR can be connected and share a vertex, or two icosahedrons of reverse orientation can be connected through a mirror plane.

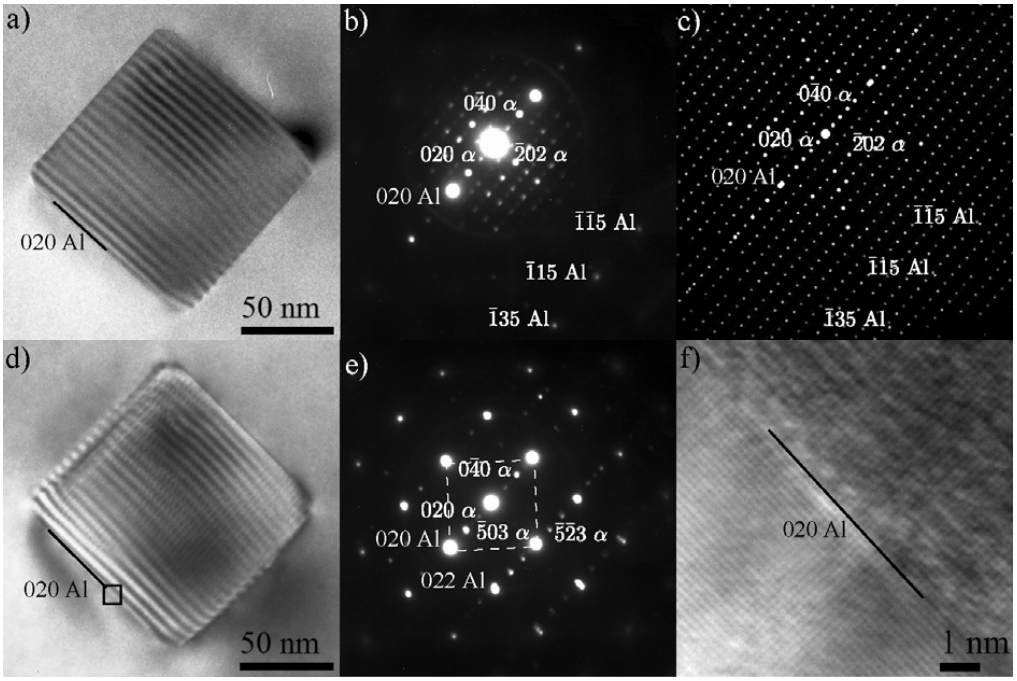

Figure 7 a) Cubed-shaped dispersoid. b) Experimental diffraction pattern and simulated diffraction pattern c) of the dispersoid in a) with OR found to be close to [101]α // [501]Al, (010)α // (010)Al. d) The same dispersoid as in a) tilted to new zone axis, of [305]α // [100]Al, as shown in e). f) High resolution micrograph of lower left part of side edge in d).

Figure 8 a) shows a 2-fold projection of the icosahedron along the common **[**010**]** α/Al direction. The icosahedron can be connected, through a mirror plane, to an icosahedron with the OR found experimentally in Figure 7. The mirror plane is defined by the 2-fold, common **[**010**]** direction of Al and α, and a 5-fold axis in the paper plane. The mirror plane is illustrated by the stippled lines in Figure 7 a). The result of the mirror plane is an icosahedron where the **[**$\bar{5}0\bar{1}$**]** Al direction becomes parallel with **[**101**]**α, equivalent with Figure7 b). The resulting icosahedron OR is shown in Figure 8 b). The mirror plane is also equivalent with a 1/10 rotation (36°) around the 5-fold axis of the 2-fold, **[**010**]** direction. If the rotated/mirrored icosahedron of orientation as in Figure 8 b) is repeated on the expense of the original icosahedron of in Figure 8 a), the OR of the α –phase shown in Figure 7 is justified.

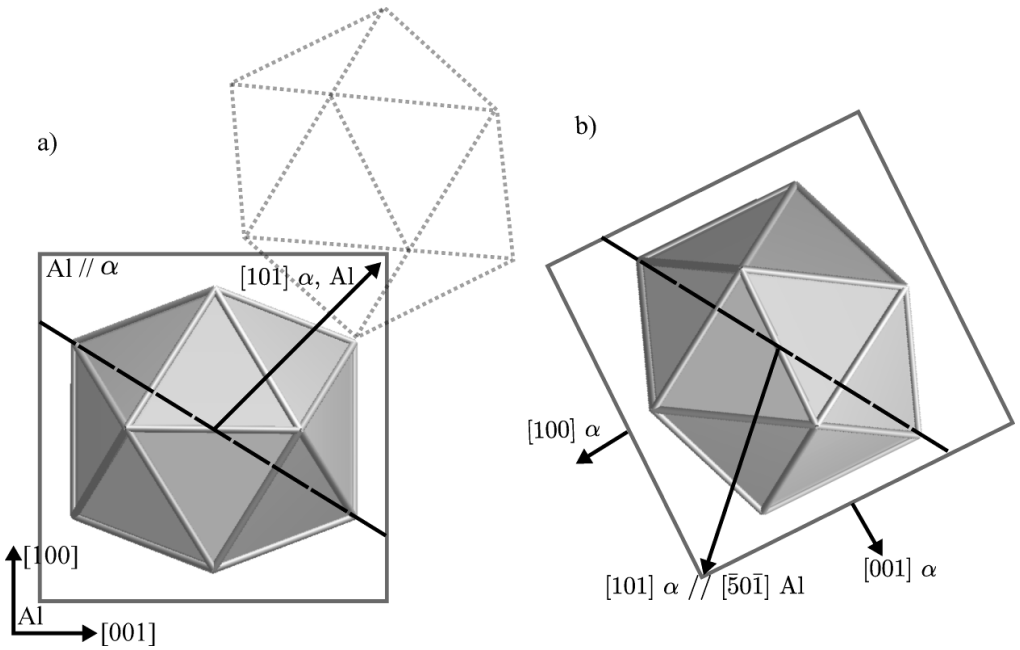

Figure 8 a) 2-fold projection of the icosahedron along the common **[**010**]** α/Al direction. A mirror plane is defined by the 2-fold, common **[**010**]** direction of Al and α, and a 5-fold axis in the paper plane. The mirror plane is illustrated by the stippled lines. b) The resulting icosahedron where the [$\bar{5}0\bar{1}$] Al direction becomes parallel with **[**101**]**α, equivalent with OR in Fig.7 b). The mirroring may be viewed as a 1/10 rotation about the 5-fold axis, bringing another 2-fold axis in the viewing direction.

The mirrored variants of OR2 presented in Figs. 5-8 illustrate how the complexity of the system may be reduced, just by considering a single fixed MI. The explanation therefore appears to be that α is preceded by nuclei or precipitates of the IQC phase, which nearly always will take the orientation in the matrix as given by the MI according to OR1 and OR2. It should be noted that this is a geometrical model for a perfect MI in perfect orientation in the Al matrix. The model does not consider the real icosahedral clusters and respective fit within the aluminum, nor how well the match is for a particular variant of α-phase. Since in principle OR1 and OR2 are identical variants, the commonness of OR1 suggests that the

respective dispersoid will match better with the matrix. This also suggests that under some (local) conditions a mirrored variant may lead to better coherency and growth condition for the α-phase. The heat treatment of the alloys will also likely influence the growth behavior of the dispersoids with respect to orientation. Furthermore, the dependence also on alloy composition has to be considered, and it is therefore possible that optimization can give more or less variants or even a dispersoid distribution of one variant only. Since growth conditions between the variants will be different, such optimizations could also be used to control dispersoid size.

Figure 9 a) shows a BF image of an α-dispersoid after 24 hours annealing at 450°C, in a special orientation relation in 3xxx alloys. The corresponding experimental and simulated diffraction patterns are shown in b) and c) respectively. The OR was found to be **[**100**]** α //**[**111**]** Al, **(**001**)** α //**(**$10\bar{1}$**)** Al. The OR was only observed for one dispersoid, indicating it has a less probability of forming. The third base vector of the α-phase will then be aligned along **[**$1\bar{2}1$**]** Al. None of the three bases of the α-phase fit well with the irrational 2-fold axes as shown in Figure 2 a). The OR can therefore not be described by the current "fixed orientation" icosahedron model since the MI has a fundamentally different orientation. However, this OR has been observed for the icosahedrons in the quasi-crystalline I phase in AlMnSi alloys, shown by Hansen *et al.* (1996). The particular orientation in Figure 9 b) is the most common for the bcc T $Mg_{32}(Al,Zn)_{49}$ phase of the Al-Mg-Zn system, first resolved by Bergman *et al.* (1957). The T-phase is considered as an approximation phase for the IQC in the Al-Mg-Zn system. The respective OR is written **[**100**]** T // **[**111**]** Al, **(**010**)** T //**(**$11\bar{2}$**)** Al, identical with the OR shown for the dispersoid in Figure 9 b) (Totten & MacKenzie, 2003). Note that this is also a common orientation for the IQC in this system, with three orthogonal 2-fold axes along $<111>$, $<110>$, and $<112>$ Al directions (Kubota *et al.* 2005). The T-phase contains about 162 atoms divided among two large molecules of icosahedral symmetry believed to exist also in the corresponding IQC. The space is group Im-3. As with the α-phase, a molecular unit consists of several concentric layers of icosahedra, and also including a dodecahedron and a triacontahedron. There is one fundamental difference between the T-phase and the α-phase. The inner icosahedron of the T-phase contains a central atom, while the α-phase icosahedron is empty. There may be several explanations for the presence of the T-phase like MI orientation. For example, it may be caused by nucleation on impurity elements. However, it could also mean that there exist two or more possible routes for the IQC to form in the matrix, for example given by some symmetry-matching principle, but for this particular system one is much more likely than the other(s). It is also a possibility that the reason could be a more complex growth related phenomenon, for example through twinning or rotation of the MI, not considered further here.

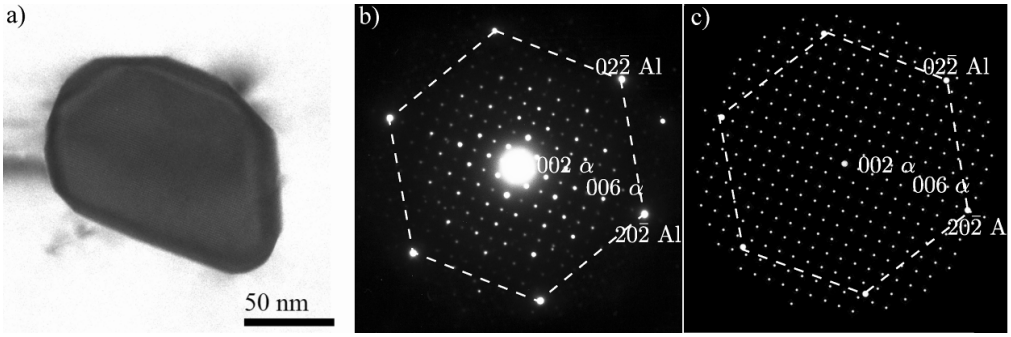

Figure 9 a) Faceted α-Al(Fe,Mn)Si dispersoid. b) Diffraction pattern of the dispersoid, OR $\mathbf{[}100\mathbf{]}\alpha$ //$\mathbf{[}111\mathbf{]}$Al, $\mathbf{(}001\mathbf{)}\alpha$ // $\mathbf{(}10\bar{1}\mathbf{)}$ Al. Reflections $009\,\alpha$ and $20\bar{2}$ Al overlap. c) Corresponding simulation of diffraction pattern. The OR does not correspond to the commonly observed OR1, either not a variant of OR2. This OR does not correspond to MI orientation giving OR1, or the variants of OR2. This OR is normal for the IQC in the Al-Mg-Zn system (Kubota *et al.* 2005), but has been observed also for the IQC phase in AlMnSi alloys (Hansen & Gjønnes 1996).

4. Conclusion

The α-Al(Fe,Mn)Si dispersoids, as an sc icosahedral quasicrystal approximant phase have been studied by TEM in a 3xxx wrought aluminum alloy after low temperature annealing. The orientation of the α-Al(Fe,Mn)Si dispersoids could be explained by assuming that the Mackay icosahedron composing the α-phase has a fixed orientation, similar to that of the IQC existing in aluminum. It is shown that this leads directly to just two generically different orientations in the matrix, described with α unit cell axes of $<\tau\tau^2 1>$ type and <100> type. Although the sets are completely equivalent from the perspective of the icosahedron the first represents the most commonly observed orientation relationship OR1. The second set, with parallel unit cells of Al and α-phase, was not observed at all. For OR1 the basis vectors fall along irrational directions in the aluminum with just one $<111>$ direction common. It can be written $\mathbf{[}1\,\bar{1}\,1\mathbf{]}\alpha$ // $\mathbf{[}1\,\bar{1}\,1\mathbf{]}$Al, $\mathbf{(}5\bar{2}\bar{7}\mathbf{)}\alpha$ // $\mathbf{(}011\mathbf{)}$Al. The remaining experimentally observed orientations, except one, could be related to mirror- variants relative to the icosahedral 3-fold or 5-fold axes of the hypothetical Mackay icosahedron fixed in the Al matrix. The single exception could be linked to the orientation of the Mackay Icosahedron internal to the T-phase of the Al-Mg-Zn system.

Acknowledgements This work has been supported by the KMB project MoReAl financed by The Research Council of Norway, and the industrially partners Hydro and Sapa Technology.

References

Alexander, D. T. L & Greer A. L. (2002). *Acta Mat*. **50**, 2571-2583.
Alexander, D. T. L., Hamerton, R. G., Cama, H. & Geer, A. L. (2002) *Light Met.* **50**, 771-776.
Bergman, G, Waugh, J. L. T. & Pauling, L. (1957). *Acta Cryst*. **10**, 254-258.
Cooper, M. (1967). *Acta cryst*. **23**, 1106-1107.
Cooper, M. & Robinson K. (1966). *Acta Cryst.* **20**, 614-617.
Courbon, J. (2000). *Mat. Sci. Forum.* **17,** 331-337.

Dubois, J. M., Janot, C. & Pannetier, J. (1986). *Phys. Lett. A.* **115**, 177-181.
Elser, V. & Henley, C. L. (1985). *Phys. Rev. Lett.* **55**, 2883-2886.
Fowler, H. A., Mozer, B. & Sims, J. (1988). *Phys. Rev. B.* **37**, 3906-3913.
Furrer, P. (1979) *Z. Material*. **70**, 699-706.
Guyot, G. & Audier, M. (1985). *Phil. Mag.* **52**, L15-L19.
Hansen, V., Anderson, B., Tibbals, J. E. & Gjønnes, J. (1995). *Mater. Trans.* B. **26B**, 839-849.
Hansen, V., Gønnes, J. & Andresson, B. (1989). *J. Mat. Sci. Lett.* **8**, 823-826.
Hansen, V. & Gjønnes, J. (1996) *Phil. Mag. A.* **73**, 1147-1158.
Hansen, V. & Gjønnes, J. (1996). *Acta Cryst*. **52**, 125-132.
Hausch, G., Furrer, P. & Warlimont, H. (1978). *Z Materialkunde*. **69**, 174-180.
Humphreys, F. J. (1977). *Acta Metal.* **25**, 1323-1344.
Hutchinson, W. B., Oscarsson, A. & Karlson, Å. (1989) *Mat. Sci. and Tech.* **5**, 1118-1127.
de Haan, P. C. M., van Rijkom, J. & Söntgerath, J. A. H. (1996) *Mat. Sci. Forum.* **217-222**, 765-770.
Jarić, M. V. & Gratias, D. (1989). *Extended Icosahedral Structures*. Vol 3. pp. 2-34. San Diego: Academic Press.
Koskenmaki, D. C., Chen, H. S. & Rao, K. V. (1986) *Phys. Rev. B.* **33**, 5328-3536
Kubota, M., Nie, J. F. & Muddle, B. C. (2005). *Mat. Trans.* **46**, 365-368.
Kuo, K. H & Deng, D. W. (2002). *J. Alloys Comp*. **342**, 174-179.
Li, Y. J & Arnberg, L. (2003) *Light Met*. 991-997.
Li, Y.J & Arnberg, L. (2003). *Acta Mat.* **51**, 3415-3428.
Li, Y. J, Muggerud, A. M. F., Olsen, A. & Furu, T. (2012) *Acta Mat.* **60**, 1004-1014.
Mackay, A. L. (1962). *Acta Cryst*. **15**, 916-918.
Merchant, H. D, Morris, J.G. & Hodgson, D. S. (1990). *Mat Charact*. **25**, 339-373.
Mondolfo, L.F. (1976).
Muggerud, A. M. F., Mørtsell, E. A., Li, Y. J. & Holmestad, R. (2013) *Mat. Sci. Eng. A.* **567**, 21-28.
Muggerud, A. M. F., Li, Y. J. & Holmestad, R. (2014). *Phil. Mag.* **94**, 556-568.
Nes, E. (1976). *Acta Metal.* **24**, 391-398.
Pannetier, J., Dubois, J. M., Janot, C. & Bilde, A. (1987). *Phil. Mag. B.* **55**, 435-457
Stern, E. A., Ma, Y. (1987). *Phil. Mag. Lett.* **56**, 103-108.
Sugiyama, K., Kaji, B. N. & Hiraga, K. (1998). *Acta Cryst*. **C54**, 445-447.
Suni, J. P, Doherty, R. D., Hollinshead, P. A., Rouns, T.N. & Shuey, R. T. (1998). *Al Alloys.* **2**, 1203-1208.
Tibballs, J. E., Davis, R. L. & Parker, B. A. (1989). *J. of Mat. Sci*. **24**, 2177-2182.
Tibballs, J. E., Horst, J. A. & Simensen, C. J. (2001). *J. of Mat. Sci.* **36,** 937-941.
Totten, G.E & MacKenzie, D. S. (2003) *Handbook of Aluminum. Physical metallurgy and Processes.* Vol. 1. pp. 284-289. New York: CRC Press.
Williams, D. B. & Carter, B.C. (2009). *Transmission Electron Microscopy.* Springer Science.

Paper IV

Combining HAADF STEM tomography and electron diffraction for studies of α-Al(Fe,Mn)Si dispersoids in 3xxx aluminium alloys

Submitted to Philosophical Magazine

Philosophical Magazine
Vol. 00, No. 00, 00 Month 200x, 1–13

RESEARCH ARTICLE

Combining HAADF STEM tomography and electron diffraction for studies of α-Al(Fe,Mn)Si dispersoids in 3xxx aluminium alloys

Astrid Marie F. Muggerud[a*], John C. Walmsley[a,b], Randi Holmestad[a] and Yanjun Li[c]

[a]*Department of Physics, Norwegian University of Science and Technology, NTNU, N-7491 Trondheim, Norway*; [b]*SINTEF Materials and Chemistry, N-7465 Trondheim, Norway*; [c]*Department of Materials Science and Engineering, Norwegian University of Science and Technology, NTNU, N-7491 Trondheim, Norway*

(*Received 00 Month 200x; final version received 00 Month 200x*)

A new methodology to study the precipitation crystallography of dispersoids in Al matrix is proposed. By combining the High Angle Annular Dark Field Tomography and the electron diffraction studies, the 3D-morphology, orientation relationship with Al matrix and habit planes of the dispersoids can be achieved simultaneously. This approach has been applied to investigate the α-Al(Mn,Fe)Si dispersoids precipitated in an AA3xxx alloy.

Most dispersoids have a plate shaped morphology after low temperature homogenisation at 450 °C. The largest proportion of the dispersoids follows the previously described orientation relationship with the Al matrix $\langle 1\bar{1}1\rangle_{\mathrm{Al}}//\langle 1\bar{1}1\rangle_{\alpha}, \{011\}_{\mathrm{Al}}//\{5\bar{2}\bar{7}\}_{\alpha}$. Two plate shaped dispersoids have been studied in detail. The dispersoid following the commonly observed orientation had habit planes $(\bar{1}11)_{\mathrm{Al}}//(2\bar{5}0)_{\alpha}$. The dispersoid not following the commonly observed orientation relationship had habit planes $(40\bar{2})_{\mathrm{Al}}//(13\bar{2})_{\alpha}$, with orientation relationship $[010]_{\mathrm{Al}}//[425]_{\alpha}$, $(40\bar{2})_{\mathrm{Al}}//(13\bar{2})_{\alpha}$.

Keywords: aluminium alloys; electron diffraction; tomography; orientation relationship

1. Introduction

Two main types of dispersoids, orthorhombic Al_6(Fe,Mn) and cubic α-Al(Fe,Mn)Si, precipitate during homogenisation of non-heat treatable commercial 3xxx Al alloys with main alloying elements Si, Fe and Mn. In alloys with low Si content, α-Al(Fe,Mn)Si dispersoids precipitate at low temperatures and dissolve during heating. Al_6(Fe,Mn) dispersoids will precipitate as the stable phase [1]. Increased Si content in the alloys leads to precipitation of cubic α-Al(Fe,Mn)Si dispersoids as the stable phase. For high Si content, Al_6(Fe,Mn) dispersoids will not precipitate in the alloy [1–5].

The crystal structure of the α-Al(Fe,Mn)Si dispersoid is complex, with 138 atoms in the unit cell. The crystal structures of the α-AlMnSi and α-AlFeSi phases were described by Cooper et al. [6, 7]. The α(AlMnSi) phase is of simple cubic (sc) structure with space group $Pm\bar{3}$, while the α(AlFeSi) phase is body centered cubic (bcc) with space group $Im\bar{3}$. A high Fe/Mn ratio in the alloy favors the bcc $Im\bar{3}$ structure, while low Fe/Mn ratios favor the sc $Pm\bar{3}$ [8]. The α(AlMnSi) structure is built up by two slightly different Mackay icosahedron at positions 000 and $\frac{1}{2}\frac{1}{2}\frac{1}{2}$ [9,

*Corresponding author. Email: astrid.muggerud@ntnu.no

ISSN: 1478-6435 print/ISSN 1478-6443 online

DOI: 10.1080/14786435.20xx.xxxxxx
http://www.informaworld.com

10]. The α-Al(Fe,Mn)Si dispersoid phase may transform from the quasi crystalline icosahedral I phase, and is therefore a so-called quasi crystal approximate [11–16].

The type, size, number density and distribution of dispersoids have a strong influence on the mechanical properties and recrystallisation behavior of the 3xxx Al alloys [4, 11, 17–23]. Recent studies show that a remarkable hardening effect from α-Al(Fe,Mn)Si dispersoids in 3xxx Al alloys can be achieved by a low temperature annealing [21, 22].

Diffraction studies of α-Al(Fe,Mn)Si dispersoids have shown various possible orientation relationships (ORs) between the dispersoid and Al matrix [8, 11, 12]. Recent studies by Li et al. of an AA3003 Al alloy [1, 21], show partial coherence exists between the α-Al(Fe,Mn)Si dispersoids and the Al matrix. According to Li et al. [21] most of the α-Al(Fe,Mn)Si dispersoids follow a commonly observed OR, described as $\langle 1\bar{1}1\rangle_{\alpha}//\langle 1\bar{1}1\rangle_{\mathrm{Al}}$, $\{5\bar{2}\bar{7}\}_{\alpha}//\{011\}_{\mathrm{Al}}$.

Conventional Transmission Electron Microscopy (TEM) techniques only provide two dimensional (2D) projections of a three dimensional (3D) structure. TEM tomography is therefore a powerful technique in order to reveal and visualize the true 3D morphology of the dispersoid in the nano meter range. To be able to reconstruct a tomography series, the detected signal must be monotonically related to a physical property through the structure. This is known as the projection requirement [24]. In crystalline materials mass thickness and diffraction contrast dominate the bright field (BF) signal. Therefore BF TEM is less suited for tomography on crystalline samples. High angle, Rutherford scattered incoherent electrons are detected by a high angle annular dark field (HAADF) STEM detector, which collects electrons scattered to high angles [24, 25]. The HAADF signal changes monotonically with atomic number Z, approximately proportional to Z^2, and the thickness of the sample. Therefore the HAADF signal is very well suited for tomography studies of crystalline materials, and diffraction contrast is suppressed.

HAADF STEM tomography has been applied on various crystalline materials, such as catalyst particles and biological samples [26, 27]. Some HAADF STEM tomography studies of precipitates in Al alloys have been performed. Kaneko et al. have studied Ge precipitates in an Al alloy [28, 29] and Feng et al. looked at S-precipitates in Al-Cu-Mg alloys [30]. In another metallurgical application Sato et al. studied hexagonal α martesite in a Ti-Al alloy [31].

In the present work α-Al(Fe,Mn)Si dispersoids have been investigated by HAADF STEM tomography in order to reveal their full morphology. The tomography study is combined with electron diffraction studies in order to describe the ORs and habit planes of the dispersoids. By combining the tomography and electron diffraction, it is possible to determine the 3D morphology and habit planes of the structures and couple this information to the orientation relationship with the surrounding Al matrix. To combine the methods provides a more throughout picture of the dispersoid orientation, morphology and habit planes in the Al alloy.

2. Experimental

2.1. *Material and equipment*

Samples were taken from a DC-cast aluminium billet produced by Hydro Aluminium. Mass spectroscopy measurements of the chemical composition of the alloy gave a content of 0.50 wt% Fe, 0.99 wt% Mn and 0.48 wt% Si. Traces of Cu, Mg, Zn, Cr, Ni, Pb and Sn in concentrations less than 0.01 wt% were also detected.

The samples were heated in an air circulating furnace from room temperature, with a heating rate of 50 K/h, up to a homogenisation temperature of 450 °C and

held for 24 hours before water quenching.

TEM foils were thinned by electro polishing using a Struers TenuPol-5 electro polishing unit, in an electrolyte containing two parts methanol and one part of nitric acid at -20 °C.

A Jeol 2010F FEG TEM operating at 200 kV was used for HAADF STEM tomography acquisition and parts of the electron diffraction work. A camera length of 15 cm, corresponding to a collection angle between 50 and 125 mrad, was used. A Jeol single tilt holder with a dedicated tomography tip insert was used in order to achieve high tilt angles in the microscope. A Phillips CM30 TEM operating at 150 kV was used for most of the electron diffraction and bright field TEM imaging.

2.2. *Experimental procedure and processing of data*

In this work the HAADF STEM signal was applied for the tomography to reveal the true morphology of α-Al(Fe,Mn)Si dispersoids. In order to obtain a high quality tilt-series, the area for investigation was carefully selected. The area chosen for HAADF STEM was tilted to high angles to check the attainable tilt range. The thickness of the selected sample area is also crucial. It is important that the area thickness is large enough so that the whole dispersoid volume are embedded within the selected volume. In too thin areas of the sample, the dispersoid edges may have been cut, and a reconstruction of the full morphology will not be possible. However, in the thicker areas of the sample the electron diffraction patterns becomes more complex and harder to index. While the resolution parallel to the tilt axis is equal to the original resolution, the resolution in the other perpendicular directions is dependent on the number of acquired projections and the diameter of the reconstructed area. The resolution in the direction parallel to the optical axis will be degraded by an elongation factor related to the maximum tilt angle. There is a missing wedge of information, resulting in a blurring in the reconstruction [24].

A tomography plug-in in Digital Micrograph was used to assist acquiring the tilt-series. Tilt, position tracking and focusing were performed automatically by the software. In addition, positioning and focusing were monitored and adjusted manually when needed. The area was tilted with 2° tilt steps from -76° to +76° around the tilt axis. The tilt axis is indicated by the stippled line in the STEM micrograph in Figure 1 (b), defined as the y-axis.

The acquired imaging data was processed using the ImageJ software with the TomoJ plug in [32, 33]. Micrographs containing strong diffraction contrast were removed from the tilt-series. The micrographs in the tilt-series were aligned with help of the landmark menu [34]. The direction of the tilt axis was calibrated according to the tilt-series. The aligned tilt-series was reconstructed by the weighted back projection (WBP) algorithm. Manual segmentation in Avizo 7.1 was used to visualise the dispersoids.

Selected area electron diffraction was performed on the same dispersoids as shown in the tomography series, to couple 3D morphology of the visualized dispersoids to the crystallographic orientation of the dispersoids in the matrix. The dispersoids were also tilted to an edge-on view in order to determine the habit planes. The possibility to tilt the dispersoids to an edge-on view depends on the dispersoid orientation related to the tilt range of the microscope. A complete and consistent description of the OR requires diffraction from various zone axes for verification of the OR. This is a strong restriction, because two relatively low indexed zone axes may not be reachable experimentally within the tilt range.

In order to be able to tilt around two independent axes the sample was moved to a double tilt holder from the single tilt dedicated tomography holder. The dispersoids

from the tomography series were tilted one by one to an aluminium zone axis, and the corresponding zone axis of the dispersoids were also recorded. A very important point is to keep track of tilting angles and directions in order to relate the directions from the diffraction patterns to the 3D directions in the reconstruction of the dispersoids. As the sample is moved to another holder the sample will also be rotated, and the tilt axes in the double tilt holder will not be in the same direction as the tilt axis of the tomography holder. Therefore, care was taken to correct for the rotation of the sample when moving between sample holders. The tilt axes and tilt directions to obtain the zone axis of Al and the dispersoids in the double tilt holder were related to the direction of the reconstructed dispersoids in the tomography series. This provides the correspondence between the orientation of the matrix and the dispersoids to the 3D visualisation of the dispersoids.

3. Results and discussion

3.1. *HAADF STEM Tomography, reconstruction and visualisation of α-Al(Fe,Mn)Si dispersoids*

Figure 1 (a) shows a HAADF STEM micrograph of α-Al(Fe,Mn)Si dispersoids distributed in the aluminum matrix. The dispersoid size varies from ∼20 nm to ∼300 nm. As can be seen, there is a tendency for small dispersoids to have a cube morphology. The larger dispersoids generally show a rod or plate shaped morphology. Figure 1 (b) shows a HAADF STEM micrograph of the dispersoids in the area outlined in (a). Figure 1 (c) shows a corresponding BF TEM micrograph to illustrate that the atomic number Z dependent HAADF STEM micrograph in (b) is more suited for tomography acquisitions. The direction of the tilt axis is stippled in Figure 1 (b). The tilt axis corresponds to the y- direction of the tomography series. The dispersoids investigated further are marked 1-4 for easy recognition.

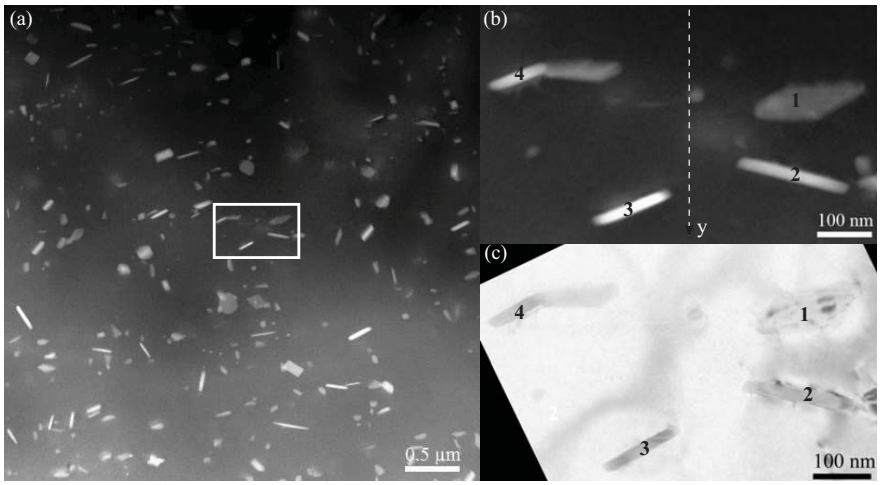

Figure 1. HAADF STEM micrographs showing (a) distribution of α-Al(Fe,Mn)Si dispersoids in Al matrix. (b) Enlargement of the box in (a) showing selected dispersoids. The stippled line corresponds to the tilt axis, defined as the y-axis in the tilt-series. (c) Corresponding BF TEM micrograph for comparison of contrast mechanisms.

HAADF STEM tomography micrographs at tilt angles of 30°, 54°,-2° and -40° contained strong diffraction contrast and were not used in the reconstruction. Figure 2 shows selected micrographs from the recorded tomography tilt-series. The

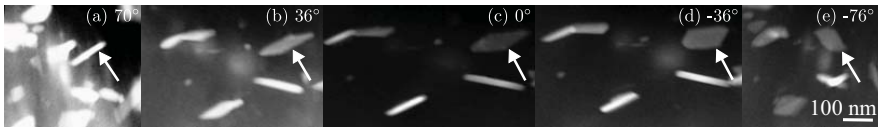

Figure 2. HAADF STEM tomography micrographs from tilt-series at (a) 70°, (b) 36°, (c) 0°, (d) -36° and (e) -76° tilt angle. The arrow pints to dispersoid 1 in Figure 1 (b) and (c).

dispersoids 1-4 from Figure 1 are shown in Figure 2 at (a) 70°, (b) 36°, (c) 0°, (d) -36° and (e) -76° tilting angles. The tilt-serie in Figure 2 illustrates the limitation of 2D projections for describing true 3D morphology. The apparent projected morphology of the dispersoids is depending on the sample orientation. For example, a plate shaped dispersoid can show rod-like morphology when viewed edge-on. Rod like precipitates in Figure 1 have a true plate shaped morphology in 3D, while the smaller irregular dispersoids viewed in projection most likely are cubes. The dispersoid growth from cube morphology to plate like morphology is because different facets of the dispersoids have different interfacial energy in relation to Al matrix.

After aqusition and reconstruction of the tilt-series, the dispersoids were visualised by segmentation. 3D morphology of the disperoids is shown in Figure 3. The dispersoids are viewed along the z-axis, perpendicular to the plane view of the TEM foil, corresponding to the untilted view in the original TEM data, as in Figure 1. The y-axis is still the tilt axis from the tomography series.

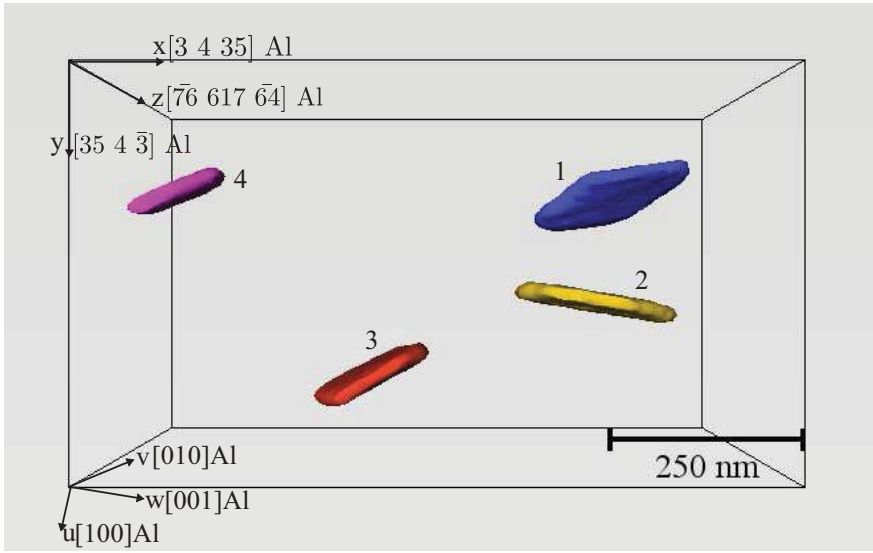

Figure 3. 3D visualisation of the reconstructed dispersoids viewed in the z- direction of the tomography series, close to the v [010] Al zone axes direction. The directions in Al are found from diffraction. The indices of the x, y and z axis in the Al coordinate system are given in the upper left corner. The dispersoids are marked 1-4 corresponding to Figure 1 (c). See the supplementary 'Movie I' for a full dynamical view of the reconstructed dispersoids .

The crystallographic directions of the Al matrix are shown in the lower left corner of the figure, named u, v and w. These directions are found from the diffraction study of the Al matrix. 3° and 6° tilt around the two axes of the double tilt holder was needed to reach the [010] Al zone axis. From these tilt angles the directions u, v and w in the Al matrix can be related to the x, y and z axes from the tomography series. The corresponding indexes for the x, y and z axes from the tomography series in the Al matrix are given in the upper left corner in the figure. As described

in Section 2.2, the tilt axes of the double tilt holder are in other directions than the x, y and z axes from the tomography series due to rotation of the sample when changing holder, and different tilt axis geometry of the two holders.

All the four dispersoids have a plate shaped morphology. For a full dynamical view of the reconstructed dispersoids, see 'Movie I'. The movie also shows the orthogonal slices of the weighted back projection reconstruction through the dispersoids, for inspection and quality assurance of the reconstruction.

As described in the introduction, the resolution parallel to the tilt axis, in this case the y-axis, equals the resolution of the projections. The large planar facets are therefore better resolved for dispersoids 2, 3 and 4 than for dispersoid 1, as the projection of the dispersoids are close to an edge-on view with respect to the tilt axis. This also made the segmentation procedure of dispersoid 2-4 easier than for disperoid 1, and the large facets of dispersoid 1 appears more noisy.

3.2. *Orientation relationship studies of dispersoids from the tomography series*

The α-Al(Fe,Mn)Si dispersoids in 3xxx alloys were found to follow a common OR described by Li et al. [21] as $\langle 1\bar{1}1\rangle_{\mathrm{Al}}//\langle 1\bar{1}1\rangle_{\alpha}$, $\{011\}_{\mathrm{Al}}//\{5\bar{2}\bar{7}\}_{\alpha}$. Selected area electron diffraction provided information about the Al matrix orientation for the four dispersoids in Figure 3. Since the diffraction patterns of dispersoid 3 and 4 were impossible to index due to reflection of higher ordered Laue zones, double diffractions and too low intensity of the diffraction spots from the dispersoid phase, only orientation relationships of dispersoid 1 and 2 with the Al matrix were determined.

3.2.1. Dispersoid 1

Figure 4 shows micrographs of dispersoid 1 with corresponding diffraction patterns along three relatively low index Al zone axes. Double diffractions and reflection of higher order Laue zones complicate the indexing. In Figure 4 (a) and (b) the OR of disperoid 1 is found to be $[010]_{\mathrm{Al}}//[8\bar{3}5]_{\alpha}$, $(002)_{\mathrm{Al}}//(2\bar{3}\bar{5})_{\alpha}$, as given in Table 1.

In Figure 4 (c) and (d) dispersoid 1 is tilted and oriented approximately along $[130]_{\mathrm{Al}}//[502]_{\alpha}$, $(002)_{\mathrm{Al}}//(2\bar{3}\bar{5})_{\alpha}$. The physical tilt at the microscope between the two diffraction patterns in (b) and (d) was 18°. This matches well with the theoretically calculated angle between $[010]_{\mathrm{Al}}$ and $[130]_{\mathrm{Al}}$, which is 18°, and the corresponding angle between $[8\bar{3}5]_{\alpha}$ and $[50\bar{2}]_{\alpha}$ of 20°.

In Figure 4 (e) and (f) dispersoid 1 is viewed edge-on. The OR is found to be approximately $[12\bar{1}]_{\mathrm{Al}}//[524]_{\alpha}$, $(\bar{1}11)_{\mathrm{Al}}//(2\bar{5}0)_{\alpha}$. The physical tilting angle from the diffraction pattern in (b) to the diffraction pattern in (f) at the microscope was 35°, in perfect correspondence to the angle between the aluminium zone axis $[010]_{\mathrm{Al}}$ and $[12\bar{1}]_{\mathrm{Al}}$, and the angle between $[8\bar{3}5]_{\alpha}$ and $[524]_{\alpha}$, which both also are 35°. Table 1 summaries the OR along the three Al zones in Figure 4.

Table 1. ORs of dispersoid 1 in Figure 4.

Figure 4	OR
(a), (b)	$[010]_{\mathrm{Al}}//[8\bar{3}5]_{\alpha}$, $(002)_{\mathrm{Al}}//(2\bar{3}\bar{5})_{\alpha}$
(c), (d)	$[130]_{\mathrm{Al}}//[502]_{\alpha}$, $(002)_{\mathrm{Al}}//(2\bar{3}\bar{5})_{\alpha}$
(e), (f)	$[12\bar{1}]_{\mathrm{Al}}//[524]_{\alpha}$, $(\bar{1}11)_{\mathrm{Al}}//(2\bar{5}0)_{\alpha}$

The OR found from Figure 4 (b) was used as an input for a transformation matrix R_1 for dispersoid 1, presented in Table 2. The transformation matrix provides

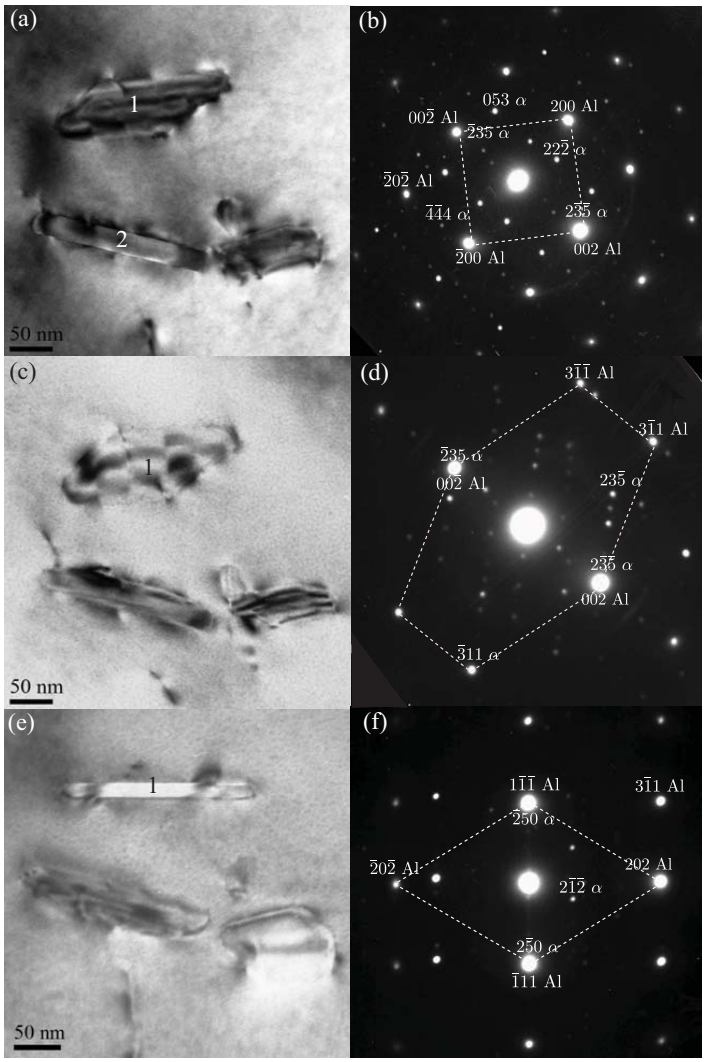

Figure 4. α- dispersoid 1 viewed from 3 zone axes of Al matrix orientations in BF TEM and the corresponding diffraction patterns of dispersoid 1 and Al matrix. The dispersoid 1 is viewed edge-on in (e).

Table 2. OR of dispersoid 1 in Figure 4 (a) and (b) and calculated transformation matrix.

Dispersoid	OR	Transformation matrix
1	$[010]_{\mathrm{Al}}//[8\bar{3}\bar{5}]_{\alpha}$, $(002)_{\mathrm{Al}}//(2\bar{3}\bar{5})_{\alpha}$	$R_1 = \begin{bmatrix} 0.1570 & 0.2581 & 0.1036 \\ 0.2617 & 0.0968 & -0.1554 \\ -0.0942 & 0.1613 & -0.2591 \end{bmatrix}$

parallel directions in the two systems. The transformation matrix was used to aid the indexing of the experimental diffraction patterns from various zone orientations consistently. The matrix were also used to verify ORs which were equivalent to the previous determined OR by Li et al. [21]. The diffraction studies show that dispersoid 1 follows the commonly observed orientation system.

Figure 5 shows plane on view of the reconstructed dispersoid 1 in (a), and in (b)

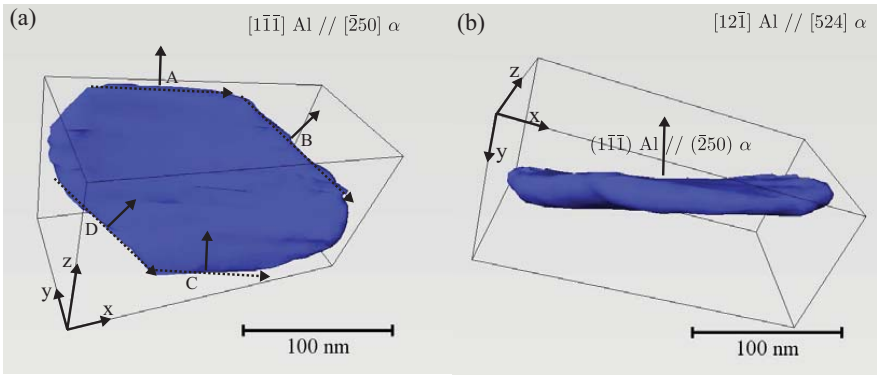

Figure 5. Visualisation of dispersoid 1. (a) Dispersoid 1 perpendicular to the large facet. The stippled side edges are indexed for both Al and dispersoid. (b) The dispersoid viewed along $[12\bar{1}]_{\mathrm{Al}}//[524]_{\alpha}$, as in Figure 4 (e). Habit plane pair $(\bar{1}11)_{\mathrm{Al}}//(2\bar{5}0)_{\alpha}$ is indicated.

Table 3. Trace directions and possible facet planes of dispersoid 1, side edges A-D in Figure 5.

Facets	Trace directions	Possible facet planes
A, C	$[\bar{1}1\bar{2}]_{\mathrm{Al}}//[001]_{\alpha}$	$(110)_{\mathrm{Al}}//(\bar{5}20)_{\alpha}$
B, D	$[\bar{5}\bar{1}\bar{4}]_{\mathrm{Al}}//[\bar{5}26]_{\alpha}$	$(13\bar{2})_{\mathrm{Al}}//(525)_{\alpha}$

edge-on view along $[12\bar{1}]_{\mathrm{Al}}//[524]_{\alpha}$, as in Figure 4 (e). The habit plane identified by the diffraction study presented in Figure 4 (e) and (f) for dispersoid 1 is indicated in Figure 5 (b), $(\bar{1}11)_{\mathrm{Al}}//(2\bar{5}0)_{\alpha}$. The large facets of dispersoid 1 appears a bit noisy. The resolution in the direction parallel to the optical axis (z-direction) will be degraded by an elongation factor related to the maximum tilt angle. In addition the segmentation of dispersoid 1 was more challenging due to the orientation of dispersoid 1 in the reconstructed volume.

The large facet of dispersoid 1, as illustrated in Figure 5 (a) is the habit plane $(\bar{1}11)_{\mathrm{Al}}//(2\bar{5}0)_{\alpha}$. The diffraction patterns along the habit plane directions were simulated. The side edges of the dispersoids are likely perpendicular to the habit plane, and this assumption was used to find the possible facet planes of the side edges in both phases, indicated by the solid arrows in Figure 5 (a). By determining the trace directions of the facets of the dispersoids, indicated by the stippled arrows in Figure 5 (a), the crystallographic planes of the facets could be determined. The side edges are named A-D in Figure 5 (a), indexed in Table 3 for both dispersoid and Al. Side edges A and C are parallel, and also B and D. The transformation matrix in Table 2 was used to verify that the indexing of the two systems was consistent with each other. By combining tomography and diffraction it is possible to obtain information about the orientation of the dispersoid edges.

The possible facet planes for Al are directed in relatively low index directions. For the α phase the possible facets have higher indexes. For both the possible faces and the trace directions there is an uncertainty in the directions with some degrees due to the unsharpness of the side edges. When comparing with the tomography tilt-series a more flat facet and clean edge structure is apparent, as can be seen in Figure 2 (b)-(d). In the direction of the side edges the reconstruction of dispersoid 1 is irregular and the segmentation is therefore less smooth along these side edges. The overall morphology of the side edges of the dispersoid can be established, although fine details and some curvatures are likely to have been introduced as artifacts in the reconstruction to visualisation.

3.2.2. Dispersoid 2

Figure 6 shows the micrographs and corresponding selected area diffraction patterns of dispersoid 2. In Figure 6 (a) and (b) dispersoid 2 is taken along $[111]_\alpha$. The corresponding zone axis of the Al matrix is deviating 1.5° from the $[14\bar{1}]_{\mathrm{Al}}$ zone axis. A high resolution insert of the dispersoid is shown in the upper right corner of Figure 6 (a).

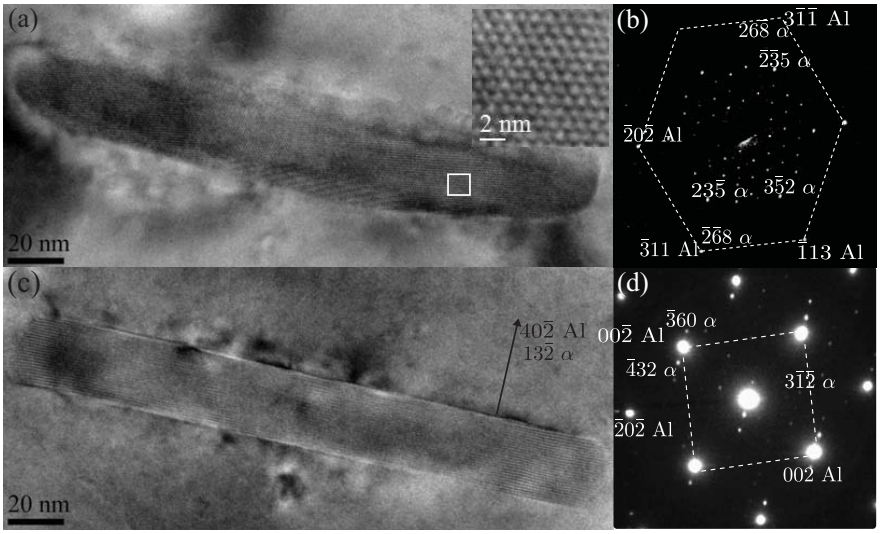

Figure 6. Dispersoid 2 viewed along two zone axes directions, with corresponding diffraction patterns. (a) and (b) Dispersoid along $[111]_\alpha//[14\bar{1}]_{\mathrm{Al}}$. (c) and (d) Edge-on view of dispersoid 2 along $[010]_{\mathrm{Al}}//[425]_\alpha$.

Different from dispersoid 1, the experimentally determined OR of dispersoid 2 does not follow the commonly observed OR. The OR in Figure 6 (a) and (b), listed in Table 5, was used to calculate a transformation matrix R_2, presented in Table 4. As the OR in Figure 6 (b) has a deviation angle of 1.5°, the accuracy of this transformation matrix seems to be lower than for the transformation matrix R_1 in Table 2 of the commonly observed OR of dispersoid 1, as the zone axes are not exactly parallel.

Table 4. OR of dispersoid 2 in Figure 6 (a) and (b) and calculated transformation matrix.

Dispersoid	OR	Transformation matrix
2	$[14\bar{1}]_{\mathrm{Al}}//[111]_\alpha$, $(3\bar{1}\bar{1})_{\mathrm{Al}}//(26\bar{8})_\alpha$	$R_2 = \begin{bmatrix} 0.1901 & 0.1910 & 0.1715 \\ 0.1492 & 0.0915 & -0.2672 \\ -0.2089 & 0.2391 & -0.0347 \end{bmatrix}$

In Figure 6 (c) and (d) dispersoid 2 is tilted to an edge-on view along $[010]_{\mathrm{Al}}$. The zone axes of dispersoid 2 were hard to index due to double diffraction. Applying the transformation matrix for dispersoid 2 in Table 4 with $[010]_{\mathrm{Al}}$ as input, an exact zone axis of $[0.1910\ 0.0915\ 0.2391]_\alpha$ is found. This gives an approximate OR of $[010]_{\mathrm{Al}}//[425]_\alpha$, with habit planes in $(40\bar{2})_{\mathrm{Al}}//(13\bar{2})_\alpha$ directions. The tilt between $[1\bar{1}1]_\alpha$ and $[425]_\alpha$ is 19°, and between $[14\bar{1}]_{\mathrm{Al}}$ and $[010]_{\mathrm{Al}}$ 19.5°. The theoretical angles between the directions are in good agreement with the physical tilt angle at the microscope of 20°. The transformation matrix was useful in order

to propose reasonable zone axes for the α phase. The ORs shown in Figure 6 are summarised in Table 5.

Table 5. ORs of dispersoid 2 in Figure 6.

Figure 6	OR
(a), (b)	$[14\bar{1}]_{\mathrm{Al}}//[111]_{\alpha}$, $(3\bar{1}\bar{1})_{\mathrm{Al}}//(26\bar{8})_{\alpha}$
(c), (d)	$[010]_{\mathrm{Al}}//[425]_{\alpha}$, $(40\bar{2})_{\mathrm{Al}}//(13\bar{2})_{\alpha}$

Figure 7 (a) shows the reconstruction of dispersoid 2 perpendicular to the large facet. The plate shaped morphology of dispersoid 2 is apparent. Figure 7 (b) shows the dispersoid along $[010]_{\mathrm{Al}}//[425]_{\alpha}$, with the habit plane $(40\bar{2})_{\mathrm{Al}}//(13\bar{2})_{\alpha}$, in correspondence with Figure 6 (c) and (d). In Figure 7 (a) the trace directions are indicated with stippled arrows and possible facet planes with solid arrows for the side edges named A-F. Side edge A and D, B and E, and also C and F are parallel. The resulting indices are summarised in Table 6. The same procedure as described for dispersoid 1 was used to find the directions of possible facet planes and trace directions.

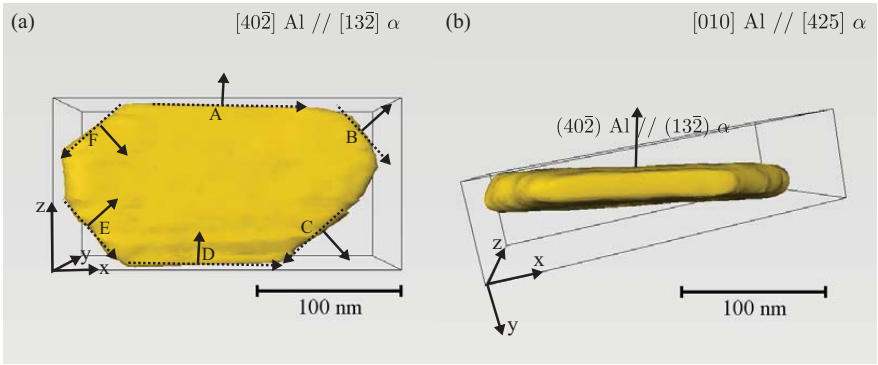

Figure 7. Visualisation of dispersoid 2. (a) Dispersoid 2 perpendicular to the large facet plane. Stippled arrows shows trace directions and solid arrows possible facet normals. (b) The dispersoid viewed along $[010]_{\mathrm{Al}}//[425]_{\alpha}$, as in Figure 6 (c). The habit plane pair $(40\bar{2})_{\mathrm{Al}}//(13\bar{2})_{\alpha}$ is indicated.

Table 6. Trace directions and possible facet planes of dispersoid 2, side edges A-F in Figure 7.

Facet	Trace direction	Possible facet normal
A, D	$[\bar{1}0\bar{2}]_{\mathrm{Al}}//[\bar{6}43]_{\alpha}$	$(010)_{\mathrm{Al}}//(425)_{\alpha}$
B, E	$[\bar{2}\bar{5}\bar{4}]_{\mathrm{Al}}//[\bar{9}1\bar{3}]_{\alpha}$	$(\bar{1}2\bar{2})_{\mathrm{Al}}//(\bar{1}34)_{\alpha}$
C, F	$[2\bar{5}4]_{\mathrm{Al}}//[\bar{1}\ 11\ \bar{1}6]_{\alpha}$	$(\bar{1}\bar{2}\bar{2})_{\mathrm{Al}}//(\bar{5}1\bar{1})_{\alpha}$

The possible facet planes for Al are directed in low index directions. For the α phase the possible facet planes have higher indexes. The reconstructed image of dispersoid 2 is less noisy than dispersoid 1, for the large facets. This is again related to how the dispersoid is oriented relative to the tilt axis (y-axis). The resolution parallel to the tilt axis is equal to the original resolution. Although there is less noise in the directions of the large facets, also here there are some degrees uncertainty in possible facet planes and trace directions due to noise on the side edges. Facet planes A and D have a larger certainty than B, E, C and F. The curvature of these facets are likely introduced during reconstruction and visualisation.

Dispersoid 3 and 4

Figure 8 shows the reconstructed dispersoids 3 and 4 from Figure 3. In Figure 8 (a) and (c) the viewing direction is perpendicular to the habit planes of the dispersoids. These two dispersoid also have a plate shaped morphology. In Figure 8 (b) and (d) the dispersoids are viewed edge-on with the large facets in the horisontal direction. For both dispersoid 3 and 4, the habit planes in Al have been determined as $(20\bar{4})_{\mathrm{Al}}$. The habit planes for dispersoid 3 and 4 were not determined for the α-phase due to lacking diffraction data of the dispersoids.

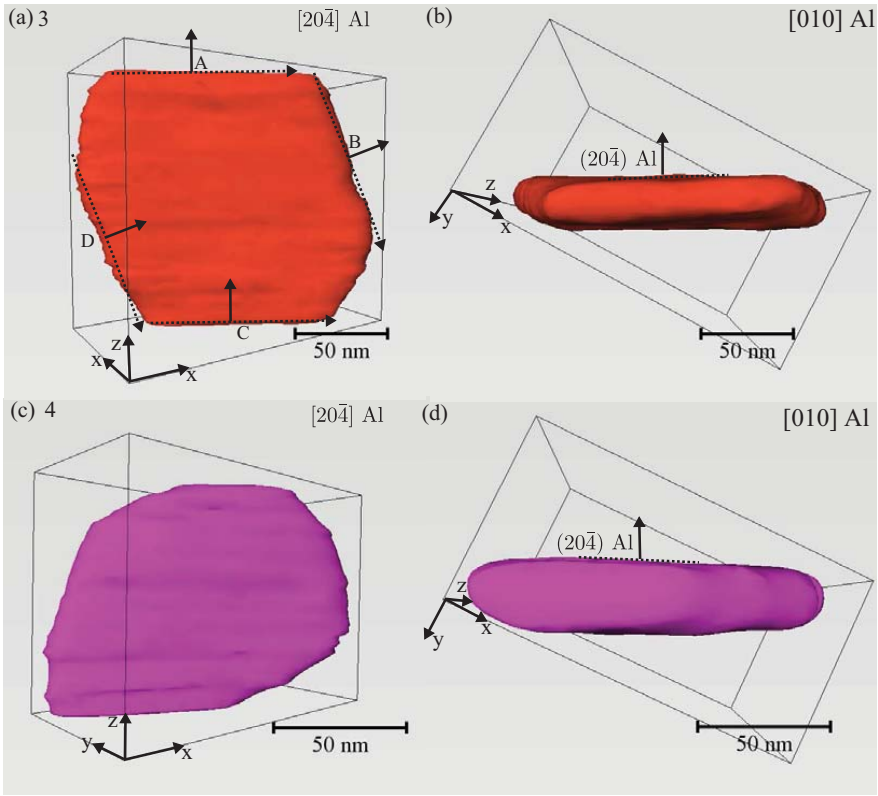

Figure 8. Visualisations of dispersoid 3 and 4. (a) Dispersoid 3 perpendicular to the large facet plane. Stippled arrows shows trace directions and solid arrows possible facet normals. (b) Dispersoid 3 viewed edge-on along $[010]_{\mathrm{Al}}$, with habit plane $(20\bar{4})_{\mathrm{Al}}$. (c) Dispersoid 4 along the large facet plane direction. (d) Dispersoid 4 viewed edge-on along $[010]_{\mathrm{Al}}$, with habit plane $(20\bar{4})_{\mathrm{Al}}$.

Table 7. Trace directions and possible facet planes of dispersoid 3, side edges A-D in Figure 8.

Facet	Trace direction	Possible facet plane
A, C	$[\bar{4}02]_{\mathrm{Al}}$	$(020)_{\mathrm{Al}}$
B, D	$[\bar{2}5\bar{1}]_{\mathrm{Al}}$	$(\bar{4}2\bar{2})_{\mathrm{Al}}$

In Figure 8 (a) the trace directions are indicated with stippled arrows and possible facet planes with solid arrows for the side edges named A-D for dispersoid 3. The resulting indices are summarised in Table 7. The same procedure as described for dispersoid 1 was used to find the directions of possible facet planes and trace directions for dispersoid 3.

Because of too large uncertainties in the side edge directions due to the rounded and irregular shape of dispersoid 4, possible facet normals and trace directions were not determined for dispersoid 4. The irregularities were introduced during the reconstruction and image processing.

From the above results, it can be seen that the methodology proposed in this work is suitable for studies of the habit planes and facets of dispersoids. The methodology are not restricted to only this dispersoid system, but could be applied also to other systems where in depth studies of orientation, morphology and facets are of interest. A practical difficulty when combing the diffraction work and the HAADF STEM tomography is that two different holders had to be applied. As described in Section 2.2 this introduces a rotation of the two systems which have to be accounted for. It is expected that the application of an in plane rotation holder with the possibility for high tilt range will resolve the problem, and such holders are commercially available.

4. Conclusion

The combined study of HAADF STEM tomography and diffraction of α-Al(Fe,Mn)Si dispersoids has lead to a method for coupling the 3D morphology and OR between α-Al(Fe,Mn)Si dispersoids and the aluminum matrix they are embedded in. After low temperature homogenistation of 450 °C for 24 hours a plate shaped morphology was dominating for the dispersoids, and was found for all the dispersoids studied.

Most dispersoids were found to follow the OR $\langle 1\bar{1}1\rangle_\alpha // \langle 1\bar{1}1\rangle_{\mathrm{Al}}$, $\{5\bar{2}\bar{7}\}_\alpha // \{011\}_{\mathrm{Al}}$. Habit planes $(\bar{1}11)_{\mathrm{Al}} // (2\bar{5}0)_\alpha$ were found for one dispersoid following this commonly observed orientation. A dispersoid not following the commonly observed orientation relationship had habit planes found to be $(40\bar{2})_{\mathrm{Al}} // (13\bar{2})_\alpha$, with a zone axis $[010]_{\mathrm{Al}} // [425]_\alpha$. The study also provided information about trace directions and possible facet normals for the side edges of the dispersoids.

Acknowledgement

The KMB project MoReAl financed by The Research Council of Norway, and the industrially partners Hydro and Sapa Technology is acknowledged for the support of this work.

References

[1] Y. Li and L. Arnberg, Acta Mat. 51 (2003), pp. 3415 – 3428.
[2] Y. Li and L. Arnberg, Light Met. (2003), pp. 991 – 997.
[3] P.C.M. de Haan, J. van Rijkom, and J.A.H. Söntgerath, Mat. Sci. Forum 217-222 (1996), pp. 765 – 770.
[4] G. Hausch, P. Furrer, and H. Warlimont, Z. Metall. 69 (1978), pp. 174 – 180.
[5] H. Watanabe, K. Ohori, and Y. Takeuchi, Aluminium 60 (1984), pp. e310 – e313.
[6] M. Cooper and K. Robinson, Acta Cryst. 20 (1966), pp. 614 – 617.
[7] M. Cooper, Acta Cryst. 23 (1967), pp. 1106 – 1107.
[8] P. Donnadieu, G. Lapasset, and T.H. Sanders, Phil. Mag. Lett. 70 (1994), pp. 319 – 26.
[9] V. Elser and C.L. Henley, Phys. Rev. Lett. 55 (1985), pp. 2883 – 2886.
[10] G. Guyot and M. Audier, Phil. Mag. A 52 (1985), pp. L15 – L19.
[11] V. Hansen, B. Anderson, J.E. Tibbals, and J. Gjønnes, Metall. Mat. Trans. B 26B (1995), pp. 839 – 849.

[12] V. Hansen and J. Gjønnes, Phil. Mag. A 73 (1996), pp. 1147 – 1158.
[13] V. Hansen, J. Gjønnes, and B. Andersson, J. of Mat. Sci. Lett. 8 (1989), pp. 823 – 826.
[14] D.C. Koskenmaki, H.S. Chen, and K. Rao, Phys. Rev. B 33 (1986), pp. 5328 – 5336.
[15] J. Pannetier, J. Dubois, C. Janot, and A. Bilde, Phil. Mag. B 55 (1987), pp. 435 – 457.
[16] E. Stern and Y. Ma, Phil. Mag. Lett. 56 (1987), pp. 103 – 108.
[17] W. Hutchinson, A. Oscarsson, and Å. Karlsson, Mat. Sci. Tech. 5 (1989), pp. 1118 – 1127.
[18] E. Nes, Acta Metal. 24 (1976), pp. 391 – 398.
[19] F. Humphreys, Acta Metal. 25 (1977), pp. 1323 – 1344.
[20] J.P. Suni, R.D. Doherty, P.A. Hollinshead, T.N. Rouns, and R.T. Shuey, Aluminum Alloys 2 (1998), pp. 1203 – 1208.
[21] Y.J. Li, A.M.F. Muggerud, A. Olsen, and T. Furu, Acta Mat. 60 (2012), pp. 1004 – 1014.
[22] A.M.F. Muggerud, E. Mørtsell, Y. Li, and R. Holmestad, Mat. Sci. Eng. A 567 (2013), pp. 21 – 28.
[23] P. Furrer and G. Hausch, Mat. Sci. (1979), pp. 155 – 162.
[24] P. Midgley and M. Weyland, Ultramicroscopy 96 (2003), pp. 413 – 431.
[25] D. Williams and C.B. Carter, *Transmission Electron Microscopy*, Springer Science, New York, 2009.
[26] M. Weyland, P.A. Midgley, and J.M. Thomas, J. Phys. Chem. B 105 (2001), pp. 7882 – 7886.
[27] P.R. Buseck, R.E. Dunin-Borkowski, B. Devouard, R.B. Frankel, M. R.McCartney, P.A. Midgley, M. Pósfai, and M. Weyland, Proc. Nat. Aca. Sci. USA 98 (2001), pp. 13490 – 13495.
[28] K. Kaneko, K. Inoke, K. Sato, K. Kitawaki, H. Higashida, I. Arslan, and P. Midgley, Ultramicro. 108 (2008), pp. 210 – 220.
[29] K. Kaneko, K. Sato, Z. Horita, and K. Inoke, Mat. Sci. Forum (2007), pp. 2009 – 2012.
[30] Z. Feng, Y. Yang, B. Huang, X. Luo, M. Li, Y. Chen, M. Han, M. Fu, and J. Ru, Phil. Mag. 93 (2013), pp. 1843 – 1858.
[31] K. Sato, H. Matsumoto, K. Kodaira, T.J. Konno, and A. Chiba, J. Alloys Comp. 506 (2010), pp. 607 – 614.
[32] M. Abramoff, P. Magelhaes, and S. Ram, Biophot. Intern.l 11 (2004), pp. 36 – 42.
[33] C. Messaoudii, T. Boudier, C.O. Sorzano, and S. Marco, BMC Bioinformatics. 288 (2007).
[34] C.O. Sorzano, C. Messaoudi, M. Eibauer, J.R. Bilbao-Castro, R. Hegerl, S. Nickell, S. Marco, and J.M. Carazo, BMC Bioinformatics. 124 (2009).